

E-ISSN 2980-3012

# Physics and Astronomy Reports

VOLUME 1 • NUMBER 1 • JUNE 2023



İSTANBUL  
UNIVERSITY  
PRESS

**OWNER**

Prof. Dr. Tansel AK

Istanbul University, Faculty of Science, Istanbul, Turkiye

**RESPONSIBLE MANAGER**

Prof. Dr. Elif AKALIN

Istanbul University, Faculty of Science,  
Department of Physics, Istanbul, Turkiye

**CORRESPONDENCE ADDRESS**

Istanbul University Faculty of Science  
PK 34134 Vezneciler, Fatih, Istanbul, Turkiye

Phone : +90 (212) 455 57 00

Fax : +90 (212) 512 21 40

E-mail: [par@istanbul.edu.tr](mailto:par@istanbul.edu.tr)

<https://iupress.istanbul.edu.tr/en/journal/par/home>

<https://dergipark.org.tr/en/pub/par>

**PUBLISHER**

Istanbul University Press

Istanbul University Central Campus,  
34452 Beyazit, Fatih, Istanbul, Turkiye

Phone: +90 (212) 440 00 00

---

Authors bear responsibility for the content of their published articles.

The publication language of the journal is English.

This is a scholarly, international, peer-reviewed and open-access journal published biannually in June and December.

---

**Publication Type:** Periodical

---



## EDITORIAL MANAGEMENT BOARD

---

### EDITOR-IN-CHIEF

**Prof. Dr. Elif AKALIN** – Istanbul University, Faculty of Science, Department of Physics, Istanbul, Türkiye – [eakalin@istanbul.edu.tr](mailto:eakalin@istanbul.edu.tr)

### CO-EDITOR

**Prof. Dr. Selçuk BİLİR** – Istanbul University, Faculty of Science, Department of Astronomy and Space Sciences, Istanbul, Türkiye – [sbilir@istanbul.edu.tr](mailto:sbilir@istanbul.edu.tr)

### STATISTICS EDITOR

**Dr. Hikmet ÇAKMAK** – Istanbul University, Faculty of Science, Department of Astronomy and Space Sciences, Istanbul, Türkiye – [hcakmak@istanbul.edu.tr](mailto:hcakmak@istanbul.edu.tr)

### PUBLICITY MANAGER

**Assit. Prof. Dr. Talar YONTAN** – Istanbul University, Faculty of Science, Department of Astronomy and Space Sciences, Istanbul, Türkiye – [talar.yontan@istanbul.edu.tr](mailto:talar.yontan@istanbul.edu.tr)

### EDITORIAL ASSISTANT

**Assit. Prof. Dr. Özgecan ÖNAL TAŞ** – Istanbul University, Faculty of Science, Department of Astronomy and Space Sciences, Istanbul, Türkiye – [ozgecan.onal@istanbul.edu.tr](mailto:ozgecan.onal@istanbul.edu.tr)

### LANGUAGE EDITORS

**Rachel Elana KRISS** – Istanbul University, Istanbul, Türkiye – [rachel.kriss@istanbul.edu.tr](mailto:rachel.kriss@istanbul.edu.tr)

**Elizabeth Mary EARL** – Istanbul University, Istanbul, Türkiye – [elizabeth.earl@istanbul.edu.tr](mailto:elizabeth.earl@istanbul.edu.tr)

## EDITORIAL BOARD

---

**Volkan BAKIŞ** – Akdeniz University, Antalya, Türkiye – [volkanbakis@akdeniz.edu.tr](mailto:volkanbakis@akdeniz.edu.tr)

**Timothy BANKS** – Harper College, Chicago, United-States – [tim.banks@nielsen.com](mailto:tim.banks@nielsen.com)

**Gönül BAŞAR** – Istanbul University, Istanbul, Türkiye – [gbasar@istanbul.edu.tr](mailto:gbasar@istanbul.edu.tr)

**Helene CARRERE** – University of Toulouse, Toulouse, France – [carrere@insa-toulouse.fr](mailto:carrere@insa-toulouse.fr)

**Ömür ÇAKIRLI** – Ege University, Izmir, Türkiye – [omur.cakirli@ege.edu.tr](mailto:omur.cakirli@ege.edu.tr)

**Uğur ÇEVİK** – Karadeniz Teknik University, Trabzon, Türkiye – [ugurc@ktu.edu.tr](mailto:ugurc@ktu.edu.tr)

**Ahmet DERVİŞOĞLU** – Ataturk University, Erzurum, Türkiye – [ahmet.dervisoglu@atauni.edu.tr](mailto:ahmet.dervisoglu@atauni.edu.tr)

**Goran DJORDJEVIC** – University of Nis, Nis, Serbia – [gorandj@junis.ni.ac.rs](mailto:gorandj@junis.ni.ac.rs)

**Yavuz EKŞİ** – Istanbul University, Istanbul, Türkiye – [eksi@itu.edu.tr](mailto:eksi@itu.edu.tr)

**Ayşe EROL** – Akdeniz University, Antalya, Türkiye – [ayseerol@istanbul.edu.tr](mailto:ayseerol@istanbul.edu.tr)

**Muhsin HARAKEH** – University of Groningen, Groningen, Netherlands – [m.n.harakeh@rug.nl](mailto:m.n.harakeh@rug.nl)

**Mohamed HENINI** – University of Nottingham, Nottingham, United-Kingdom – [Mohamed.Henini@nottingham.ac.uk](mailto:Mohamed.Henini@nottingham.ac.uk)

**Ümit KAVAK** – NASA Ames Research Center, Moffett-Field, United-States – [ukavak@sofia.usra.edu](mailto:ukavak@sofia.usra.edu)

**Mükremin KILIÇ** – University of Oklahoma, Oklahoma, United-States – [kilic@ou.edu](mailto:kilic@ou.edu)

**Sophie KRÖGER** – Hochschule für Technik und Wirtschaft Berlin, Berlin, Germany – [sophie.kroeger@hte-berlin.de](mailto:sophie.kroeger@hte-berlin.de)

**Yeşim ÖKTEM** – Istanbul University, Istanbul, Türkiye – [yesim.oktem@istanbul.edu.tr](mailto:yesim.oktem@istanbul.edu.tr)

**Faruk SOYDUGAN** – Canakkale Onsekiz Mart University, Canakkale, Türkiye – [fsoydugan@comu.edu.tr](mailto:fsoydugan@comu.edu.tr)

**Horst STOECKER** – Goethe University, Frankfurt, Germany – [stoecker@fias.uni-frankfurt.de](mailto:stoecker@fias.uni-frankfurt.de)

**Timur ŞAHİN** – Akdeniz University, Antalya, Türkiye – [timursahin@akdeniz.edu.tr](mailto:timursahin@akdeniz.edu.tr)

**Hakan Volkan ŞENAVCI** – Ankara University, Ankara, Türkiye – [hvsenavci@ankara.edu.tr](mailto:hvsenavci@ankara.edu.tr)

**Kadri YAKUT** – Ege University, Izmir, Türkiye – [kadri.yakut@ege.edu.tr](mailto:kadri.yakut@ege.edu.tr)

**Özgür YAVUZÇETİN** – University of Wisconsin-Whitewater, Whitewater, United-States – [yavuzce@uww.edu](mailto:yavuzce@uww.edu)

## CONTENTS

---

### *RESEARCH ARTICLES*

- 1** Analysis of the Young Open Cluster Trumpler 2 Using Gaia DR3 Data  
**Seval TAŞDEMİR, Talar YONTAN**
- 11** The Age-Metallicity Relation in the Solar Neighbourhood  
**Sibel DÖNER, Serap AK, Özgecan ÖNAL TAŞ, Olcay PLEVNE**
- 27** Band Profile and Surface Acoustic Wave Attenuation Analysis of Polygonal Cavity-type Piezoelectric Phononic Crystals  
**Furkan KURUOĞLU, Nurseli Seda GENÇ, Ayşe EROL, Ahmet ÇİÇEK**
- 32** Laser Spectroscopic Investigation of the Hyperfine Structure of Atomic Manganese in the Mid-infrared Wavelength Range  
**Sophie KRÖGER, L. WINDHOLZ, Gönül BAŞAR**
- 38** Selective Antimicrobial Properties of W-Ge Nanocomposite Thin Films  
**Selçuk ATASOY, Yasin KURUL, Sıtkı AKTAŞ, Fahrettin SARCAN, Mustafa Şükrü KURT, Adnan AYNA, Ekrem DARENDELİOĞLU, Ayşe EROL**

# Analysis of the Young Open Cluster Trumpler 2 Using Gaia DR3 Data

S. Taşdemir<sup>1\*</sup> , and T. Yontan<sup>2</sup> 

<sup>1</sup>Istanbul University, Institute of Graduate Studies in Science, Programme of Astronomy and Space Sciences, 34116, Beyazit, Istanbul, Türkiye

<sup>2</sup>Istanbul University, Faculty of Science, Department of Astronomy and Space Sciences, 34119, Beyazit, Istanbul, Türkiye

## ABSTRACT

We present an investigation of the open cluster Trumpler 2 using *Gaia* DR3 photometric, astrometric and spectroscopic data. 92 stars were identified as likely members of the cluster, with membership probabilities greater than 0.5. The mean proper-motion components of the cluster are derived as  $(\mu_\alpha \cos \delta, \mu_\delta) = (1.494 \pm 0.004, -5.386 \pm 0.005)$  mas yr<sup>-1</sup>. By comparing the *Gaia* based colour-magnitude diagram with the PARSEC isochrones scaled to  $z = 0.0088$ , age, distance modulus and reddening are simultaneously estimated as  $t = 110 \pm 10$  Myr,  $\mu = 10.027 \pm 0.149$  mag and  $E(G_{BP} - G_{RP}) = 0.452 \pm 0.019$  mag, respectively. The total mass of the cluster is estimated as  $162 M/M_\odot$  based on the stars with membership probabilities  $P > 0$ . The mass function slope is derived to be  $\Gamma = 1.33 \pm 0.13$  for Trumpler 2. This value is in a good agreement with that of Salpeter. Galactic orbit analyses show that the Trumpler 2 orbits in a boxy pattern outside the solar circle and belongs to the young thin-disc component of the Galaxy.

**Keywords:** Galaxy: open clusters and associations; individual: Trumpler 2, Galaxy: Stellar kinematics, stars: Hertzsprung Russell (HR) diagram

## 1. INTRODUCTION

Open Clusters (OCs) are celestial objects consisting of stars bound to each other via mutual gravitational attraction. OCs are formed when a molecular cloud collapses. This means that the member stars of an OC formed under similar physical conditions and at a similar time. Hence, the stars that belong to the OCs have similar properties such as distance to Sun, metallicity and age. However stellar masses vary, leading to a range of stellar luminosities being observed in such clusters. These features make OCs valuable and interesting laboratories for understanding the formation and evolution of our Galaxy (Lada & Lada 2003).

The available information in the literature for the Trumpler 2 is as follows: Trumpler 2 ( $\alpha = 02^{\text{h}}36^{\text{m}}55^{\text{s}}.7, \delta = +55^\circ 54' 18''; l = 137^\circ.3863, b = -03^\circ.9778, J2000$ ) is located at the Perseus Constellation. Since the cluster has low central concentration, it is classified in the Trumpler catalogue as II 2p (Trumpler 1930). Frolov et al. (2006) determined proper motion components of Trumpler 2 on 6 plates with a maximal epoch difference of 63 years by considering the positions of about 3,000 stars within the  $B \sim < 16.25$  magnitude. By taking into account 148 stars assessed as the most probable cluster members, based on astrometric and photometric criteria, Frolov et al. (2006) obtained the colour-excess, distance modulus, distance and age

as  $0.40 \pm 0.06$  mag,  $10.50 \pm 0.35$  mag, 725 pc and 89 Myr, respectively. Zejda et al. (2012) determined the mean proper-motion components of 879 open clusters including Trumpler 2, based on 4 member stars in that cluster, as  $(\mu_\alpha \cos \delta, \mu_\delta) = (1.0 \pm 0.3, -4.6 \pm 0.3)$  mas yr<sup>-1</sup>. Dias et al. (2014) obtained the mean proper-motion components by using the U.S. Naval Observatory CCD Astrograph Catalogue (UCAC4; Zacharias et al. 2013) as  $(\mu_\alpha \cos \delta, \mu_\delta) = (0.11 \pm 1.48, -3.49 \pm 2.23)$  mas yr<sup>-1</sup>. They also identified 346 stars as members of Trumpler 2. Paunzen et al. (2014) studied chemically peculiar stars inside 10 open clusters including Trumpler 2. Moreover, it is confirmed that HD 16080 and BD+55 664 are members of Trumpler 2. As part of a survey of 1241 OCs, Joshi et al. (2016) derived the colour-excess, distance, age and total mass of Trumpler 2 as  $E(B - V) = 0.321$  mag,  $d = 670$  pc,  $\log t = 7.925$  yr, and  $M/M_\odot = 72.63 \pm 0.19$ , respectively.

With the beginning of the *Gaia* era (Gaia Collaboration et al. 2016), the quality and accuracy of photometric, astrometric, and spectroscopic data have considerably taken a turn for the better. Cantat-Gaudin et al. (2018) investigated 1229 open clusters using the second data release of *Gaia* (*Gaia* DR2; Gaia Collaboration et al. 2018) and listed the mean astrometric parameters and membership probabilities of open clusters to characterize them. Cantat-Gaudin et al. (2018) identified 179 likely member stars ( $P \geq 0.5$ ) in the direction of Trumpler 2, resulting

Corresponding Author: S. Taşdemir E-mail: tasdemir.seval@ogr.iu.edu.tr

Submitted: 03.03.2023 • Revision Requested: 27.03.2023 • Last Revision Received: 19.04.2023 • Accepted: 26.04.2023 • Published Online: 10.05.2023



This article is licensed under a Creative Commons Attribution-NonCommercial 4.0 International License (CC BY-NC 4.0)

**Table 1.** Astrophysical parameters for Trumpler 2 compiled from the literature: Colour excesses ( $E(B - V)$ ), distance moduli ( $\mu_V$ ), distances ( $d$ ), iron abundances ([Fe/H]), age ( $t$ ), proper-motion components ( $\langle \mu_\alpha \cos \delta \rangle$ ,  $\langle \mu_\delta \rangle$ ), radial velocities ( $V_\gamma$ ) and references (Ref).

$E(B - V)$ (mag)	$\mu_V$ (mag)	$d$ (pc)	[Fe/H] (dex)	$t$ (Myr)	$\langle \mu_\alpha \cos \delta \rangle$ (mas yr <sup>-1</sup> )	$\langle \mu_\delta \rangle$ (mas yr <sup>-1</sup> )	$V_\gamma$ (km s <sup>-1</sup> )	Ref
0.40±0.06	10.50±0.35	725	0.00	89	–	–	–	(01)
–	–	–	–	–	1.0±0.3	-4.6±0.3	–	(02)
–	–	–	–	–	0.11±1.48	-3.49±2.23	–	(03)
0.321	–	670	–	84	–	–	–	(04)
–	–	685 <sup>+50</sup> <sub>-44</sub>	–	–	1.583±0.018	-5.352 ±0.015	–	(05)
–	–	685 <sup>+50</sup> <sub>-44</sub>	–	–	1.583±0.018	-5.352 ±0.015	-4.12±0.09	(06)
0.308 <sup>+0.007</sup> <sub>-0.006</sub>	10.289±0.021	736±7	0.00	91 <sup>+14</sup> <sub>-7</sub>	–	–	–	(07)
–	–	694±23	–	81±5	1.574±0.273	-5.323±0.242	–	(08)
0.277	10.12	710	–	112	1.583±0.192	-5.352 ±0.167	–	(09)
0.307	–	685	-0.088±0.07	92	1.583±0.192	-5.352±0.167	-6.045±12.32	(10)
0.355±0.041	10.25±0.029	677±9	0.140±0.149	238±132	1.581±0.236	-5.343±0.193	-3.990±0.746	(11)
0.316	–	710	-0.262±0.106	110	1.58±0.19	-5.35±0.17	-4.16±0.02	(12)

(01) Frolov et al. (2006), (02) Zejda et al. (2012), (03) Dias et al. (2014), (04) Joshi et al. (2016), (05) Cantat-Gaudin et al. (2018), (06) Soubiran et al. (2018), (07) Bossini et al. (2019), (08) Liu & Pang (2019), (9) Cantat-Gaudin et al. (2020), (10) Zhong et al. (2020), (11) Dias et al. (2021), (12) Carrera et al. (2022)

is the proper-motion components being estimated as  $(\mu_\alpha \cos \delta, \mu_\delta) = (1.583 \pm 0.018, -5.352 \pm 0.015)$  mas yr<sup>-1</sup> and distance  $d = 685^{+50}_{-14}$  pc. Soubiran et al. (2018) performed kinematic analyses for 861 open clusters using *Gaia* DR2 data, estimating the radial velocity  $V_\gamma = -4.12 \pm 0.09$  km s<sup>-1</sup>, and space velocity components  $(U, V, W) = (-4.12 \pm 0.08, -11.98 \pm 0.08, -13.60 \pm 0.06)$  km s<sup>-1</sup> for Trumpler 2. Calculating the age, distance, distance modulus, and extinction values of 269 open clusters with the data obtained from the *Gaia* DR2 catalogue using the Bayesian statistical method, Bossini et al. (2019) determined the age of Trumpler 2 cluster as  $91^{+14}_{-7}$  Myr. Liu & Pang (2019) used 86 member stars to calculate the mean proper-motion components, trigonometric parallaxes, and age. Accordingly, the values of the parameters as given as  $(\langle \mu_\alpha \cos \delta \rangle, \langle \mu_\delta \rangle) = (1.574 \pm 0.273, -5.323 \pm 0.242)$  mas yr<sup>-1</sup>,  $\langle \varpi \rangle = 1.441 \pm 0.048$  mas, and  $t = 81 \pm 5$  Myr. Cantat-Gaudin et al. (2020) obtained the astrometric and astrophysical parameters belonging to 2017 open clusters based on *Gaia* DR2 data. According to this study, the mean proper-motion components and parallaxes are calculated from 154 member stars as  $(\langle \mu_\alpha \cos \delta \rangle, \langle \mu_\delta \rangle) = (1.583 \pm 0.192, -5.352 \pm 0.167)$  mas yr<sup>-1</sup> and  $\langle \varpi \rangle = 1.431 \pm 0.058$  mas, respectively. The recent study on the Trumpler 2 was carried out by Carrera et al. (2022). They performed high-resolution spectroscopic analyses and obtained metallicities for 41 stars with high membership probabilities in 20 open clusters including Trumpler 2. They determined metallicity value of Trumpler 2 as  $-0.262 \pm 0.106$  dex. Furthermore, analysing *Gaia* EDR3 astrometric data, Carrera et al. (2022) obtained the birth radius as  $8.08 \pm 0.05$  kpc as well as the kinematic and dynamic orbital parameters of the cluster. The literature results are listed in Table 1 for ease of comparison.

## 2. DATA

### 2.1. Astrometric and Photometric Data

By using the high-quality data of the third data release of *Gaia* (*Gaia* DR3, Gaia Collaboration et al. 2022), we constructed the astrometric and photometric catalogue of the cluster. For this, we used the equatorial coordinates calculated by Cantat-Gaudin & Anders (2020)  $(\langle \alpha, \delta \rangle) = (02^h 36^m 55^s .7, \delta = +55^\circ 54' 18'')$  and take into account all stars located throughout the field of Trumpler 2 within the 50 arcmin region around the centre. Therefore it has been found that there are 121,569 stars with the stellar magnitudes between  $7 < G \leq 23$  mag. The identification chart of stars ( $50' \times 50'$ ) located in regions of Trumpler 2 is shown in Figure 1.

### 2.2. Photometric Completeness Limit and Photometric Errors

To calculate reliable structural and astrophysical parameters of open clusters, it is important to obtain the photometric completeness limit of the data. To determine the accurate parameter estimates for Trumpler 2, the photometric completeness limit of the stars is established by counting the stars corresponding to the  $G$  magnitudes. In Figure 2, the histogram shows the completeness limit as  $G = 20.50$  mag which is indicative of an increase in the star count relative to the magnitude until this value and then decreases after it. In the following analyses, stars fainter than this value were excluded statistically and were not taken into account. The uncertainties in the *Gaia* DR3 data were accepted as interval errors and calculated mean  $G$  magnitudes with  $G_{BP} - G_{RP}$  colour indices of stars in the cluster region as a function of  $G$  magnitude intervals. Considering  $G = 20.50$

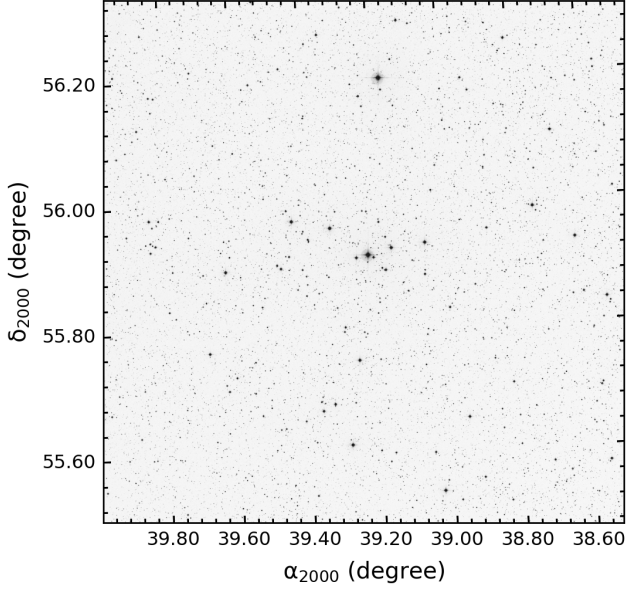


**Figure 1.** Identification chart of Trumpler 2. The field of view of the chart is  $50' \times 50'$ . North and East correspond with the up and left directions, respectively.

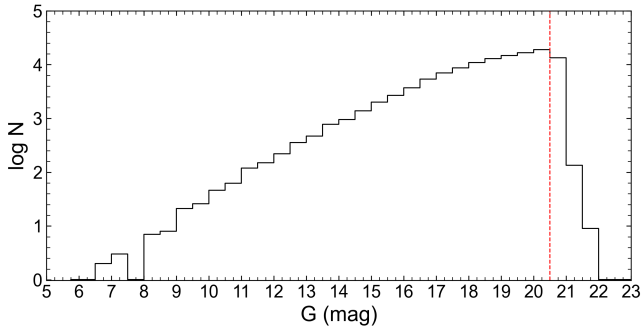


**Figure 2.** Histogram of number of stars with respect to  $G$  magnitude intervals for Trumpler 2. The red dashed-line indicates the faint limit magnitude of the cluster.

mag, the mean internal  $G$  magnitude and  $G_{BP} - G_{RP}$  colour index were calculated as 0.007 and 0.142 mag at this limit, respectively. Mean errors of photometric data are listed in Table 2 as a function of  $G$  apparent magnitude. Also, Figure 3 presents the mean internal errors of  $G$  magnitudes and  $G_{BP} - G_{RP}$  colour indices.

### 3. RESULTS

#### 3.1. Structural Parameters of Trumpler 2

In order to investigate the extent of Trumpler 2 and determine its structural parameters, we performed Radial Density Profile (RDP) analysis. By using *Gaia* DR3 data within 50 arcmin, we divided the cluster area into many concentric rings from the central coordinates given by Cantat-Gaudin et al. (2020). For the calculation of the stellar density ( $\rho(r)$ ), we used the stars within the  $G \leq 20.5$  mag completeness limit and utilized the

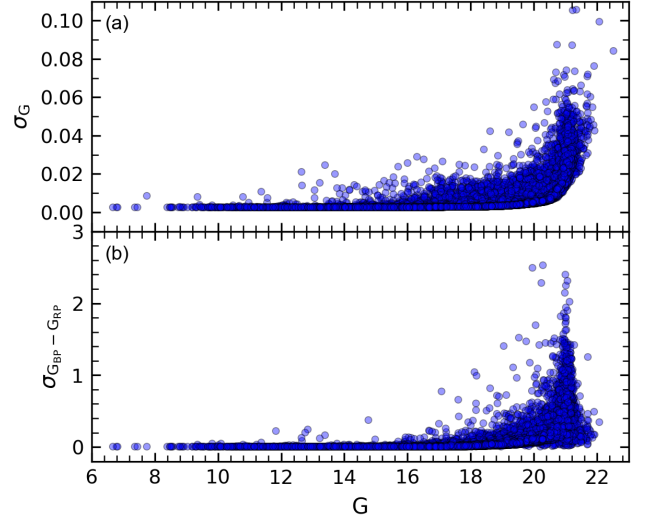


**Figure 3.** Mean photometric errors calculated for  $G$  apparent magnitude (a) and  $G_{BP} - G_{RP}$  colour index for Trumpler 2.

**Table 2.** Mean internal photometric errors per magnitude bin in  $G$  apparent magnitude and  $G_{BP} - G_{RP}$  colour index for Trumpler 2.

$G$ (mag)	$N$	$\sigma_G$ (mag)	$\sigma_{G_{BP}-G_{RP}}$ (mag)
(06, 14]	1839	0.003	0.006
(14, 15]	2056	0.003	0.006
(15, 16]	3930	0.003	0.006
(16, 17]	7566	0.003	0.009
(17, 18]	14083	0.003	0.017
(18, 19]	21699	0.003	0.038
(19, 20]	29495	0.005	0.081
(20, 21]	37454	0.010	0.208
(21, 23]	3447	0.027	0.430

equation of  $R_i = N_i/A_i$  for each  $i^{\text{th}}$  ring, where  $N_i$  and  $A_i$  are the number of stars falling into a given ring and the area of that ring, respectively. Uncertainties in the stellar density were calculated using the Poisson statistical measure  $1/\sqrt{N}$ , where  $N$  is the number of stars. Then, to plot the radial density profile we used the stellar density and fitted the RDP with the empirical King (1962) model defined by the following formula:

$$\rho(r) = f_{\text{bg}} + \frac{f_0}{1 + (r/r_c)^2} \quad (1)$$

In the equation,  $r$  denotes the radius of the cluster. The terms  $f_{\text{bg}}$ ,  $f_0$ ,  $r_c$  represent the background stellar density, the central stellar density and the core radius of Trumpler 2, respectively. Minimum  $\chi^2$  estimation was used in the RDP fitting process to estimate the  $f_{\text{bg}}$ ,  $f_0$  and  $r_c$  parameters which are listed in Table 3. The best-fit solution to the radial density profile is illustrated with a solid black line in Figure 4. The correlation coefficient of the King model (King 1962) with the best-fit model parameters to the data is  $R^2 = 0.971$ , which implies that the estimated structural parameters are well estimated.

**Table 3.** The structural parameters of the Trumpler 2 according to the King (1962) model analyses:  $(\alpha, \delta)$ ,  $f_0$ ,  $f_{bg}$ ,  $r_c$ ,  $r_{lim}^{obs}$ ,  $r_{lim}^{cal}$  and  $R^2$  are equatorial coordinates, central stellar density, the background stellar density, the core radius, observational limiting radius, calculated limiting radius and correlation coefficient, respectively.

Cluster	$\alpha_{J2000}$ (hh:mm:ss.s)	$\delta_{J2000}$ (dd:mm:ss)	$f_0$ (stars arcmin $^{-2}$ )	$f_{bg}$ (stars arcmin $^{-2}$ )	$r_c$ (arcmin)	$r_{lim}^{obs}$ (arcmin)	$r_{lim}^{cal}$ (arcmin)	$R^2$
Trumpler 2	02:36:55.7	+55:54:18	$1.55 \pm 0.33$	$12.59 \pm 0.02$	$2.48 \pm 1.09$	12	11.7	0.971

Taking into account the visualisation of RDP, we determine the limiting radii ( $r_{lim}^{obs}$ ) of cluster as 12. The structural parameters were derived as  $f_{bg} = 12.59 \pm 0.02$ ,  $f_0 = 1.55 \pm 0.33$  stars arcmin $^{-2}$  and  $r_c = 2.48 \pm 1.09$  arcmin (see also Table 3). To validate the precision of the observed limiting radii ( $r_{lim}^{obs}$ ), equation given by Bukowiecki et al. (2011) is used as follow:

$$r_{lim} = r_c \sqrt{\frac{f_0}{3\sigma_{bg}} - 1}. \quad (2)$$

From the equation, we calculated the theoretical limiting radius as 11.7 arcmin. It is obvious that theoretical and observed limiting radii values are in good agreement with each other.

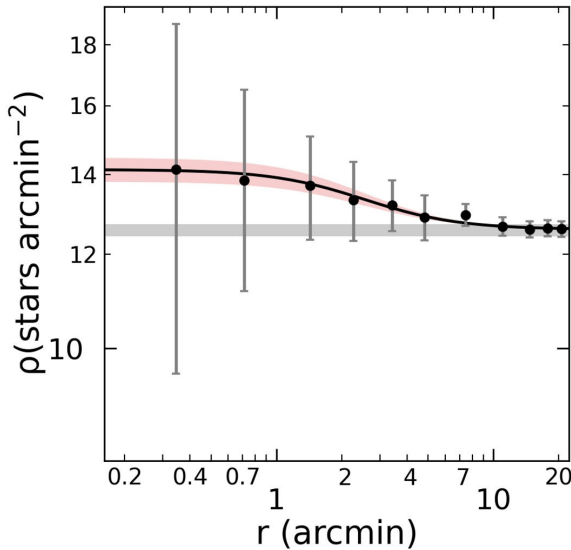


**Figure 4.** The stellar density distribution of Trumpler 2. The fitted black curve shows the RDP profile of King (1962), whereas the horizontal grey band represents the background stellar density. The  $1\sigma$  King fit uncertainty is pictured by the red-shaded area.

### 3.2. Membership Probabilities of Stars

As open clusters are located within the Galactic plane, they are highly contaminated by foreground and background stars. This situation makes it necessary to separate cluster members from field stars for determining reliable astrophysical parameters of the studied cluster. As the member stars of an OC form under similar physical conditions, they have similar vectorial movements in space. These properties make proper-motion components functional information to distinguish cluster members

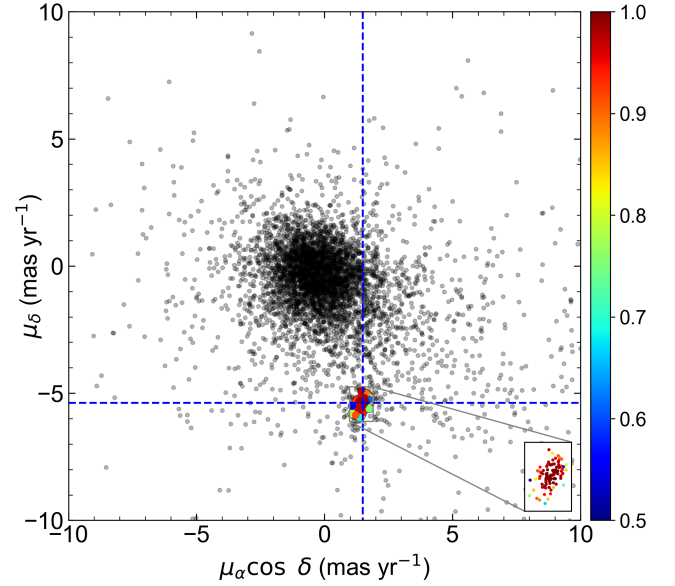


**Figure 5.** VPD of Trumpler 2 based on *Gaia* DR3 astrometry. The membership probabilities of the stars are identified with the colour scale shown on the right for the cluster. The zoomed-in panel inset represents the region of condensation for the cluster in the VPD. The mean proper-motion value of Trumpler 2 is shown by the intersection of the dashed blue lines.

from the field stars (Bisht et al. 2020). The high accuracy of *Gaia* DR3 data (Gaia Collaboration et al. 2022) leads to reliable results for membership analyses. To determine the membership probabilities ( $P$ ) of stars in the direction of Trumpler 2, we used the membership determination method known as Photometric Membership Assignment in Stellar Clusters (UPMASK, Krone-Martins & Moitinho 2014) on the *Gaia* DR3 astrometric data. Many researchers have previously utilized this method (Cantat-Gaudin et al. 2018, 2020; Castro-Ginard et al. 2018, 2019, 2020; Banks et al. 2020; Akbulut et al. 2021; Wang et al. 2022; Yontan 2023). UPMASK is a clustering method which is defined as  $k$ -means. The method allows the detection of similar groups of stars according to their proper-motion components and trigonometric parallax, providing statistical probability values for membership of these groups. We used each detected stars' astrometric measurements ( $\alpha, \delta, \mu_\alpha \cos \delta, \mu_\delta, \varpi$ ) as well as their uncertainties by running 100 iterations of UPMASK to set their membership probability values. Hence, we identified 92 stars for Trumpler 2 as the most probable member stars with membership probabilities  $P \geq 0.5$ , brighter than the photometric completeness limits and located within the limited radius ( $r_{lim}^{obs}$ ) described above.



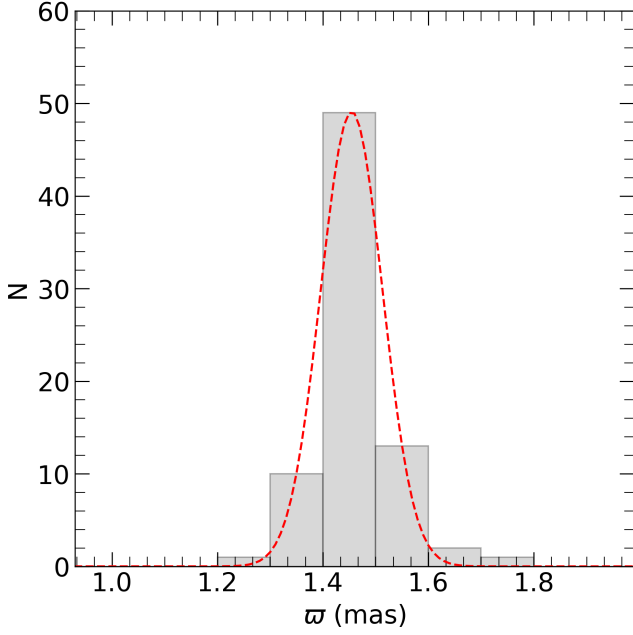


**Figure 6.** Histogram of mean trigonometric parallax estimation of Trumpler 2 from the most probable members ( $P \geq 0.50$ ). Red dashed line shows the fitted Gaussian function.

We constructed the Vector-Point Diagram (VPD), which consists of proper-motion components of the stars, to investigate the most probable cluster member stars, as shown in Figure 5. It can be seen from the figure that Trumpler 2 is clearly distinguished from the foreground and background stars. In Figure 5, the intersection of the blue dashed lines represents the mean proper-motion values obtained from the most probable member stars ( $P \geq 0.5$ ). The mean proper-motion components of Trumpler 2 are found as  $(\mu_\alpha \cos \delta, \mu_\delta) = (1.494 \pm 0.004, -5.386 \pm 0.005)$  mas yr<sup>-1</sup>. Also, using these member stars we plotted the trigonometric parallax histogram and calculated the mean value by fitting the Gaussian functions to the distributions as shown in Figure 6. Thus, we estimated the mean trigonometric parallax value as  $\varpi = 1.455 \pm 0.059$  mas for the cluster. We transformed the mean trigonometric parallax to the trigonometric parallax distance ( $d_\varpi$ ) by using the linear equation of  $d(\text{pc}) = 1000/\varpi$  (mas) and estimated the value as  $d_\varpi = 687 \pm 27$  pc. This result is in a good agreement with the results determined in the *Gaia* era by different researchers (for a detailed comparison see Table 1).

### 3.3. Astrophysical Parameters of Trumpler 2

Colour-magnitude diagrams (CMDs) are essential tools to obtain basic astrophysical parameters such as age, distance modulus, reddening and metallicity of open clusters. These diagrams allow identification of a cluster's main sequence, turn-off point, and giant members as well as the determination of reliable cluster parameters. In the current study, considering the morphology of the most probable ( $P \geq 0.5$ ) cluster members on the *Gaia* based CMD, we estimated age, distance moduli

and reddening simultaneously, whereas the metallicity [Fe/H] was adopted with the value of [Fe/H] =  $-0.262 \pm 0.106$  dex as given by Carrera et al. (2022). To derive the age, distance moduli and reddening of Trumpler 2, we applied PARSEC stellar isochrones (Bressan et al. 2012) to the observed CMD and obtained the best fit. We used the PARSEC<sup>1</sup> isochrones corresponding to *Gaia* Early Data Release 3 (EDR3) photometric passbands (Riello et al. 2021).

We transformed the adopted metallicity [Fe/H] =  $-0.262 \pm 0.106$  dex) to the mass fraction  $z$  for the selection of isochrones as well as for determination of astrophysical parameters. For the transformation, we applied the analytic expressions of Bovy<sup>2</sup> suitable for PARSEC isochrones (Bressan et al. 2012). The expressions are given as follow:

$$z_x = 10^{[\text{Fe}/\text{H}] + \log\left(\frac{z_\odot}{1 - 0.248 - 2.78 \times z_\odot}\right)}, \quad (3)$$

and

$$z = \frac{(z_x - 0.2485 \times z_x)}{(2.78 \times z_x + 1)}. \quad (4)$$

where  $z_x$  and  $z_\odot$  indicate intermediate values where solar metallicity  $z_\odot$  was accepted as 0.0152 (Bressan et al. 2012). We derived  $z = 0.0088$  for Trumpler 2.

To determine the age, distance moduli and reddening of the cluster, we constructed a  $G \times (G_{\text{BP}} - G_{\text{RP}})$  CMD and fitted selected isochrones by visual inspection, according to the most probable ( $P \geq 0.5$ ) main sequence, turn-off, and giant member stars. Before the selection of isochrones, we scaled them to the mass fraction  $z$ , as determined above. This procedure indicated that the *Gaia*-based colour excess for Trumpler 2 is  $E(G_{\text{BP}} - G_{\text{RP}}) = 0.452 \pm 0.019$  mag. To compare with literature studies more accurately, we transformed this value to the *UBV*-based colour excess  $E(B - V)$  by employing the equation  $E(G_{\text{BP}} - G_{\text{RP}}) = 1.41 \times E(B - V)$  as given by Sun et al. (2021). Hence, we find the value as  $E(B - V) = 0.320 \pm 0.013$  mag which is compatible with the results given by Joshi et al. (2016), Bossini et al. (2019), Zhong et al. (2020) and Carrera et al. (2022) within the errors (see Table 1).

The PARSEC isochrones with different ages of  $\log(\text{age}) = 8.00, 8.04$  and  $8.08$  with  $z = 0.0088$  were superimposed to the observed  $G \times (G_{\text{BP}} - G_{\text{RP}})$  CMD as shown in Figure 7. The overall fit is acceptable for  $\log(\text{age}) = 8.04$  to the most probable members ( $P \geq 0.5$ ), corresponding to the age of Trumpler 2 being  $t = 110 \pm 10$  Myr. The derived age value is compatible with the values given by Bossini et al. (2019), Zhong et al. (2020) and Cantat-Gaudin et al. (2020) within the formally stated errors (Table 1). The estimated distance modulus  $\mu = 10.027 \pm 0.149$  mag corresponds to an isochrone distance

<sup>1</sup> <http://stev.oapd.inaf.it/cgi-bin/cmd>

<sup>2</sup> <https://github.com/jobovy/isodist/blob/master/isodist/Isochrone.py>

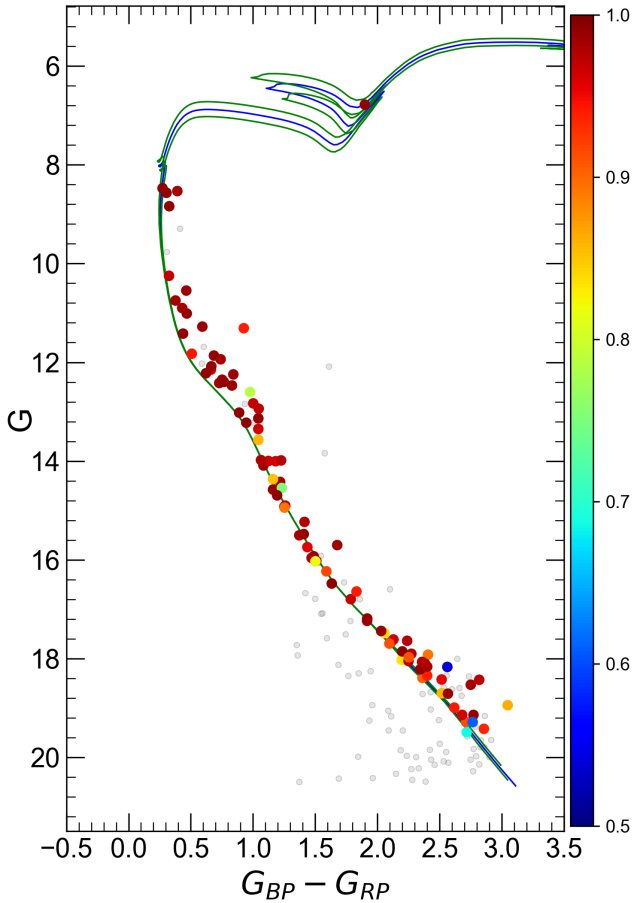


**Figure 7.** Colour-magnitude diagram for the studied cluster Trumpler 2. Different colour scales show the membership probabilities of the most probable cluster members. The scales of memberships are represented on colourbars to the right. Grey-coloured dots identify the stars with probabilities  $P < 0.5$ . The best fitting PARSEC isochrones and their errors are shown as the blue and green lines, respectively. Superimposed isochrone ages match to 110 Myr for Trumpler 2

from Sun as  $d_{\text{iso}} = 686 \pm 49$  pc. The errors in distance modulus and isochrone distance were calculated from the relations presented in Carraro et al. (2017). These relations take into account the photometric magnitude and colour excess with their uncertainties. The estimated isochrone distance is in a good agreement with the values given by different researchers (see Table 1) as well as with the value of trigonometric parallax distance  $d_{\pi} = 687 \pm 27$  pc calculated in this study.

Moreover, we derived Galactocentric coordinates  $(X, Y, Z)_{\odot}$  of Trumpler 2, where  $X$ ,  $Y$ , and  $Z$  are directions toward the Galactic centre in the Galactic disc, the Galactic rotation and the Galactic north pole, respectively. We used isochrone distance, Galactic longitude and latitude of the cluster and calculated these values as  $(X, Y, Z)_{\odot} = (-504, 464, -48)$  pc. These findings are in fair agreement with the results of Cantat-Gaudin et al. (2020) (see also Table 4).

#### 4. SPACE VELOCITIES AND GALACTIC ORBITAL PARAMETERS

Kinematic and dynamical orbit analyses of open clusters are important to understand the birth radii and Galactic populations of these objects (Yontan 2023). In this study we performed orbital integration analyses and obtained the Galactic orbital parameters for Trumpler 2. To do this, we used MWPotential2014 in the Galactic dynamics library GALPY<sup>3</sup> package of Bovy (2015) which is written in Python. The MWPotential2014 model represents the sum of three-component potentials: the spherical bulge as described in Bovy (2015), the Galactic disc as defined by Miyamoto & Nagai (1975) and the massive, spherical dark-matter halo as defined by Navarro et al. (1996). The Galactocentric distance and orbital velocity of Sun were taken as  $R_{\text{gc}} = 8$  kpc and  $V_{\text{rot}} = 220$  km s<sup>-1</sup>, respectively (Bovy 2015; Bovy & Tremaine 2012). The distance from the Galactic plane of the Sun was accepted as  $25 \pm 5$  pc (Jurić et al. 2008).

For the complete integration of the orbit, radial velocity information is one of the necessary parameters to be known. We used the available Gaia DR3 radial velocities of the stars to determine mean radial velocity and its uncertainty for Trumpler 2. To do this, we took into account the most probable member stars with membership probabilities  $P \geq 0.9$ , and the number of these stars are 33. The calculation was based on the weighted average of stars' radial velocities (for equations see Soubiran et al. 2018). Thus, the mean radial velocity was obtained as  $V_{\gamma} = -4.48 \pm 1.11$  km s<sup>-1</sup>. The literature mean radial velocity findings for Trumpler 2 (see also Table 1) are  $-4.12 \pm 0.09$  (Soubiran et al. 2018),  $-6.045 \pm 12.32$  (Zhong et al. 2020),  $-3.990 \pm 0.746$  km s<sup>-1</sup> (Dias et al. 2021) and  $-4.16 \pm 0.02$  km s<sup>-1</sup> (Carrera et al. 2022). The mean radial velocity obtained in this study for Trumpler 2 is within 1 km s<sup>-1</sup> of the values are presented in these literature studies. To carry out the orbit integration, we provide the following parameters as input: the central equatorial coordinates ( $\alpha = 02^{\text{h}}36^{\text{m}}55^{\text{s}}.7$ ,  $\delta = +55^{\circ}54'18''$ ) taken from Cantat-Gaudin et al. (2020), the mean proper-motion components ( $\mu_{\alpha} \cos \delta = 1.494 \pm 0.004$ ,  $\mu_{\delta} = -5.386 \pm 0.005$  mas yr<sup>-1</sup>) estimated in Section 3.2, the isochrone distance ( $d_{\text{iso}} = 686 \pm 49$  pc) from Section 3.3, and the radial velocity ( $V_{\gamma} = -4.48 \pm 1.11$  km s<sup>-1</sup>) calculated in the study (see also Table 4).

We integrated the cluster orbit forward with an integration step of 1 Myr up to 2.5 Gyr in order to derive the cluster's possible current location. Figure 8a shows the 'side view' of the cluster on  $Z \times R_{\text{gc}}$  plane, which indicates the distance from the Galactic plane and the Galactic centre. To estimate the possible birth radius of the Trumpler 2, we performed orbit analyses in the past epoch across a time period equal to its age (110 Myr). The integration procedure was limited to the cluster's age as the potential based uncertainties in time, as

<sup>3</sup> See also <https://galpy.readthedocs.io/en/v1.5.0/>

well as the additional errors in the distance, proper-motion components and radial velocity influence the reliability of the results (Gaia Collaboration et al. 2018; Sariya et al. 2021). Figure 8b indicates the distance of the cluster on the  $R_{gc} \times t$  plane with time. In the figure, the effect of uncertainties in the input parameters on the orbit of Trumpler 2 is represented. The results show that Trumpler 2 has an uncertainty of about 0.08 kpc for its possible birth-radius. These results also indicated that the cluster was formed outside the solar vicinity with a birth radius of 8.71 kpc.

Orbit integration resulted in the following derivation for Trumpler 2: apogalactic ( $R_a = 8752 \pm 107$  pc) and perigalactic ( $R_p = 8438 \pm 10$  pc) distances, eccentricity ( $e = 0.018 \pm 0.007$ ), the maximum vertical distance from Galactic plane ( $Z_{max} = 101 \pm 17$  pc), space velocity components ( $U, V, W = -3.71 \pm 1.32, -12.08 \pm 0.10, -13.81 \pm 1.07$  km  $s^{-1}$ ), and orbital period ( $P_{orb} = 242 \pm 1$  Myr). Taking into account the space velocity component values ( $U, V, W$ ) $_{\odot} = (8.83 \pm 0.24, 14.19 \pm 0.34, 6.57 \pm 0.21)$  km  $s^{-1}$  of Coşkunoglu et al. (2011), we applied a Local Standard of Rest (LSR) correction to the ( $U, V, W$ ) components of Trumpler 2. Hence, we derived the LSR corrected space velocity components as ( $U, V, W$ ) $_{LSR} = (5.12 \pm 1.34, 2.11 \pm 0.35, -7.24 \pm 1.09)$  km  $s^{-1}$ . Using these LSR results, we estimated the total space velocity as  $S_{LSR} = 9.12 \pm 1.76$  km  $s^{-1}$ , which is compatible with the velocity value given for young thin-disc stars (Leggett 1992). Perigalactic and apogalactic distances show that orbit of Trumpler 2 is completely outside the solar circle (Figure 8a). The cluster rises a maximum distance above the Galactic plane

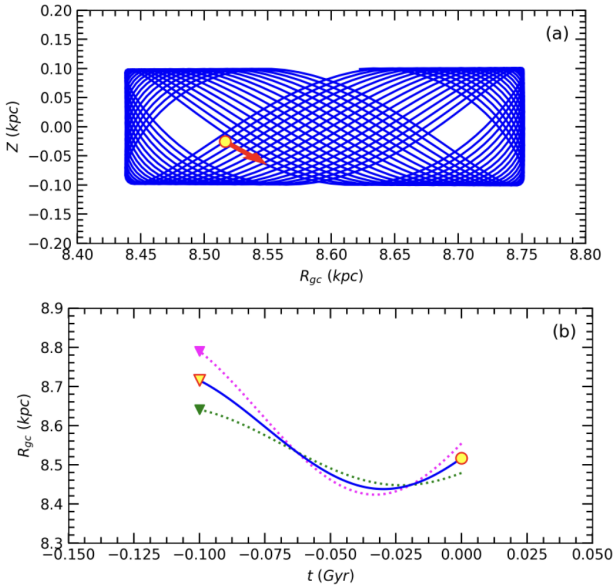


**Figure 8.** The Galactic orbits and birth radii of Trumpler 2 in the  $Z \times R_{gc}$  (a) and  $R_{gc} \times t$  (b) planes. The filled yellow circle and triangles show the present-day and birth positions, respectively. Red arrow is the motion vector of Trumpler 2. The green and pink dotted lines show the orbit when errors in input parameters are considered, while the green and pink filled triangles represent the birth locations of the open cluster based on the lower and upper error estimates.

at  $Z_{max} = 101 \pm 17$  pc, indicating that Trumpler 2 belongs to the thin-disc component of the Milky Way (Bilir et al. 2006a,b, 2008).

## 5. LUMINOSITY AND MASS FUNCTIONS

The distribution of stellar brightness in an open cluster is known as its Luminosity Function (LF). The luminosity function and mass function (MF) are related by well-known mass-luminosity relationships. The correlation between the absolute magnitude and mass of the main-sequence stars can be estimated by a high-degree polynomial equation from the best-fitted age isochrone of the cluster. We used main-sequence stars with probabilities  $P > 0$ , located inside the limiting radius obtained in the study ( $r_{lim}^{obs} = 12$  arcmin) and within the magnitude range  $10 \leq G \leq 19.5$  magnitudes to investigate the LF of Trumpler 2. With these selection criteria, LF analyses were performed from 153 stars. We transformed apparent  $G$  magnitudes of the selected stars into the absolute  $M_G$  magnitudes using the distance modulus equation  $M_G = G - 5 \times \log d + 1.8626 \times E(G_{BP} - G_{RP})$ , where  $G$ ,  $d$  and  $E(G_{BP} - G_{RP})$  are apparent magnitude, isochrone distance, and colour excess that estimated for Trumpler 2 (see also Table 4). We plot as Figure 9 the LF histogram, with a bin width of 1 magnitude. It can be seen from the figure that the absolute magnitude ranges of the used stars lie within the  $-2 < M_G < 11$  magnitude.

The MF was estimated from the LF through the mass-luminosity relation derived from the model isochrones (Bressan et al. 2012) based on the derived age and the previously adopted metallicity fraction ( $z$ ) of the cluster. MF is described by the following expression:

$$\log(dN/dM) = -(1 + \Gamma) \times \log M + C. \quad (5)$$

where  $dN$  denotes the number of stars per unit mass  $dM$ ,  $M$  states the central mass,  $C$  is the constant for the equation, and  $\Gamma$  is the slope of the MF.

We created a high-degree polynomial equation between the

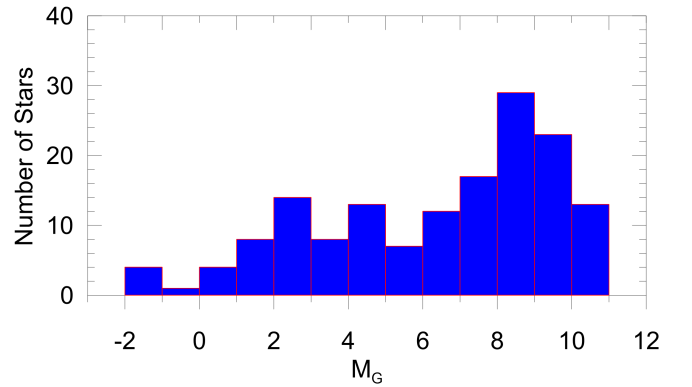


**Figure 9.** The luminosity function based on selected stars ( $P > 0$ ) for Trumpler 2.

G-band absolute magnitudes and masses. Using this equation we transformed the observational absolute magnitudes  $M_G$  of the selected 153 stars ( $P > 0$ ) into masses. With this process, we determined that the mass range of the 153 stars was inside  $0.5 \leq M/M_\odot \leq 3.25$ . Applying equation 5, we derived the MF slope value as  $\Gamma = 1.33 \pm 0.13$  for the cluster, as shown in Figure 10.

In the study, the total mass of the cluster is also examined as a function of the membership probabilities of the stars, as shown in Figure 11. Figure 11a shows the total stellar mass with a bin width of 0.1 membership probabilities ( $\Delta P = 0.1$ ), whereas Figure 11b represents the cumulative values of this distribution. Stars with probabilities  $P > 0.9$  have a total mass of  $106M_\odot$ , while stars with probabilities  $P > 0$  have a total mass of  $162M_\odot$ . Also, when considering the total mass of the stars with probabilities  $P > 0.5$ , the total mass of the cluster is

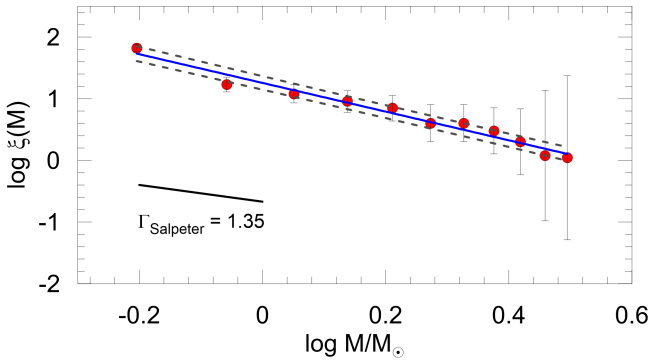


**Figure 10.** Mass function of Trumpler 2. Blue line indicates the calculated mass function of the cluster, whereas black dashed lines present the  $\pm 1\sigma$  standard deviations. Black solid line shows the slope of Salpeter (1955).

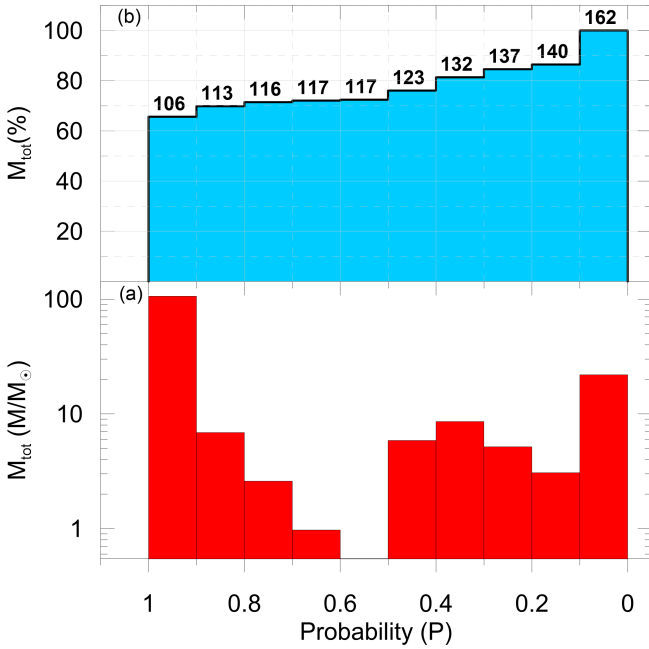


**Figure 11.** Total mass of Trumpler 2 based on membership probabilities (a) and their cumulative masses (b). The numbers above the bins represent the total mass of each bin in the histogram.

$117 M/M_\odot$ , corresponding to 72 per cent of the total mass of stars in all membership probabilities.

## 6. CONCLUSION

We presented photometric, astrometric, and kinematic analyses of open cluster Trumpler 2 using *Gaia* DR3 data. We identified 92 members as the most probable members with probabilities  $P \geq 0.5$  in the direction of the cluster. These stars were used to estimate fundamental astrophysical and Galactic orbit parameters. We obtained age, distance modulus and reddening simultaneously from a *Gaia*-based CMD, whereas the metallicity is taken from the literature Carrera et al. (2022). The results are listed in Table 4. The main outcomes of current study are summarized as follows:

1. We derived structural parameters from the RDP analyses. Analyses concluded that the background stellar density, central stellar density and the core radius values of the cluster are  $f_{bg} = 12.59 \pm 0.02$  stars  $\text{arcmin}^{-2}$ ,  $f_0 = 1.55 \pm 0.33$  stars  $\text{arcmin}^{-2}$  and  $r_c = 2.48 \pm 1.09$  (arcmin), respectively. The limiting radius was determined by the visual eye from RDP fitting. It was adopted as the point where the RDP model matches with the background density level. Accordingly, the value of the limiting radius was concluded to be  $r_{lim}^{obs} = 12$  arcmin.
2. On the basis of the VPD, we estimated mean proper-motion components as  $(\mu_\alpha \cos \delta, \mu_\delta) = (1.494 \pm 0.004, -5.386 \pm 0.005)$  mas  $\text{yr}^{-1}$ .
3. The metallicity value ( $[\text{Fe}/\text{H}] = -0.262 \pm 0.106$  dex) of the cluster was taken from the study of Carrera et al. (2022) and transformed to the mass fraction  $z = 0.0088$  to estimate age and distance modulus.
4. The *Gaia* based colour excess was estimated as  $E(G_{BP} - G_{RP}) = 0.452 \pm 0.019$  mag by comparing the cluster CMD to the theoretical PARSEC isochrone (Bressan et al. 2012) with  $z = 0.0088$ . This value corresponds to a *UBV*-based colour excess to be  $E(B - V) = 0.320 \pm 0.013$  mag via the use of expression  $E(G_{BP} - G_{RP}) = 1.41 \times E(B - V)$  as given by Sun et al. (2021).
5. The isochrone fitting distance to the open cluster Trumpler 2 was derived as  $d_{iso} = 686 \pm 49$  pc. This value is matched well by the distance obtained from the mean trigonometric parallax  $d_\varpi = 687 \pm 27$  pc. The age was evaluated as  $t = 110 \pm 10$  Myr by fitting the isochrone with  $z = 0.0088$  scaled given by Bressan et al. (2012) to the observable CMD.
6. The mass function slope of Trumpler 2 was obtained as  $\Gamma = 1.33 \pm 0.13$ . This slope is in good agreement with the value of 1.35 given by Salpeter (1955). The total mass of Trumpler 2 is about  $162 M/M_\odot$ .
7. Galactic orbit analyses showed that Trumpler 2 is orbiting in a boxy pattern outside the solar circle and belongs to the young thin-disc component of the Milky Way. Moreover, the birth-radius ( $8.71 \pm 0.08$  kpc) indicated that the cluster was formed outside the solar circle.

**Table 4.** Fundamental parameters of Trumpler 2.

Parameter	Value
$(\alpha, \delta)_{J2000}$ (Sexagesimal)	02:36:55.7, +55:54:18
$(l, b)_{J2000}$ (Decimal)	137.3863, -03.9778
$f_0$ (stars arcmin <sup>-2</sup> )	1.55±0.33
$f_{bg}$ (stars arcmin <sup>-2</sup> )	12.59±0.02
$r_c$ (arcmin)	2.48±1.09
$r_{lim}$ (arcmin)	12
$r$ (pc)	2.39
Cluster members ( $P \geq 0.5$ )	92
$\mu_\alpha \cos \delta$ (mas yr <sup>-1</sup> )	1.494 ± 0.004
$\mu_\delta$ (mas yr <sup>-1</sup> )	-5.386 ± 0.005
$\varpi$ (mas)	1.455 ± 0.059
$d_\varpi$ (pc)	687 ± 27
$E(B - V)$ (mag)	0.320 ± 0.013
$E(G_{BP} - G_{RP})$ (mag)	0.452 ± 0.019
$A_G$ (mag)	0.842 ± 0.035
[Fe/H] (dex)	-0.262 ± 0.106*
Age (Myr)	110 ± 10
Distance modulus (mag)	10.027 ± 0.149
Isochrone distance (pc)	686 ± 49
$(X, Y, Z)_\odot$ (pc)	(-504, 464, -48)
$R_{gc}$ (kpc)	8.52
MF slope	1.33 ± 0.13
Total mass ( $M/M_\odot$ )	162
$V_\gamma$ (km s <sup>-1</sup> )	-4.48 ± 1.11
$U_{LSR}$ (km s <sup>-1</sup> )	5.12 ± 1.34
$V_{LSR}$ (kms <sup>-1</sup> )	2.11 ± 0.35
$W_{LSR}$ (kms <sup>-1</sup> )	-7.24 ± 1.09
$S_{LSR}$ (kms <sup>-1</sup> )	9.12 ± 1.76
$R_a$ (pc)	8752 ± 107
$R_p$ (pc)	8438 ± 10
$z_{max}$ (pc)	101 ± 17
$e$	0.018 ± 0.007
$P_{orb}$ (Myr)	242 ± 1
Birthplace (kpc)	8.71 ± 0.08

\*Carrera et al. (2022)

**Peer Review:** Externally peer-reviewed.**Author Contribution:** Conception/Design of study - S.T., T.Y.; Conception/Design of study Data Analysis/Interpretation - S.T., T.Y.; Drafting Manuscript - S.T., T.Y.; Critical Revision of Manuscript - S.T., T.Y.; Final Approval and Accountability - S.T., T.Y.**Conflict of Interest:** Authors declared no conflict of interest.**Financial Disclosure:** Authors declared no financial support.**ACKNOWLEDGEMENTS**

We are grateful to the referees for their valuable feedback, which improved the paper. This study has been supported in part by the Scientific and Technological Research Council (TÜBİTAK) 122F109. This study is a part of the master thesis of Seval Taşdemir. This research has made use of the WEBDA database, operated at the Department of Theoretical Physics and Astrophysics of the Masaryk University. We also made use of NASA's Astrophysics Data System as well as the VizieR and Simbad databases at CDS, Strasbourg, France and data from the European Space Agency (ESA) mission *Gaia*<sup>4</sup>, processed by the *Gaia* Data Processing and Analysis Consortium (DPAC)<sup>5</sup>. Funding for DPAC has been provided by national institutions, in particular, the institutions participating in the *Gaia* Multilateral Agreement.





**LIST OF AUTHOR ORCIDS**S. Taşdemir <https://orcid.org/0000-0003-1339-9148>T. Yontan <https://orcid.org/0000-0002-5657-6194>**REFERENCES**

- Akbulut B., Ak S., Yontan T., Bilir S., Ak T., Banks T., Ulgen E. K., Pautzen E., 2021, *Ap&SS*, 366, 68
- Banks T., Yontan T., Bilir S., Canbay R., 2020, *Journal of Astrophysics and Astronomy*, 41, 6
- Bilir S., Karaali S., Ak S., Yaz E., Hamzaoglu E., 2006a, *New Astron.*, 12, 234
- Bilir S., Karaali S., Gilmore G., 2006b, *MNRAS*, 366, 1295
- Bilir S., Cabrera-Lavers A., Karaali S., Ak S., Yaz E., López-Corredoira M., 2008, *Publ. Astron. Soc. Australia*, 25, 69
- Bisht D., Zhu Q., Yadav R. K. S., Durgapal A., Rangwal G., 2020, *MNRAS*, 494, 607
- Bossini D., et al., 2019, *A&A*, 623, A108
- Bovy J., 2015, *ApJS*, 216, 29
- Bovy J., Tremaine S., 2012, *ApJ*, 756, 89
- Bressan A., Marigo P., Girardi L., Salasnich B., Dal Cero C., Rubele S., Nanni A., 2012, *MNRAS*, 427, 127
- Bukowiecki L., Maciejewski G., Konorski P., Strobel A., 2011, *Acta Astron.*, 61, 231
- Cantat-Gaudin T., Anders F., 2020, *A&A*, 633, A99
- Cantat-Gaudin T., et al., 2018, *A&A*, 618, A93
- Cantat-Gaudin T., et al., 2020, *A&A*, 640, A1
- Carraro G., Sales Silva J. V., Moni Bidin C., Vazquez R. A., 2017, *AJ*, 153, 99
- Carrera R., et al., 2022, *A&A*, 663, A148

<sup>4</sup> <https://www.cosmos.esa.int/gaia><sup>5</sup> <https://www.cosmos.esa.int/web/gaia/dpac/consortium>

- Castro-Ginard A., Jordi C., Luri X., Julbe F., Morvan M., Balaguer-Núñez L., Cantat-Gaudin T., 2018, [A&A](#), 618, A59
- Castro-Ginard A., Jordi C., Luri X., Cantat-Gaudin T., Balaguer-Núñez L., 2019, [A&A](#), 627, A35
- Castro-Ginard A., et al., 2020, [A&A](#), 635, A45
- Coşkunoğlu B., et al., 2011, [MNRAS](#), 412, 1237
- Dias W. S., Monteiro H., Caetano T. C., Lépine J. R. D., Assafin M., Oliveira A. F., 2014, [A&A](#), 564, A79
- Dias W. S., Monteiro H., Moitinho A., Lépine J. R. D., Carraro G., Paunzen E., Alessi B., Vilella L., 2021, [MNRAS](#), 504, 356
- Frolov V. N., Ananjevskaja J. K., Jilinski E. G., Gorshanov D. L., Bronnikova N. M., 2006, [A&A](#), 451, 901
- Gaia Collaboration et al., 2016, [A&A](#), 595, A1
- Gaia Collaboration et al., 2018, [A&A](#), 616, A1
- Gaia Collaboration et al., 2022, [arXiv e-prints](#), p. arXiv:2208.00211
- Joshi Y. C., Dambis A. K., Pandey A. K., Joshi S., 2016, [A&A](#), 593, A116
- Jurić M., et al., 2008, [ApJ](#), 673, 864
- King I., 1962, [AJ](#), 67, 471
- Krone-Martins A., Moitinho A., 2014, [A&A](#), 561, A57
- Lada C. J., Lada E. A., 2003, [ARA&A](#), 41, 57
- Leggett S. K., 1992, [ApJS](#), 82, 351
- Liu L., Pang X., 2019, [ApJS](#), 245, 32
- Miyamoto M., Nagai R., 1975, [PASJ](#), 27, 533
- Navarro J. F., Frenk C. S., White S. D. M., 1996, [ApJ](#), 462, 563
- Paunzen E., Netopil M., Maitzen H. M., Pavlovski K., Schnell A., Zejda M., 2014, [MNRAS](#), 564, A42
- Riello M., et al., 2021, [A&A](#), 649, A3
- Salpeter E. E., 1955, [ApJ](#), 121, 161
- Sariya D. P., et al., 2021, [AJ](#), 161, 101
- Soubiran C., et al., 2018, [A&A](#), 619, A155
- Sun M., Jiang B., Yuan H., Li J., 2021, [ApJS](#), 254, 38
- Trumpler R. J., 1930, [Lick Observatory Bulletin](#), 420, 154
- Wang H., Zhang Y., Zeng X., Hu Q., Liu J., Qin M., Lü G., 2022, [AJ](#), 164, 40
- Yontan T., 2023, [AJ](#), 165, 79
- Zacharias N., Finch C. T., Girard T. M., Henden A., Bartlett J. L., Monet D. G., Zacharias M. I., 2013, [AJ](#), 145, 44
- Zejda M., Paunzen E., Baumann B., Mikulášek Z., Liška J., 2012, [A&A](#), 548, A97
- Zhong J., Chen L., Wu D., Li L., Bai L., Hou J., 2020, [A&A](#), 640, A127

# The Age-Metallicity Relation in the Solar Neighbourhood

S. Döner<sup>1\*</sup> , S. Ak<sup>2</sup> , Ö. Önal Taş<sup>2</sup> , and O. Plevne<sup>2</sup> 

<sup>1</sup>Istanbul University, Institute of Graduate Studies in Science, Programme of Astronomy and Space Sciences, 34116, Beyazit, Istanbul, Türkiye

<sup>2</sup>Istanbul University, Faculty of Science, Department of Astronomy and Space Sciences, 34119, Beyazit, Istanbul, Türkiye

## ABSTRACT

Age-metallicity relation for the Galactic disc is a crucial tool and is used to constrain the Galactic chemical evolution models. We investigated the age-metallicity relation of the Galactic disc using the red giant branch stars in the Solar neighbourhood. The data cover the Galactocentric radius of  $7 \leq R_{gc}(\text{kpc}) \leq 9.5$ , but extends up to 4 kpc in height from the Galactic plane. We used kinematic age derived from highly precise astrometric data of *Gaia* Data Release 2 and element abundance ratios from high-resolution spectroscopic data of APOGEE-2 catalogues. We applied a two-component Gaussian mixture model to chemically separate the programme stars into thin and thick disc populations. The stars in each population are grouped into different distance intervals from the Galactic plane. The mean metal abundances and velocity dispersions of the stars in the groups were calculated and the kinematic ages were determined from their kinematic parameters. We found a steep relation for the thin disc with  $-0.057 \pm 0.007$  dex  $\text{Gyr}^{-1}$ , and even a steeper value of  $-0.103 \pm 0.009$  dex  $\text{Gyr}^{-1}$  for the thick disc. These age-metallicity relations along with the prominent differences in age, metallicity, and kinematic behaviours seen from the data, clearly show that it is important to consider the distinct formation scenarios of the Galactic disc components in modelling the Milky Way.

**Keywords:** Galaxy: solar neighbourhood – disc – structure – stars: red giant branch

## 1. INTRODUCTION

Galactic archaeology is built upon dependable features of stars, and interstellar medium to reconstruct the formation history by considering certain evolutionary scenarios. Features like kinematics, age and chemistry help track the past events of the Galactic formation. It is known that kinematics of a star can change over time due to large scale perturbations and tendency to adapt the surrounding environment. Age of a star can be estimated from the atmosphere model properties using statistical methods or it can be inferred from the kinematic properties once the basic observational parameters are determined precisely. Chemistry of a star changes as a function of time during the Galactic evolution. From the first concrete formation scenarios of ELS (Eggen et al. 1962) and SZ (Searle & Zinn 1978) to sophisticated chemo-dynamic models (i.e. Minchev et al. 2013), our understanding of the Milky Way has evolved with the aid of precise photometric, spectroscopic and astrometric data of hundreds of millions of stars where most lie within the extended Solar neighbourhood ( $< 2$  kpc). This knowledge has enabled us to get a rough idea of the chemical and kinematic behaviours of the stars as we move away from the Galactic centre in all directions within the Milky Way. Accordingly, the stars in the central bulge region are old and their metallicity tends to increase radially away from the Galactic centre and decrease

perpendicularly from the Galactic plane. This suggests that the outer and central parts of the Milky Way were formed earlier than the disk objects (Eggen et al. 1962). This general age trend is followed by inversely related iron and alpha-element abundance ratios, such that older stars have lower iron and higher alpha abundances, as a result of Type II supernova activity, than younger ones. On the other hand, atmospheric abundances of younger stars indicate that iron and alpha element abundance ratios are reversed, as a result of increasing Type Ia supernova activity in our Galaxy. This shows that there is a way to track the evolution of the Milky Way using chemical element abundances, which is the basis of the chemical evolution models.

Chemical evolution has been one of the ways to understand the evolution of the Milky Way disc since its formation. Primordial gas trapped in stars changes with stellar evolution. The gas in the Galaxy becomes a subject to recycled chemical enrichment over time. The formation mass of a star determines the chemical element production yield and the method of recycling of the gas. On one end, if the star is a low-mass the gas trapped inside the star will retain initial chemical diversity for a long time. On the other hand, if the star is massive, then star will produce a variety of chemical elements via nuclear reactions and return the gas with significant change in its chemistry. The overall impact of the recycling process can be

Corresponding Author: S. Döner E-mail: sibeldnr@gmail.com

Submitted: 03.03.2023 • Revision Requested: 27.03.2023 • Last Revision Received: 19.04.2023 • Accepted: 26.04.2023 • Published Online: 10.05.2023



This article is licensed under a Creative Commons Attribution-NonCommercial 4.0 International License (CC BY-NC 4.0)

resolved through an accurate determination of the history of star formation. This mechanism is also responsible for the increase in metallicity in stars, and as such, serves as a measure of time evolution. Elements leave detectable imprints on starlight that can be measured through spectral analysis. This interpretation has already been made by several authors as chemical tagging (Freeman & Bland-Hawthorn 2002) or the chemical clock approach (Chiappini, Matteucci & Gratton 1997). Since the distribution of metallicity has a tendency to evolve in time due to differences of initial mass function across the Galaxy and due to spatial velocities of stars. This provides a unique way to infer the star formation rate, metallicity distribution, amount of gas accretion and supernova activity. Within the last decade, chemical evolution models have been combined with dynamic models to form chemo-dynamic ones, giving greater insight into the Galaxy formation (Minchev et al. 2016).

The last two decades have witnessed major developments in observational astronomy that enlarge our understanding of the Milky Way. The first decade of 2000's were dominated by photometric all sky surveys that prepared the necessary grounds to initiate spectroscopic sky surveys such as GCS (Nordström et al. 2004), RAVE (Steinmetz et al. 2006), BRAVA (Rich et al. 2007), APOGEE (Allende Prieto et al. 2008), SEGUE (Yanny et al. 2009), GES (Gilmore et al. 2012), LAMOST (Zhao et al. 2012), GALAH (De Silva et al. 2015), and GSP-Spec (Recio-Blanco et al. 2022). These surveys made it possible to study the structure, formation and evolution of the Milky Way in depth. Galactic disc formation and evolution studies rely on the observations and theoretical models by means of chemistry, kinematic properties and ages of its main ingredients, i.e. stars, gas and dust. Among these properties the chemical content of up to 20+ elements in the atmospheres of stars in the Solar neighbourhood is obtained more reliably with the aid of high resolution and high signal-to-noise spectroscopic all sky surveys. Kinematic properties of stars can be derived by five astrometric parameters and one spectroscopic parameter, i.e. radial velocity, in which the astrometric ones are now provided by the *Gaia* (Gaia Collaboration et al. 2018).

The first age-metallicity relation (AMR) studies used the *Hipparcos* data of F-G spectral type main-sequence stars. Using these data, Twarog (1980) speculated for the first time that there might be a relation between age and metallicity. Edvardsson et al. (1993) suggested that there exists a wide spread between age and metallicity that implies there may not be such a relation between these parameters. Carraro, Ng & Portinari (1998) analysed the AMR for four different data types, i.e. F-G main-sequence stars, open clusters, synthetic populations and chemical evolution models, then compared the resulting AMRs. In the study, ages were calculated with the synthetic colour-magnitude diagram method using the metallicity, colour excess and distance modulus, while metallicities were determined via spectroscopic and/or photometric methods, which the data regarding were compiled from independent sources in

the literature. They pointed out that AMRs found are unable to explain the existence of old and relatively metal-rich stars and clusters. They found that there is a large spread in metallicity at any age. In another study, Ng & Bertelli (1998) determined a gradient of the AMR as  $-0.07 \text{ dex Gyr}^{-1}$ . In studies that use combined astrometry with Strömgren photometry data of Solar neighbourhood stars (Olsen 1983, 1993), Feltzing, Holmberg & Hurley (2001) found a prominent AMR for a sample of early spectral type stars while no AMR for late-type stars by asserting these stars which have longer lifetime. Nordström et al. (2004) have used the data consisting of around 14,000 main-sequence stars, but despite the sensitivity of their data they claimed that their calculated AMR was dispersed because of the uncertainties. Soubiran et al. (2008) showed no relation between age and metallicity for red giant branch (RGB) stars older than 5 Gyr. Using RAVE DR3 spectroscopic data of F-G spectral type main-sequence stars, Duran et al. (2013) investigated the age and metallicity relation. They have shown that the AMR is related to the spectral type, but not to the population type. Haywood et al. (2013) have studied the AMR in the Galactic disc and found  $-0.025 \text{ dex Gyr}^{-1}$  for the thin disc and  $-0.15 \text{ dex Gyr}^{-1}$  for thick disc sample. Bergemann et al. (2014) used the high-resolution UVES spectra of GES survey to investigate the relationship between age, metallicity and  $\alpha$ -enhancements in F-G main-sequence stars. They claimed a nearly flat AMR for stars younger than 8 Gyr, while no AMR for stars older than 8 Gyr due to the spread in metallicity in the Solar neighbourhood.

Lin et al. (2018) have examined the AMR using 4,000 stars selected from *Gaia* DR1 TGAS catalogue. They have found  $-0.032 \text{ dex Gyr}^{-1}$  of AMR gradient for stars older than 10 Gyr. Wojno et al. (2018) have analyzed 25,000 FGK spectral type main-sequence stars in  $7 < R_{\text{gc}}(\text{kpc}) < 9$  selected from RAVE and TGAS catalogues by separating their sample into low- and high- $\alpha$  sub-samples. This study claims the existence of AMR in both chemical discs. Feuillet et al. (2019) also supports this result. In their study, they have investigated the AMR for iron and  $\alpha$ -element abundance ratios using the RGB stars selected from APOGEE catalogue and *Gaia* DR2 astrometry. They have claimed that there is a significant variation between age and metallicity as a function of current Galactocentric radial and vertical distances from the Galactic centre and Galactic plane, respectively, for the first time. They have suggested that AMR supports the radial migration of stars on the disc plane.

In recent studies, AMR investigations have become more intricate than before due to the contribution of additional element abundance ratios, i.e. iron-peak, alpha-, neutron-capture and s-process elements, from HRS spectra. Casali et al. (2020) have studied relations between  $[X/\text{Fe}]$  and stellar age for 560 solar-like stars in the Solar neighbourhood using their HARPS spectra. They have shown that there are strong correlations between  $[X/\text{Fe}]$  and stellar age with negative slope for s-process elements, a positive slope for  $\alpha$ -elements and nearly flat relation for iron-peak elements. Nissen et al. (2020) have analysed the



relations between 13 element abundance ratios and model ages of 72 solar-like stars with HARPS spectra. They found two sequences in the age-metallicity distribution and have interpreted these as an evidence of gas accretion in two episodes onto the disc. However, they have concluded that there is a need for a deeper study that eliminates the systematic errors in abundance derivation.

An important issue in AMR studies is the estimation of accurate stellar age, which is not a directly measured property. There are various methods to obtain this information. The most popular one depends on the isochrone matching based on the application of Bayes statistics to the observational priors defined from the stellar spectra. This application gives a probability density function (Pont & Eyer 2004; Jørgensen & Lindegren 2005) which helps to define the most likely age. This method provides relatively precise ages ( $\pm 1$  Gyr; Edvardsson et al. 1993; Casagrande et al. 2011; Bensby et al. 2014) for stars in middle spectral types (FGK), because it depends on the precision of stellar evolution tracks and only iron abundance ratios, so far. Theoretical tracks, even though they improve over time, give better results for relatively metal-rich stars. At the upper, and lower limits of the metallicity range  $-2.2 \leq [\text{Fe}/\text{H}](\text{dex}) \leq 0.50$  for PARSEC;  $-4 \leq [\text{Fe}/\text{H}](\text{dex}) \leq 0.45$  for MIST for the Galactic studies, probability density functions are impaired so that stellar age cannot be determined, especially for stars with  $[\text{Fe}/\text{H}] \leq -2.2$  dex. Another age determination method uses astroseismology. However, this method is not applicable to all stars. As a star evolves, its chemical composition changes, affecting the average mass of a particle in a gas, leading to an increase in pressure at a given temperature. This results in a change in the speed of sound. This method measures the speed of sound inside a star by finding the characteristic oscillation frequencies, which gives the age of the star.

Old AMR studies have used early and late spectral type main-sequence stars. The stars spend 90% of their lifetimes in the main sequence stage. Especially, atmospheres of FGK main-sequence stars reflect the chemical properties of their protostellar cloud, so the most reliable metallicity can be inferred from these objects. These objects are fairly common stars in the Solar neighbourhood, since they were targeted in most of the spectroscopic sky surveys. However, these stars cannot provide information from great distances due to their relatively low luminosity. Nevertheless, AMR can be probed in great distances using red giant branch (RGB) stars as stellar tracers instead of main-sequence stars. RGBs are bright objects that reside on the red, metal-rich part of the observational colour-magnitude diagram. An RGB star has an isothermal non-burning helium core with degenerate electrons (Chiosi 1998) and produces core energy from the surrounding shell of it's core and there is a large convective envelope beyond this shell. Red giants are evolved stars which "burn" hydrogen in a shell around an inert helium core (see, Iben 1968). If the mass of the star is sufficiently large,

then this core grows massive enough to initiate helium fusion (Schwarzschild & Selberg 1962). The helium mass in the core continuously increases as it is fed by freshly synthesized helium in the shell, resulting in the star shining brighter over time and the effective temperature continuously decreasing. RGB stars lose mass from their convective envelopes and this causes dust shells to form around them (Origlia et al. 2002; Boyer et al. 2008). This means that age estimation using stellar isochrones with spectroscopic priors becomes an impossible task for RGB stars. On the other hand, HRS spectroscopic data of APOGEE-2 and highly precise *Gaia* astrometric data helps to find other solutions for RGB stars. Spectroscopic and astrometric data can be used to determine the space velocity components and especially their dispersions, which will help to determine stellar ages kinematically (Wielen 1977).

In this study, we present the results on the AMR derived from the RGB stars in the Solar neighbourhood that belong to different chemical Galactic disc components. Section 2 explains the data selection, distance and space velocity estimation. Section 3 describes the chemical separation of RGB stars into disc components and kinematic age derivation. Section 4 deliberates the results for calculated AMRs of chemical discs and Section 5 gives the summary and discussion of the results by comparing with the literature.

## 2. DATA

The AMR for the Milky Way disc is investigated using the Sloan Digital Sky Survey's (SDSS) sixteenth data release (DR16) (Blanton et al. 2017; Ahumada et al. 2020) taken as part of the second, dual hemisphere phase of APOGEE (APOGEE-2) (Majewski et al. 2017). The APOGEE/DR16 dataset includes about 473,307 stars using the two 300-fibre APOGEE spectrographs (Wilson et al. 2019) and the APOGEE survey has near-complete coverage in Galactic longitude, due to the first release of data from Las Campanas Observatory in Chile (Bowen & Vaughan 1973). The APOGEE spectroscopic data reduction pipeline (cf Holtzman et al. 2015; Nidever et al. 2015) supply radial velocity ( $\gamma$ ) and atmospheric model parameters ( $T_{\text{eff}}$ ,  $\log g$ ,  $[\text{Fe}/\text{H}]$ ), while more than 20 different elemental abundances are provided from the APOGEE Stellar Parameters and Chemical Abundances Pipeline (ASPCAP; Holtzman et al. 2018; García Pérez et al. 2016). APOGEE/DR16 data is extracted from high resolution ( $R \sim 22,500$ ) and high signal-to-noise ( $S/N > 100$ ) spectra and complemented with the second data release of *Gaia* (*Gaia* DR2; *Gaia* Collaboration et al. 2018) astrometric and photometric data. So, no additional cross-match is performed between APOGEE-2 and *Gaia* DR2 catalogues. There are 407,266 stars out of 473,307 have all atmospheric model parameters ( $T_{\text{eff}}$ ,  $\log g$ ,  $[\text{Fe}/\text{H}]$ ,  $[\alpha/\text{Fe}]$ ) and trigonometric parallaxes ( $\varpi$ ) in the APOGEE-2 catalogue. These stars cover  $3000 < T_{\text{eff}}(\text{K}) < 9000$  and  $1 < \log g(\text{cgs}) < 6$  intervals on the  $\log g \times T_{\text{eff}}$  plane. Stars with negative parallax values

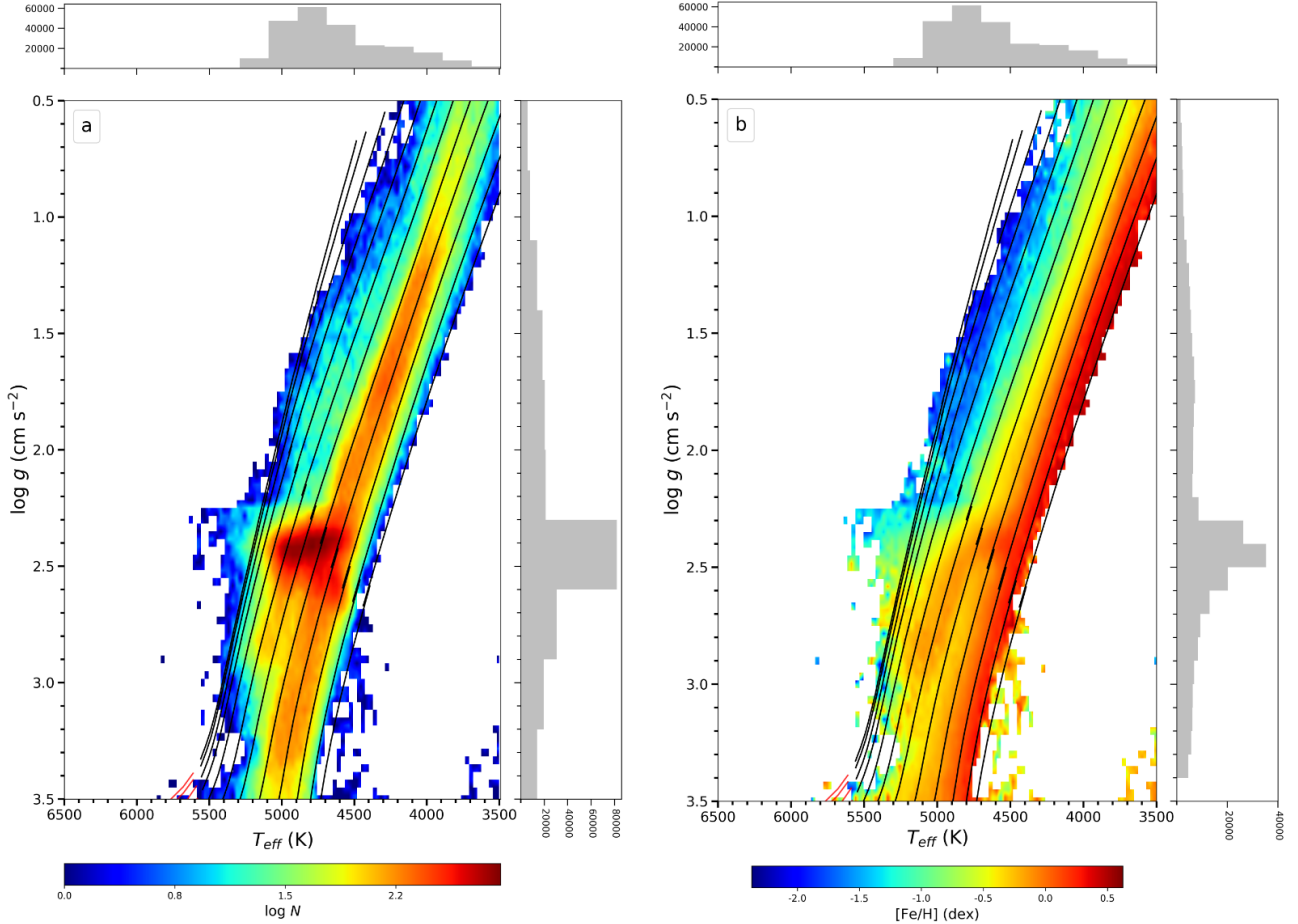


**Figure 1.** Kiel diagrams of the RGB stars colour coded for the stellar number density (a) and the metallicity (b), respectively.  $T_{\text{eff}}$  and  $\log g$  histograms are plotted parallel to apses and ordinate axes in both HR diagrams.

are also eliminated from the sample. In this study, AMR is investigated using RGB stars, which are selected by constraining the data on the effective temperature and the surface gravity plane, i.e.  $3500 < T_{\text{eff}}(\text{K}) < 6500$  and  $0.5 < \log g \text{ (cgs)} < 3.5$ . RGB stars are colour coded by the logarithmic number density (left panel) and the metallicity (right panel) as shown in the Figure 1. In this sample, there are 233,568 objects with  $[\text{Fe}/\text{H}] \geq -2.5$  dex and  $\varpi > 0.1$  mas. PARSEC isochrones (Bressan et al. 2012) are also plotted on the  $\log g \times T_{\text{eff}}$  plane by assuming constant stellar age of 7 Gyr and the PARSEC isochrones are chosen for  $-2.25 < [\text{Fe}/\text{H}](\text{dex}) < 0.5$  metallicity range with 0.25 dex steps. These isochrones are plotted on the Kiel diagram with black-solid lines and it can be seen that these calibrated theoretical models are in good-agreement with observational data. Also in the figure, the  $T_{\text{eff}}$  and  $\log g$  histograms are presented parallel to apses and ordinate axes in both Kiel diagrams. RGB stars in the APOGEE-2 survey have high  $S/N$ , so the  $S/N$  median values at 50%, 68% and 95% of the RGB samples are 175, 125, 75, respectively. The precision in APOGEE-2 radial velocities of RGB stars is around  $\leq 2 \text{ km s}^{-1}$ , so there is no need to put constraints on both  $S/N$  and radial velocity.

Our RGB sample intersects with relatively metal-rich red clump stars, which are easily spotted on the Figure 1's panel (a) as a dark red dense ellipsoidal region. This region is a mixture of ascending red giants, descending red giants after helium flash and stable helium burning red clump stars. We used the technique of Plevne et al. (2020) to determine the contamination of this region by red giant at different level of stellar evolution. In this technique RC stars were determined using the width of half maximum and the standard deviation of the Gaussian distributions on the  $\log g \times T_{\text{eff}}$  plane. Based on this analysis it is found that RGB sample is contaminated only 22% with RC stars according to the  $1\sigma$  of the distribution of stars within the ellipsoid.

The position of 233,568 RGB stars in equatorial and Galactic coordinates are shown in Figure 2. Most of the sources are found on the northern hemisphere. In the southern hemisphere there are relatively small number of sources observed within the APOGEE-2 campaign. Many of the APOGEE-2 stars are observed on the Galactic plane which is the main difference from the other spectroscopic sky surveys. Unlike the position of stars in equatorial coordinates, there are more stars in northern Galactic hemisphere in Galactic coordinates, which is caused

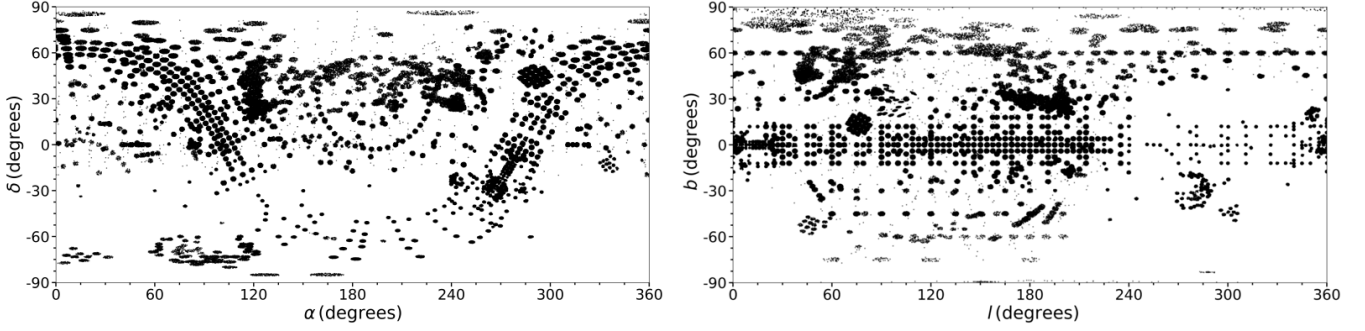


**Figure 2.** The positions of 233,568 RGB stars in Equatorial (left panel) and Galactic (right panel) coordinate systems.

by the  $63^\circ$  difference between two coordinate systems. It shows the regions where  $|b| > 20^\circ$  are surveyed more systematically. There are 142,178 stars in the northern and 91,390 stars in the southern hemisphere. Distance histograms of APOGEE-2 RGB stars are shown for various relative parallax error limits in Figure 3. The sub-samples are obtained for  $\sigma_\varpi/\varpi \leq 0.20, 0.15, 0.10, 0.05, 0.02, 0.01$  and the number of stars is given in the figure. Percentage of the RGB stars corresponding to above relative parallax error limits are 67%, 58%, 45%, 20%, 3% and 0.4%, respectively. So it is preferred to limit the relative parallax errors to 0.1 in order to minimize the errors in distance estimation, which reduces the sample size to 104,241 stars. The RGB sample is further divided into the discrete relative parallax error intervals at 0.05, 0.08 and 0.10, but this time to investigate the dispersed effect and the level of necessity of applying the Lutz & Kelker (1973, LK) bias correction to the *Gaia* DR2 parallaxes. These intervals include 45%, 37% and 18% of the APOGEE-2 RGB samples, respectively. For these discrete sub-samples, the LK corrections, to be applied to the *Gaia* DR2 trigonometric parallaxes that are calculated using Eq. 12 of Smith (1987), are found as  $\leq 1\%$ , 1-2.6% and 2.6-4.3% respectively (see also, Çelebi et al. 2019). Based on these results no LK correction is applied to the trigonometric parallaxes of 104,241 RGB stars.

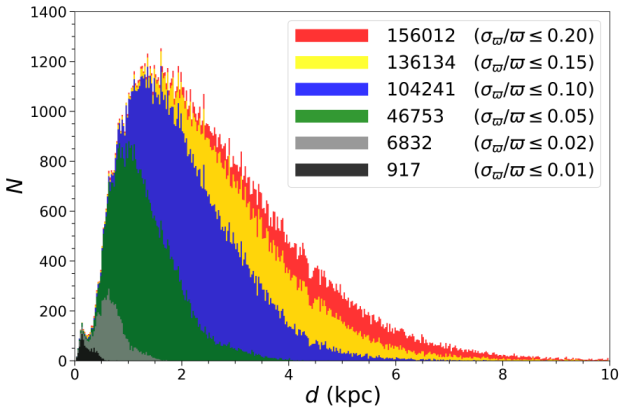


**Figure 3.** Distance histograms of RGB stars based on different relative parallax errors.

## 2.1. Stellar Distances

Stellar distances are obtained using the *Gaia* DR2 trigonometric parallaxes of the RGB stars with two methods; the inverse of trigonometric parallaxes ( $1/\varpi$ ) and Bayesian statistics based on the probability analysis (Bailer-Jones 2015; Bailer-Jones et al. 2018, BJ18). Comparison between stellar distances with  $1/\varpi$  and BJ18 methods and their residuals are shown in Figure 4. Data points are coloured based on the relative parallax errors. The increase in percentages of the RGB stars with the distance is given with the histograms in the upper panel. It is seen that RGB stars reach up to 8 kpc and 87% of the samples lie within 3 kpc distances in the Figure 4. Distances start to deviate from each other at 1 kpc and this becomes apparent at 2 kpc. Similar comparison was performed at Plevne et al. (2020) for their RC sample. The distance difference becomes larger with increasing

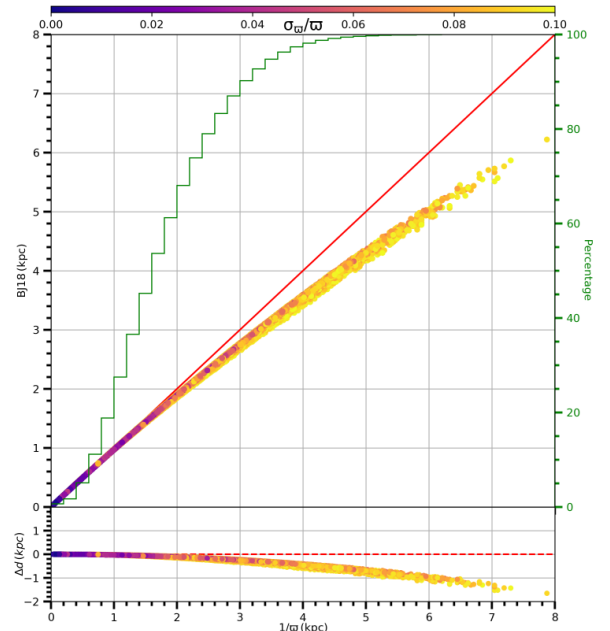


**Figure 4.** Distance comparison between  $1/\varpi$  and BJ18 methods for RGB stars (upper panel). Individual relative parallax errors of RGB stars are represented with colours. Also, on the right y-axis, and on the background the increment of the sample with increasing distances is shown with green step function. The residual distances are shown with  $\langle \Delta \rangle = -0.08$  kpc and  $\sigma(\Delta) = 0.13$  kpc. Red dashed line represents the zero line (lower panel).

distance and reaches to 1 kpc at 6 kpc distance in  $1/\varpi$  scale. The mean residual distance is  $-0.08$  kpc and its dispersion is  $0.13$  kpc. This implies the distance estimation method is not a critical ingredient up to 2 kpc. In order to see the spatial distribution of 104,241 RGB stars, the Heliocentric coordinate components ( $X, Y, Z$ ) are calculated using their Galactic coordinates ( $l, b$ ) and distances ( $d$ ). Heliocentric distance distributions of RC stars on  $Y \times X$  (a) and  $Z \times X$  (b) planes for  $1/\varpi$  methods are given in Figure 5. Figure is colour-coded with the logarithmic number density. Median distance to the Sun and median heliocentric distance components with their respective

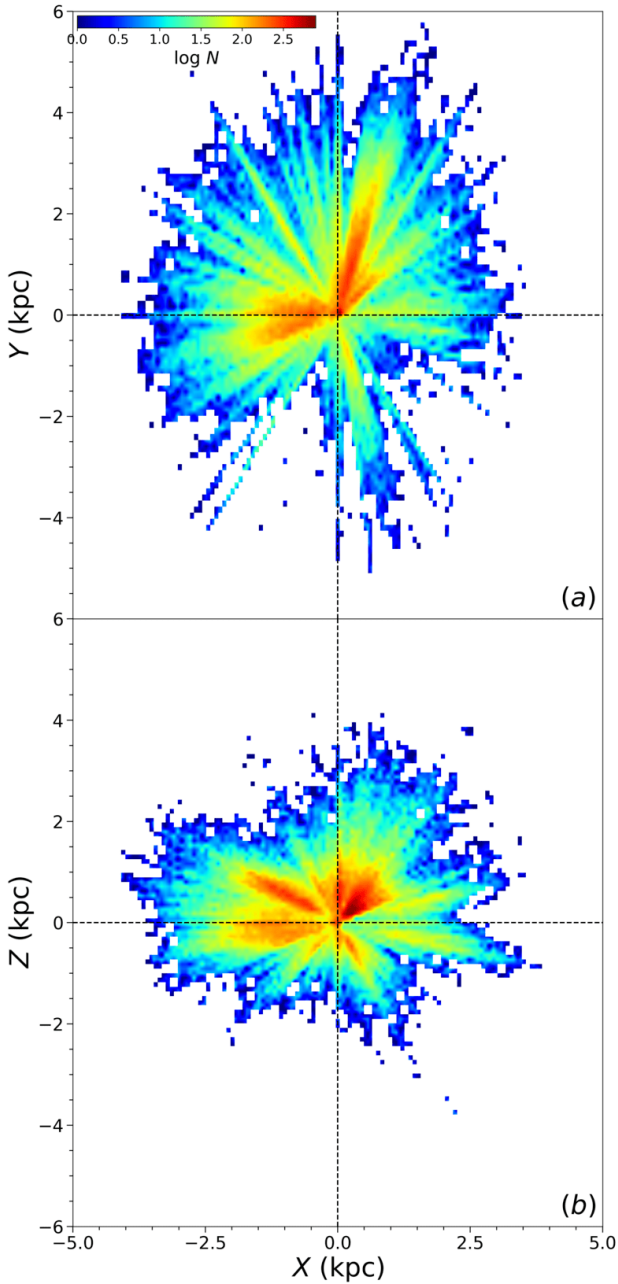


**Figure 5.** Spatial distribution of RGB stars on heliocentric  $Y \times X$  (a) and  $Z \times X$  (b) planes.

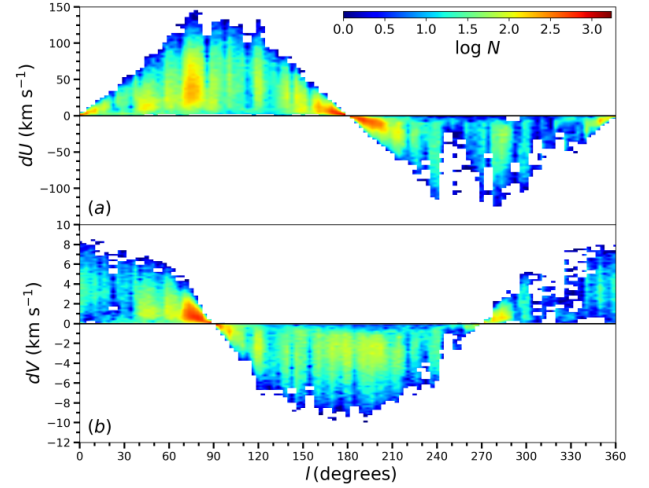


**Figure 6.** Variations of  $dU$  (a) and  $dV$  (b) differential rotation corrections with Galactic longitude.

standard errors are 3.24 kpc and  $(X, Y, Z) = (-0.660 \pm 0.004, +0.440 \pm 0.004, +0.360 \pm 0.003)$  kpc, respectively.

## 2.2. Space Velocity Components

This study is based on the kinematic properties of RGB stars. The accuracy of the kinematic properties is increased with the quality of astrometric data and with the high resolution and  $S/N$  spectroscopic data compiled from known sky surveys. Space velocity components ( $U, V, W$ ) and their respective uncertainties ( $U_{\text{err}}, V_{\text{err}}, W_{\text{err}}$ ) of the RGB sample are calculated using the algorithm and matrices of Johnson & Soderblom (1987) for the J2000 epoch for the right-handed Galactic reference system. This means that  $U$  is positive towards the Galactic centre,  $V$  is in the direction of Galactic rotation, and  $W$  is positive towards the North Galactic Pole. The total space velocity ( $S$ ) for each star is calculated as  $S = \sqrt{U^2 + V^2 + W^2}$ .

Two out of three space velocity components ( $U$  and  $V$ ) are directed parallel to the Galactic plane. Since the Galactic disc rotates differentially starting from around 2 kpc to the outer layers, then  $U$  and  $V$  should be corrected to compensate for the impact on the orbital speeds with these distances from the Galactic centre by applying Mihalas & Binney (1981)'s differential rotation correction formulae. Variations of  $dU$  and  $dV$  with respect to the Galactic longitudes are shown in Figure 6. Calculation shows the differential rotation correction vary between  $-120 < dU(\text{kms}^{-1}) < +150$  and  $-10 < dV(\text{kms}^{-1}) < +10$ . The median distance of the RGB sample shows that this correction is significant. After the correction  $U, V$  and  $W$  components are reduced for the local standard of rest by using the  $(U, V, W)_{\odot} = (8.83 \pm 0.24, 14.19 \pm 0.34, 6.57 \pm 0.21)$   $\text{km s}^{-1}$  values of Coşkunoğlu et al. (2011).

Propagating the uncertainties in radial velocity, trigonometric parallax and proper motion components of RGB stars using Johnson & Soderblom (1987)'s algorithm gives the uncertainty

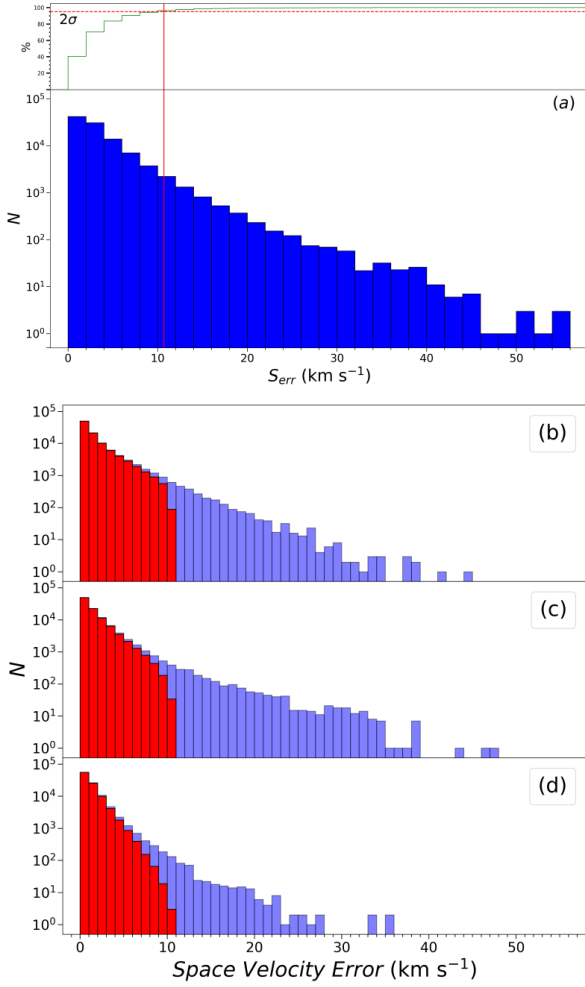


**Figure 7.**  $S_{\text{err}}$  histogram of 104,241 RGB stars and cumulative change of stellar number (a). Red solid line represents the  $2\sigma$  limit on  $S_{\text{err}}$  axis, while red dashed line represents the corresponding number of stars to  $2\sigma$ . Error histograms of space velocity components, i.e.  $U_{\text{err}}$  (b),  $V_{\text{err}}$  (c), and  $W_{\text{err}}$  (d), before (purple) and after (red) the  $S_{\text{err}}=10.68 \text{ km s}^{-1}$  cut-off.

on each space velocity component. Then, the total space velocity error ( $S_{\text{err}}$ ) is obtained from these uncertainties for each star from  $S_{\text{err}} = \sqrt{U_{\text{err}}^2 + V_{\text{err}}^2 + W_{\text{err}}^2}$  relation.  $S_{\text{err}}$  distribution and the cumulative variation of the percentile number of stars and the error histograms of RGB sample are shown in Figure 7. In panel (a), the blue histogram shows the raw distribution of the total space velocity, which reaches up to  $S_{\text{err}} = 60 \text{ km s}^{-1}$ , while the red line represents the  $2\sigma$  value. Step function shows the number of RGB stars with the cumulative increase of RGB stars with  $S_{\text{err}}$ .

Accuracy of the kinematic parameters is enhanced by applying a final constraint on the  $S_{\text{err}}$  distribution. Based on the  $2\sigma$  value of the distribution a cut-off point is defined as  $10.68 \text{ km s}^{-1}$ . Eliminating the stars beyond this cut-off point provides the most sensitive kinematic RGB sample, which is composed of 99,029 stars. Median space velocity errors of this sample are  $(U_{\text{err}}, V_{\text{err}}, W_{\text{err}}) = (1.06 \pm 0.003, 1.06 \pm 0.003, 0.90 \pm 0.003) \text{ km s}^{-1}$ . In panels of Figure 7, distributions of the individual

space velocity component errors ( $U_{\text{err}}, V_{\text{err}}, W_{\text{err}}$ ) are shown before (light-blue histograms) and after (red histograms) the cut-off.

After correcting the space velocity components for the differential rotation and LSR, and constraining the RGB sample for  $S_{\text{err}}$ , the distribution of the space velocity components of 99,029 RGB stars on the  $U_{\text{LSR}} \times V_{\text{LSR}}$  and  $W_{\text{LSR}} \times V_{\text{LSR}}$  planes are shown in Figure 8. The figure is colour coded for logarithmic number density of RGB stars where space velocity components vary  $-200 \leq U_{\text{LSR}} (\text{km s}^{-1}) \leq 200$ ,  $-240 \leq V_{\text{LSR}} (\text{km s}^{-1}) \leq 70$ , and  $-120 \leq W_{\text{LSR}} (\text{km s}^{-1}) \leq 120$  intervals. According to the positions of RGB stars on these planes, stars with small space velocity errors are moving at Solar like velocities. By doing so the velocity dispersion calculations are precise enough to use in age calculations for an AMR investigation. Dispersion of space

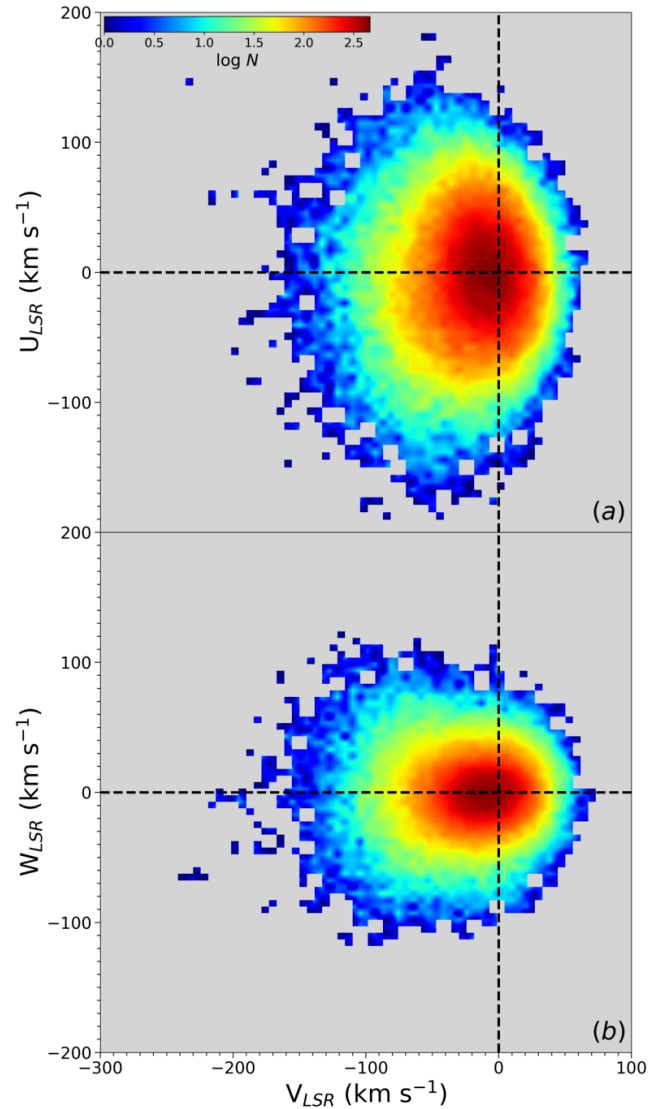


**Figure 8.** Distribution of velocity components of RGB stars on the Galactic planes:  $U_{\text{LSR}} \times V_{\text{LSR}}$  (a) and  $W_{\text{LSR}} \times V_{\text{LSR}}$  (b). RGB stars are colour coded with logarithmic stellar number density. Black dashed-lines in both panels show the centroid of the LSR as  $0 \text{ km s}^{-1}$ .

velocity components ( $\sigma_U$ ,  $\sigma_V$ ,  $\sigma_W$ ) are calculated using Eq. 1 below:

$$\begin{aligned}\sigma_U &= \sqrt{\sum_{i=1}^N \frac{U_i^2}{N} - \left(\sum_{i=1}^N \frac{U_i}{N}\right)^2 - \sum_{i=1}^N \frac{U_{\text{err}_i}^2}{N}}, \\ \sigma_V &= \sqrt{\sum_{i=1}^N \frac{V_i^2}{N} - \left(\sum_{i=1}^N \frac{V_i}{N}\right)^2 - \sum_{i=1}^N \frac{V_{\text{err}_i}^2}{N}}, \\ \sigma_W &= \sqrt{\sum_{i=1}^N \frac{W_i^2}{N} - \left(\sum_{i=1}^N \frac{W_i}{N}\right)^2 - \sum_{i=1}^N \frac{W_{\text{err}_i}^2}{N}}.\end{aligned}\quad (1)$$

here  $U_i$ ,  $V_i$ , and  $W_i$  and  $N$ , represent space velocity components for each star and total number of stars in the stellar sub-sample, respectively.

AMR is investigated on the current Galactocentric radial distance ( $R_{\text{gc}}$ ) from the Galactic centre and current vertical distance ( $Z$ ) from the Galactic plane.  $R_{\text{gc}}$  values of RGB stars are calculated using the formula derived from the geometry (see [Tunçel Güçtekin et al. 2019](#)). The distribution of our RGB sample on  $Z \times R_{\text{gc}}$  plane is shown in Figure 9, where the stars are colour coded according to their metallicity. Galactic plane (at  $Z = 0$ ) and the Solar cylinder ( $7 \leq R_{\text{gc}} \text{ (kpc)} \leq 9$ ) borders are presented with the black dashed lines in Figure 9. In this study, the AMR investigations are focused on the Solar cylinder, where 43,592 RGB stars lie inside these borders. This is the final sample used in AMR analysis. It is noticed that there are three times more stars lie at  $Z > 0$  kpc (32,187 stars) than  $Z \leq 0$  kpc (11,405 stars).

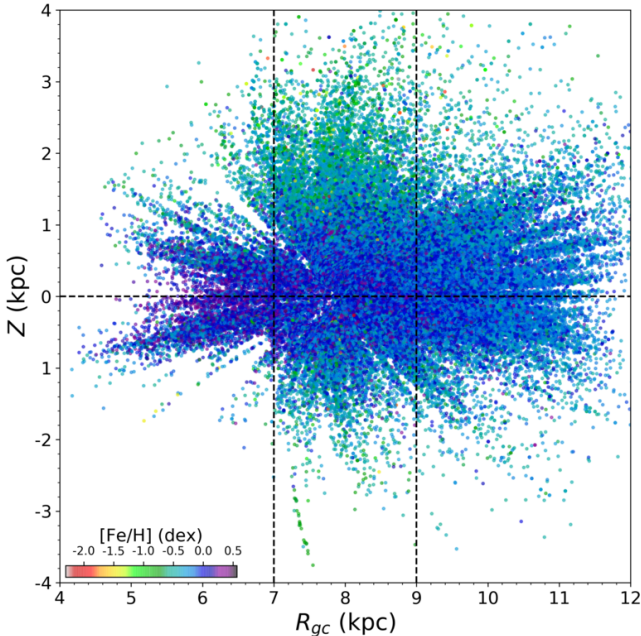


**Figure 9.** Distribution of RGB stars coloured by metallicity on the  $Z \times R_{\text{gc}}$  plane. Vertical dashed lines represent the borders of the solar cylinder ( $7 \leq R_{\text{gc}} \text{ (kpc)} \leq 9$ ) and horizontal dashed lines shows Galactic plane.

### 3. METHODS

This study aims to examine the age and metallicity trends within the Galactic disc. There are strong evidences that the Milky Way disc is composed of overlapping but distinct in nature (age, chemistry and kinematics) sub-components, i.e., thin and thick discs discussed by earlier studies such as [Gilmore & Wyse \(1985\)](#); [Gratton et al. \(1996\)](#); [Fuhrmann \(1998\)](#); [Chiba & Beers \(2000\)](#); [Navarro et al. \(2011\)](#); [Karaali et al. \(2019\)](#); [Plevne et al. \(2020\)](#). In the thin and thick discs, iron and  $\alpha$ -element abundance ratios change towards the radial direction from the Galactic centre or in the vertical direction from the Galactic plane ([Bilir et al. 2006, 2008, 2012](#); [Ak et al. 2007a,b](#); [Cabrera-Lavers et al. 2007](#); [Yaz & Karaali 2010](#)). Distribution of stars on the  $[\alpha/\text{Fe}] \times [\text{Fe}/\text{H}]$  plane is a reflection of the chemical evolution of the Milky Way. Investigations of the chemical evolution of the Galactic disc have shown that the disc has undergone at least two different periods of the formation according to the renowned two infall model of [Chiappini et al. \(1997\)](#). The stars born during these formation periods can be separated on  $[\alpha/\text{Fe}] \times [\text{Fe}/\text{H}]$  plane. It is also known that the chemical abundances plotted on this plane can be used to disentangle the components of the Galactic disc in age ([Wyse & Gilmore 1988](#)).

#### 3.1. Classification of Galactic Populations

To determine Galactic populations, this study made use of Gaussian Mixture Model (GMM), an unsupervised machine learning algorithm which classifies the data by fitting preferred number of Gaussian planes. We applied GMMs to the  $[\alpha/\text{Fe}] \times [\text{Fe}/\text{H}]$  plane of RGB stars. Then, it calculates the probabilities of each Gaussian plane. GMM is applied using *sklearn* version 0.19.1 ([Pedregosa et al. 2011](#)). For more details about the procedure applied in this study, see [Plevne et al. \(2020\)](#). The GMM procedure is applied to 43,592 RGB stars that have  $[\alpha/\text{Fe}]$  and  $[\text{Fe}/\text{H}]$  abundance ratios. Iron abundances range  $-2 \leq [\text{Fe}/\text{H}] \text{ (dex)} \leq 0.5$ , while  $\alpha$  abundances range  $-0.2 \leq [\alpha/\text{Fe}] \text{ (dex)} \leq 0.5$ . Results of GMM on the  $[\alpha/\text{Fe}] \times [\text{Fe}/\text{H}]$  plane is shown in Figure 10. The figure is colour-coded for logarithmic number density, and the black dashed line is the decision boundary line that allows categorising RGB stars to chemical Galactic populations such as low- $[\alpha/\text{Fe}]$  or high- $[\alpha/\text{Fe}]$  population objects (hereafter low- $\alpha$  and high- $\alpha$ , respectively). GMM classification is based on the decision boundary line. According to this, 36,204 stars are classified as low- $\alpha$ , i.e. chemical thin disc, while 7,388 stars are classified as high- $\alpha$ , i.e. chemical thick disc.

#### 3.2. Kinematic Age

Space velocities of stars change systematically causing a departure behaviour from the Galactic plane as a function of their age and radial distance from the Galactic centre. If these stars

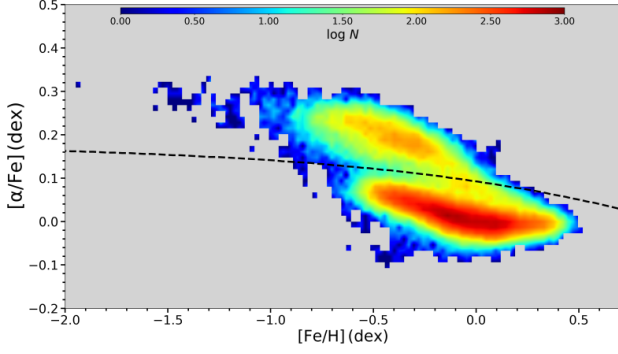


**Figure 10.** Logarithmic number density distribution of 43,592 RGB stars on  $[\alpha/\text{Fe}] \times [\text{Fe}/\text{H}]$  plane. Black dashed line presents the decision boundary obtained with Gaussian mixture model.

are involved with any stellar group, this also increases the total space velocity dispersion and the mean value of the group age. This fact is provided as a base for a new method to obtain the stellar age. As the stars move away from the Galactic plane they also move to a less dense medium, meanwhile, their interaction with surrounding objects increases space velocity  $v$  and decreases the diffusion coefficient (Spitzer & Schwarzschild 1953; Chandrasekhar 1960; Wielen 1977).

Kinematic age estimation is based on the dispersion of true space motions and requires a complete set of space velocity components. Age is calculated from the velocity dispersion of a statistically significant RGB sample using the equation given in Cox (2000), which is the improved version of Wielen (1977)’s study.

$$\sigma_v^3(\tau) = \sigma_{v,\tau=0}^3 + \frac{3}{2} \alpha_V \delta_2 T_\delta \left[ \exp\left(\frac{\tau}{T_\delta}\right) - 1 \right], \quad (2)$$

where,  $\sigma_{v,\tau=0}$  is the velocity dispersion at zero age, which is usually taken as  $10 \text{ km s}^{-1}$  (Cox 2000),  $T_\delta$  is a time scale ( $5 \times 10^9 \text{ yr}$ ),  $\delta_2$  is a diffusion coefficient ( $3.7 \times 10^{-6} (\text{km s}^{-1})^3 \text{ yr}$ ), and  $\alpha_V$  is a parameter describing the rotation curve ( $\approx 2.95$ ).  $\sigma_v(\tau)$  is the total velocity dispersion of the group of RGB.  $\tau$  is the kinematic age of the group. The total dispersion of space velocity vectors is connected to the dispersion of the velocity components as

$$\sigma_v = \sqrt{\sigma_{U_{\text{LSR}}}^2 + \sigma_{V_{\text{LSR}}}^2 + \sigma_{W_{\text{LSR}}}^2}. \quad (3)$$

After computing  $\sigma_v$  from the dispersion of velocity components, it is used in Eq. (2) for computing kinematic age ( $\tau$ ).

## 4. RESULTS AND DISCUSSION

First of all, our sample stars lie within the Solar cylinder ( $7 \leq R_{\text{gc}}(\text{kpc}) \leq 9$ ) that extends up to  $|Z| = 4 \text{ kpc}$ . RGB stars are examined by their kinematics and their chemical properties. GMM model divides the sample into chemical populations which are called low- $\alpha$  (thin disc) high- $\alpha$  (thick disc/halo). Each of the chemical disks separated into the  $Z$  distance intervals. For

each  $Z$  interval the following parameters were calculated: (i) the space velocity components and their respective dispersions, (ii) total space velocity dispersions, (iii) kinematic age and (iv) metallicities. Total velocity dispersions are calculated with Eq. (3), while kinematic ages are calculated with Eq. (2). The space velocity components and the metallicities are determined by the histograms and mean values calculated from the fitted Gaussians. The kinematic and chemical results of the low- $\alpha$  (upper panel) and high- $\alpha$  (lower panel) populations in different  $Z$  distance intervals are listed in Table 1.

### 4.1. AMR for the Low- $\alpha$ Population

The RGB stars are separated into different  $Z$  intervals to probe the variation of the kinematic age with metallicity. Low- $\alpha$  RGB stars are separated with  $0.2 \text{ kpc}$  steps up to  $1 \text{ kpc}$ . Also, there are two more distance intervals that are  $1 \leq |Z| \leq 1.5$  and  $|Z| > 1.5 \text{ kpc}$ .  $U$ ,  $V$  and  $W$  space velocity components and their dispersions are calculated for stars in these distance intervals. Metallicity and space velocity component distributions for each distance intervals and plotted in Figure 11 and Figure 12, respectively. These distributions are presented with blue bars and red solid lines are the Gaussians fitted to the histograms. Mean values ( $\mu$ ) and standard deviations ( $\sigma$ ) are given in each panel. Metallicity follow a Gaussian trend in all panels. It decreases from  $-0.010 \pm 0.002 \text{ dex}$  to  $-0.120 \pm 0.004 \text{ dex}$  as a function of increasing  $|Z|$  distances. According to Table 1, kinematic age and total space velocity dispersion increase, while metallicity and  $V_{\text{LSR}}$  velocity decrease with  $|Z|$ . Kinematic age of RGB stars vary between  $4.37 \pm 0.28$  to  $6.57 \pm 0.26 \text{ Gyr}$ . There is therefore a  $\sim 2.2 \text{ Gyr}$  age difference among the low- $\alpha$  RGB population. Each space velocity component varies in a narrow range when all  $|Z|$  intervals are considered in low- $\alpha$  sub-samples. The mean value of  $V_{\text{LSR}}$  is about  $-9.12 \text{ km s}^{-1}$ , which is in agreement with the mean  $V = -8 \text{ km s}^{-1}$  value of the *Gaia* DR1 TGAS APOGEE sample of Allende Prieto et al. (2016). Moreover, the mean value of  $W_{\text{LSR}} = -1.51 \text{ km s}^{-1}$  is also closer to the  $W = 0 \text{ km s}^{-1}$  velocity of the same study. However, there is a prominent difference between mean  $U_{\text{LSR}}$  value of the two samples. In Allende Prieto et al. (2016)’s study, the space velocity dispersions of each velocity have been investigated for the stars within the Solar cylinder (i.e.  $7.5 \leq R_{\text{gc}}(\text{kpc}) \leq 9.5$ ). They found velocity dispersions of low- $\alpha$  stars at  $|Z| < 0.5 \text{ kpc}$  as  $(\sigma_U, \sigma_V, \sigma_W) = (28, 22, 18) \text{ km s}^{-1}$ . In our study, the mean velocity dispersions of each space velocity component found as  $(\sigma_U, \sigma_V, \sigma_W) = (38, 24, 21) \text{ km s}^{-1}$ . Both studies are in agreement.

### 4.2. AMR for the High- $\alpha$ Population

The same analysis routine is applied to the high- $\alpha$  population for seven subsequent different distance intervals according to Table 1. These intervals increase with  $0.25 \text{ kpc}$  steps up to  $1 \text{ kpc}$ , then there are two more additional distance intervals, i.e.

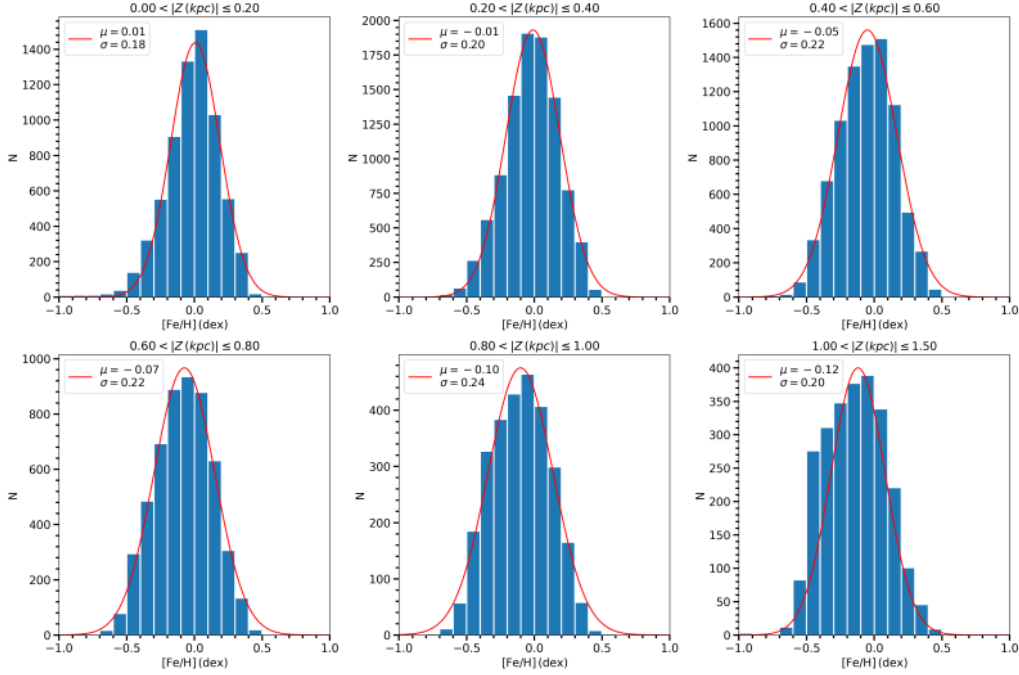


**Figure 11.** Metallicity histograms for low- $\alpha$  population for different  $Z$  distance intervals. Blue bars are the metallicity distributions and red solid lines are the Gaussian fits to distributions in each distance interval.

$1.5 < Z(\text{kpc}) \leq 2$ , and  $2 < Z(\text{kpc}) \leq 5$  (see Figure 13). According to the table, kinematic age and total space velocity dispersion increase, while metallicity and  $V_{\text{LSR}}$  velocity decrease with  $Z$  as these are the expected trends for the Galactic disc (i.e. Boeche et al. 2013). Kinematic age of the RGB stars is  $6.62 \pm 0.18$  Gyr for the high- $\alpha$  stars that are embedded in the Galactic plane ( $|Z| \leq 0.2$  kpc), and age increases to  $8.73 \pm 0.29$  Gyr for stars with  $|Z| > 2$  kpc. There is a  $\sim 2.1$  Gyr age difference among the high- $\alpha$  RGB population. Iron abundance ratios are in agreement with the relatively metal-rich part of the metallicity distribution of the Galactic high- $\alpha$  population, which vary between  $-0.29 \pm 0.010$  to  $-0.49 \pm 0.006$  dex (Figure 13).

For the high- $\alpha$  sample, all of the space velocity components vary in a larger range with respect to the low- $\alpha$  analogues.  $V_{\text{LSR}}$  values fit to the thin disc kinematics up to 1 kpc, then they start to obey the thick disc kinematics (i.e. Chiba & Beers 2000) and  $V_{\text{LSR}}$  reaches to  $-42.33$  km s $^{-1}$  at  $2 < |Z|(\text{kpc}) < 5$  (i.e. Soubiran et al. 2003; Allende Prieto et al. 2016). Distribution of each velocity component for APOGEE-2 RGB stars in each distance interval is given in Figure 14. Based on the figure, velocity distribution in  $U_{\text{LSR}}$  fits to the Gaussian distribution up to 1 kpc, where classical thick disc kinematics become dominant, i.e.  $0.75 < |Z|(\text{kpc}) < 1$  and  $1 < |Z|(\text{kpc}) < 1.5$  intervals. Then, the wings of the distribution start to spread after the  $1 < |Z|(\text{kpc}) < 1.5$  interval. A midly apparent population of stars at  $-200 < U_{\text{LSR}}(\text{km s}^{-1}) < -100$  become prominent in the  $2 < |Z|(\text{kpc}) < 5$  interval.  $V_{\text{LSR}}$  distribution is generally right-skewed and at  $1 < |Z|(\text{kpc}) < 1.5$  interval the left wing of the distribution starts to fill by a

population with  $-200 < V_{\text{LSR}}(\text{km s}^{-1}) < -100$ . Dispersions of each space velocity component for the high- $\alpha$  population,  $(\sigma_U, \sigma_V, \sigma_W) = (42, 28, 39)$  km s $^{-1}$ , are in good agreement with the values for the high- $\alpha$  component in the Solar cylinder of Allende Prieto et al. (2016),  $(\sigma_R, \sigma_\phi, \sigma_Z) = (40, 34, 39)$  km s $^{-1}$ . Difference between  $\sigma_R$  and  $\sigma_U$  or  $\sigma_V$  and  $\sigma_\phi$  values might be caused either by the difference of the definition of the coordinates in heliocentric and Galactic coordinate system or the differential rotation corrections. Metallicity and space velocity component distributions of RGB stars in high- $\alpha$  population are shown for each distance interval in Figure 13 and Figure 14. Distributions of  $[\text{Fe}/\text{H}]$  in  $0 < |Z|(\text{kpc}) < 0.25$  and  $0.25 < |Z|(\text{kpc}) < 0.5$  intervals slightly do not fit to the Gaussian curve. Also, it can be seen from the figure there are contributions to the metal-rich and metal-poor wings in distributions. Metallicity distribution follows the normal distribution at  $0.5 < |Z|(\text{kpc}) < 0.75$  interval. This normal distribution is accompanied with the small contributions to the metal-poor tail of the distribution in the remaining distance intervals up to  $|Z| > 2$  kpc.

Although Galactic disc components have distinct properties in kinematics, chemistry and age, they appear as spatially intertwined structures on  $Z \times R_{\text{gc}}$  plane, which can be seen from Figure 9. This implies the existence of certain stars with thick disc chemistry and thin disc kinematics, as well as other stars with the opposite characteristics. Some of these are old thin disc stars and some are not. Table 1 indicates that regardless of their superposed appearance on the spatial plane, RGB stars have distinct chemistry and age distribution. Also, based on



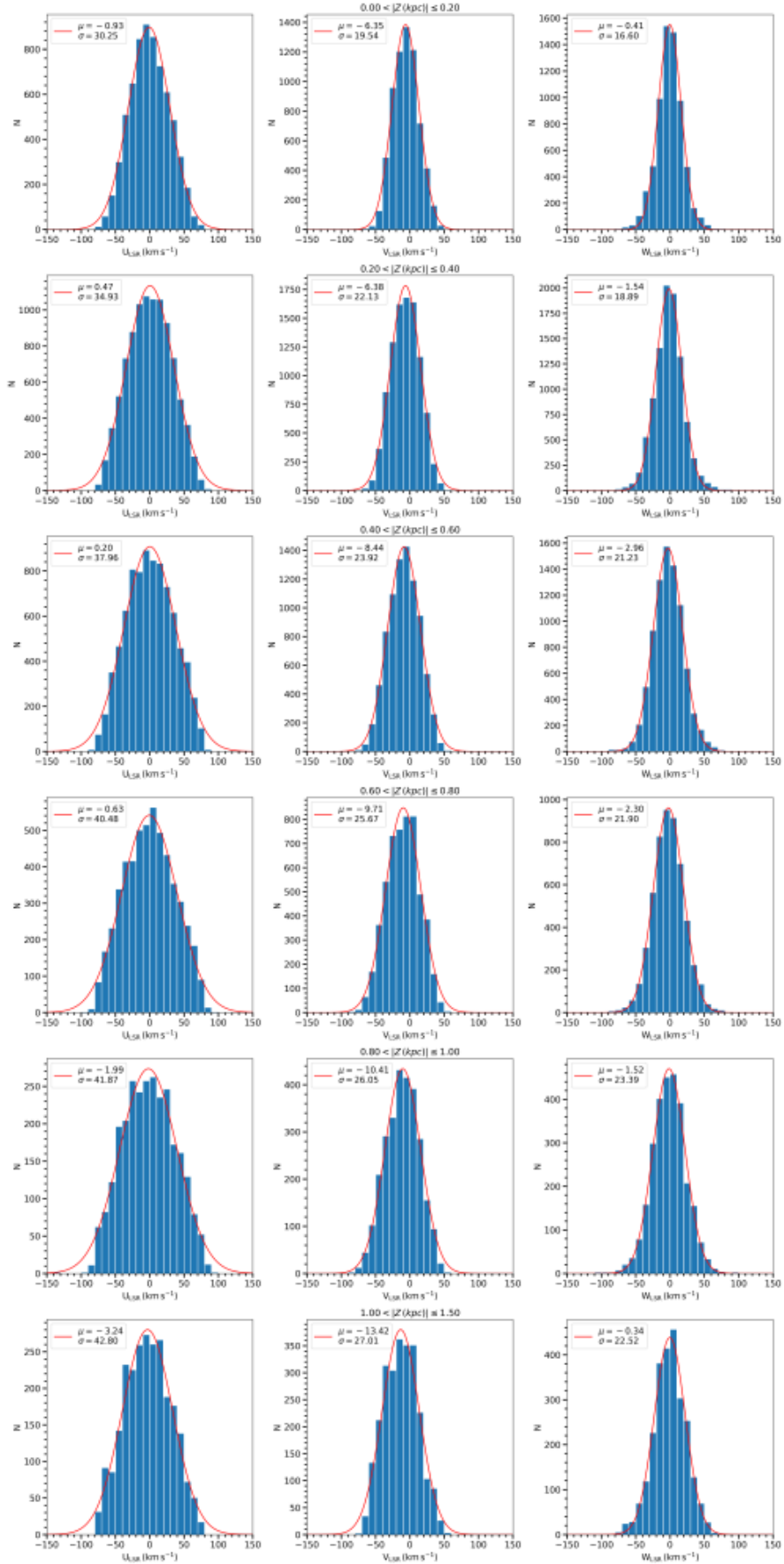


**Figure 12.** Velocity histograms for low- $\alpha$  population for different  $Z$  distance intervals. Blue bars are the velocity distributions and red solid lines are the Gaussian fits to distributions in each distance interval.

**Table 1.** Kinematic properties for the low and high- $\alpha$  populations. Perpendicular distance intervals from the Galactic plane ( $|Z_1 - Z_2|$ ), number of stars ( $N$ ) in each distance interval, LSR corrected space velocity components ( $U_{\text{LSR}}$ ,  $V_{\text{LSR}}$ ,  $W_{\text{LSR}}$ ) and their dispersions ( $\sigma_U$ ,  $\sigma_V$ ,  $\sigma_W$ ), total space velocity dispersion ( $\sigma_{\text{tot}}$ ), kinematic age ( $\tau$ ) and the metallicity ( $[\text{Fe}/\text{H}]$ ) are given in columns, respectively.

low- $[\alpha/\text{Fe}]$ population										
$ Z_1 - Z_2 $ (kpc)	$N$ (stars)	$U_{\text{LSR}}$ (km s $^{-1}$ )	$V_{\text{LSR}}$ (km s $^{-1}$ )	$W_{\text{LSR}}$ (km s $^{-1}$ )	$\sigma_U$ (km s $^{-1}$ )	$\sigma_V$ (km s $^{-1}$ )	$\sigma_W$ (km s $^{-1}$ )	$\sigma_{\text{tot}}$ (km s $^{-1}$ )	$\tau$ (Gyr)	$[\text{Fe}/\text{H}]$ (dex)
0.00-0.20	6691	$-0.93 \pm 1.06$	$-6.35 \pm 0.50$	$-0.41 \pm 0.64$	$30.25 \pm 1.47$	$19.54 \pm 0.60$	$16.60 \pm 0.58$	$39.65 \pm 1.69$	$4.37 \pm 0.28$	$-0.01 \pm 0.002$
0.20-0.40	9687	$+0.47 \pm 1.37$	$-6.38 \pm 0.58$	$-1.54 \pm 0.72$	$34.93 \pm 1.60$	$22.13 \pm 0.63$	$18.89 \pm 0.63$	$45.46 \pm 1.83$	$5.28 \pm 0.26$	$-0.01 \pm 0.002$
0.40-0.60	8401	$+0.20 \pm 1.83$	$-8.44 \pm 0.72$	$-2.96 \pm 0.84$	$37.96 \pm 2.00$	$23.92 \pm 0.66$	$21.23 \pm 0.75$	$49.64 \pm 2.23$	$5.85 \pm 0.30$	$-0.05 \pm 0.002$
0.60-0.80	5341	$-0.63 \pm 2.08$	$-9.71 \pm 0.82$	$-2.30 \pm 0.84$	$40.48 \pm 2.15$	$25.67 \pm 0.72$	$21.90 \pm 0.78$	$52.70 \pm 2.40$	$6.25 \pm 0.30$	$-0.07 \pm 0.003$
0.80-1.00	2785	$-1.99 \pm 2.00$	$-10.41 \pm 0.98$	$-1.52 \pm 0.83$	$41.87 \pm 2.02$	$26.05 \pm 0.84$	$23.39 \pm 0.76$	$54.58 \pm 2.31$	$6.48 \pm 0.28$	$-0.10 \pm 0.005$
1.00-1.50	2505	$-3.24 \pm 2.04$	$-13.42 \pm 1.19$	$-0.34 \pm 0.80$	$42.80 \pm 1.88$	$27.01 \pm 0.94$	$22.52 \pm 0.71$	$55.39 \pm 2.22$	$6.57 \pm 0.26$	$-0.12 \pm 0.004$
> 1.50	794	—	—	—	—	—	—	—	—	—
high- $[\alpha/\text{Fe}]$ population										
$ Z_1 - Z_2 $ (kpc)	$N$ (stars)	$U_{\text{LSR}}$ (km s $^{-1}$ )	$V_{\text{LSR}}$ (km s $^{-1}$ )	$W_{\text{LSR}}$ (km s $^{-1}$ )	$\sigma_U$ (km s $^{-1}$ )	$\sigma_V$ (km s $^{-1}$ )	$\sigma_W$ (km s $^{-1}$ )	$\sigma_{\text{tot}}$ (km s $^{-1}$ )	$\tau$ (Gyr)	$[\text{Fe}/\text{H}]$ (dex)
0.00-0.25	294	$+0.74 \pm 0.92$	$-13.90 \pm 0.54$	$-2.08 \pm 0.84$	$34.93 \pm 1.21$	$23.86 \pm 0.63$	$36.42 \pm 0.74$	$55.82 \pm 1.55$	$6.62 \pm 0.18$	$-0.29 \pm 0.010$
0.25-0.50	839	$-2.24 \pm 1.58$	$-19.06 \pm 0.72$	$-3.17 \pm 0.98$	$38.34 \pm 1.78$	$24.54 \pm 0.67$	$36.40 \pm 0.89$	$58.28 \pm 2.09$	$6.91 \pm 0.24$	$-0.30 \pm 0.007$
0.50-0.75	1093	$+1.47 \pm 1.91$	$-22.32 \pm 0.92$	$-1.57 \pm 1.04$	$39.82 \pm 2.02$	$27.71 \pm 0.79$	$37.27 \pm 0.99$	$61.18 \pm 2.38$	$7.22 \pm 0.25$	$-0.31 \pm 0.006$
0.75-1.00	1086	$+0.09 \pm 1.97$	$-25.92 \pm 1.19$	$-0.73 \pm 0.97$	$43.09 \pm 1.98$	$28.01 \pm 0.98$	$36.57 \pm 0.91$	$63.08 \pm 2.39$	$7.42 \pm 0.25$	$-0.34 \pm 0.006$
1.00-1.50	1952	$-3.03 \pm 2.21$	$-33.31 \pm 1.68$	$-0.85 \pm 1.09$	$44.18 \pm 1.90$	$28.83 \pm 1.28$	$38.09 \pm 1.05$	$65.07 \pm 2.52$	$7.63 \pm 0.25$	$-0.37 \pm 0.005$
1.50-2.00	1078	$+1.83 \pm 2.80$	$-39.99 \pm 2.38$	$-3.46 \pm 1.26$	$44.53 \pm 2.19$	$28.00 \pm 1.61$	$41.96 \pm 1.18$	$67.29 \pm 2.97$	$7.85 \pm 0.29$	$-0.42 \pm 0.006$
> 2.00	1046	$-7.31 \pm 3.62$	$-42.33 \pm 2.99$	$-6.06 \pm 1.48$	$51.46 \pm 2.45$	$33.49 \pm 2.02$	$46.48 \pm 1.28$	$77.01 \pm 3.43$	$8.73 \pm 0.29$	$-0.49 \pm 0.006$

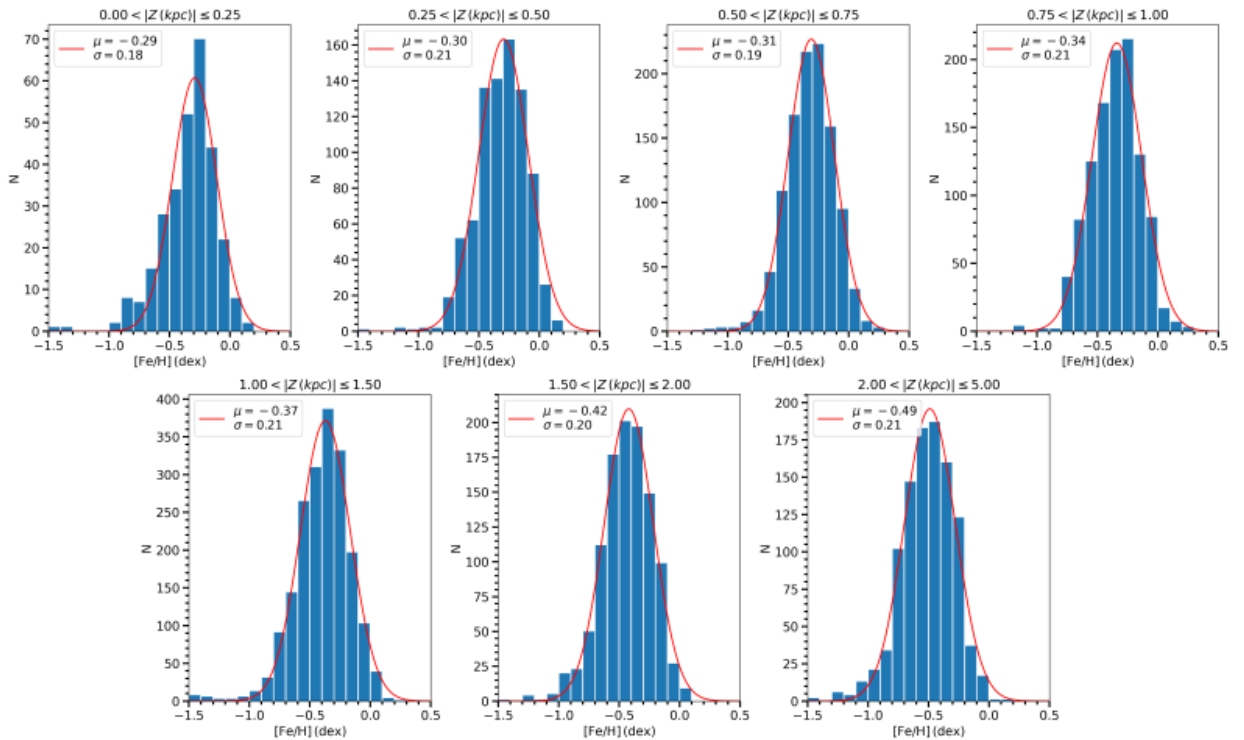


**Figure 13.** Metallicity histograms for high- $\alpha$  population for different  $Z$  distance intervals. Blue bars are the metallicity distributions and red solid lines are the Gaussian fits to distributions in each distance interval.

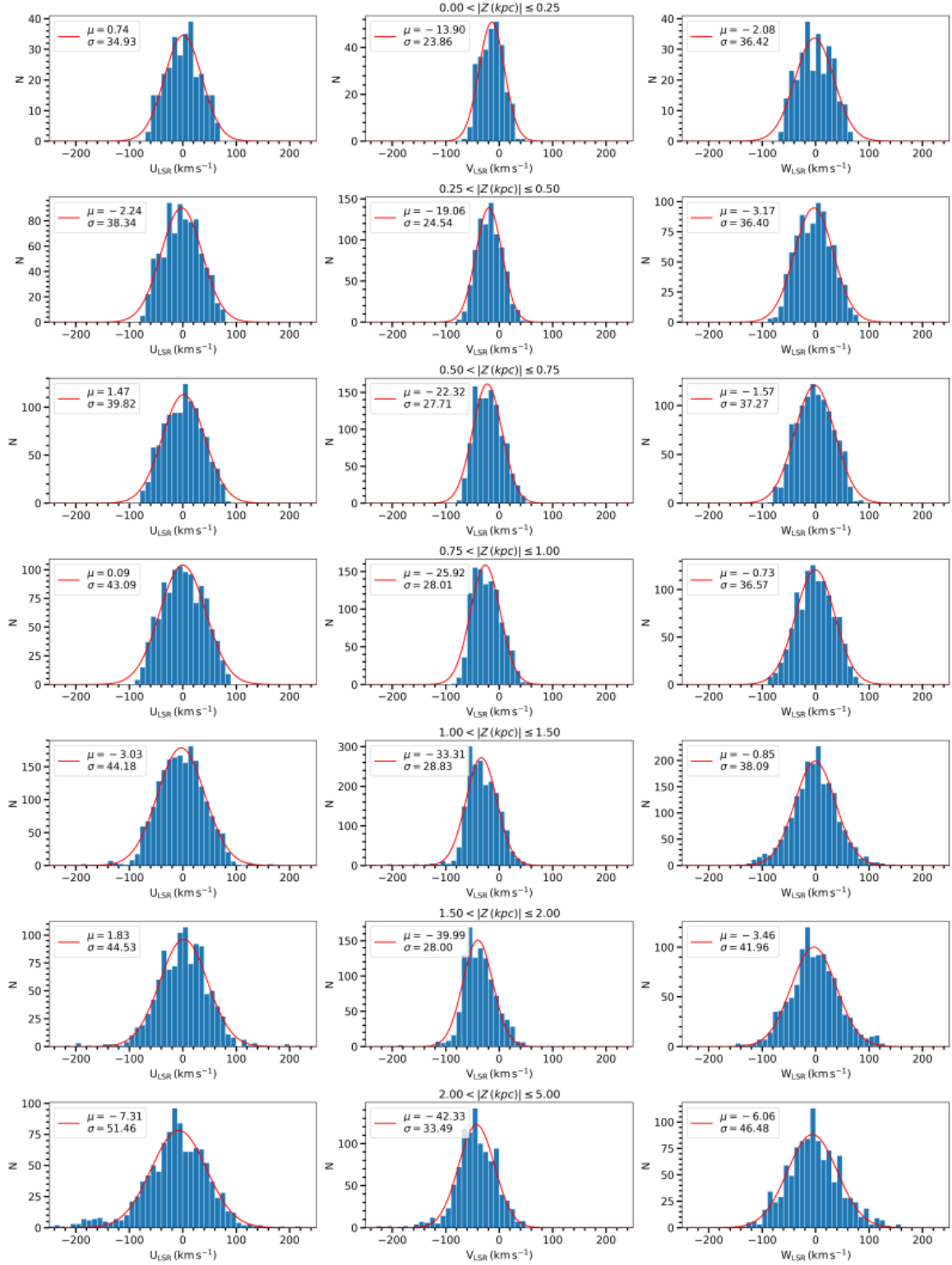


**Figure 14.** Velocity histograms for high- $\alpha$  population for different  $Z$  distance intervals. Blue bars are the velocity distributions and red solid lines are the Gaussian fits to distributions in each distance interval.

the total space velocity dispersions, both components also have distinct characteristics.

Overall results show both Galactic disc components have AMR relations (see Figure 15). AMR are calculated via loci points that represent the  $|Z|$  distance intervals for each Galactic disc component. Each locus point is determined from the age and metallicity parameters of stars in the respective distance interval. Then the linear fits are applied on all of loci points for the thin and thick discs, separately. Blue and red solid lines represent the low- and high- $\alpha$  populations, respectively. The calculated AMR slopes are  $-0.057 \pm 0.007$  dex  $\text{Gyr}^{-1}$  for the low- $\alpha$  population, while it is  $-0.103 \pm 0.009$  dex  $\text{Gyr}^{-1}$  for the high- $\alpha$  population. This study deviates from the literature of AMR derivations a group age from the kinematic data instead of assigning an isochrone-based statistical age from derived observational parameters (e.g. Haywood et al. 2013; Feuillet et al. 2019). Nonetheless our results can be compared with some studies. In one study Haywood et al. (2013) have determined the AMR for thin and thick discs using the HARPS spectroscopy, re-reduced *Hipparcos* parallaxes (van Leeuwen 2007) and isochrone based ages of 1,111 FGK stars. Their result for the thin disc is  $-0.025$  dex  $\text{Gyr}^{-1}$  and for the thick disc is  $-0.15$  dex  $\text{Gyr}^{-1}$ . Haywood et al. (2013) calculated the enrichment rate for the thick disc as around 5-6 times the thin disc. Even though our results seem to be similar in trend to Haywood et al. (2013), the calculated enrichment rates reflects a difference. We found the high- $\alpha$  enrichment rate as  $\sim 1.8$  times that of the low- $\alpha$ . Vertical velocity dispersions of low- and high- $\alpha$  populations correlate with kinematic age. In Figure 15, the first locus of the low- $\alpha$  sample is around the same spot as the Sun, which is  $[\text{Fe}/\text{H}] = 0$  dex and  $\tau = 4.6$  Gyr. So, we cannot provide kinematic age of the stellar group more rich in metallicity based on this analysis even though our sample reaches to  $+0.5$  dex at the metal-rich tail of the metallicity distribution.

The oldest star group in the low- $\alpha$  population has a mean age of 6.57 Gyr and a mean metallicity of  $-0.12$  dex with rotational velocities  $-13.42$  km  $\text{s}^{-1}$ . On the other hand for the high- $\alpha$  population, the youngest group have a mean age of 6.62 Gyr,

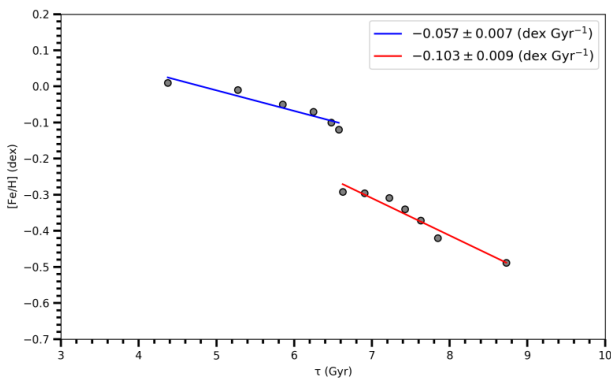


**Figure 15.** Age-metallicity relation for thin (blue line) and thick (red line) disc populations.

metallicity of  $-0.29$  dex and the rotational velocity of  $-13.90$  km  $\text{s}^{-1}$ . Both samples are around the same age and similar in kinematics, but the metallicity differs by 0.15 dex. Difference in chemistry implies that these samples presumably have different origin, and their rotational velocities are almost same. It's because kinematic properties of stars have a tendency adapt to the orbital angular momentum distribution that is shaped by the large scale perturbation sources.

Therefore, there is a kinematic continuum within Galactic disks and a discontinuity between chemical populations, regardless of chemical sub-populations. However, each chemical group has their own chemical continuities from metal rich to metal poor as the vertical distances increase from the Galactic plane. It can be inferred from this result to chemical discs have different origins related to the gas accretion.

## 5. SUMMARY AND CONCLUSION

We have investigated the age-metallicity relation for the Galactic disc using the kinematic properties calculated from the precise astrometric and spectroscopic data of 43,592 RGB stars within the Solar cylinder. Red giant sample is selected using PARSEC stellar evolution tracks. Relative parallax errors are limited to 0.1 and Lutz-Kelker bias is not applied on the trigonometric parallaxes of the sample. Stellar distances are determined via inverse parallax relation. Based on the difference between inverse parallax method and BJ18 methods compared and we have shown that the estimation method is not a crucial tool up to 2 kpc distances. Precise input parameter in kinematic calculations allowed more dependable ages than the ones obtained with the former kinematics data. In the study, Galactic populations are defined using a GMM applied to the  $[\alpha/\text{Fe}] \times [\text{Fe}/\text{H}]$  plane, see Section 3.1. As a result of this method, chemical disk sub-components emerged as low- $\alpha$  and high- $\alpha$  populations, which are akin to the classical thin disc and thick disc/halo, respectively. Each chemical disc component was divided into  $|Z|$  intervals, and they became the loci for AMR calculation.

This study shows there are AMRs for both disc components. Past studies usually found an AMR for the thick disc and no relation for the thin disc due to spread in metallicity. As both the quality and the quantity of the photometric, spectroscopic and the astrometric data are enhanced within the last decade, relations between stellar age-metallicity and stellar age-various elemental ratios immensely investigated with similar, but different methodologies. Moreover, individual stellar age plays the key role on the modelling efforts. We hope the PLANetary Transits and Oscillation of Stars mission (PLATO) (Miglio et al. 2017) shall remove most of the fuzzy parts of the Galactic formation and evolution models by providing excellent age determinations. From the Galactic archaeology point of view, PLATO survey is expected to derive astroseismic ages for red giant stars with a 10% precision.

**Peer Review:** Externally peer-reviewed.

**Author Contribution:** Conception/Design of study - S.A., S.D.; Data Acquisition - S.D., O.P.; Data Analysis/Interpretation - S.D., O.P., S.A.; Drafting Manuscript - Ö.Ö.T., S.A.; Critical Revision of Manuscript - Ö.Ö.T., S.A.; Final Approval and Accountability - S.A., Ö.Ö.T., O.P., S.D.; Technical or Material Support - O.P.; Supervision - S.A.

**Conflict of Interest:** Authors declared no conflict of interest.

**Financial Disclosure:** Authors declared no financial support.

## 6. ACKNOWLEDGEMENTS

We thank the referee for his/her insightful and constructive suggestions, which significantly improved the paper. This study is related to Sibel Döner's MSc thesis. This work has been supported by the Scientific and Technological Research Council of Turkey (TÜBİTAK), Grant No: MFAG-118F350. We have also made use of data from the APOGEE survey, which is part of Sloan Digital Sky Survey IV. SDSS-V is managed by the Astrophysical Research Consortium for the Participating Institutions of the SDSS Collaboration (<http://www.sdss.org>). This work has made use of data from the European Space Agency (ESA) mission *Gaia* (<https://www.cosmos.esa.int/gaia>), processed by the *Gaia*Data Processing and Analysis Consortium (DPAC, <https://www.cosmos.esa.int/web/gaia/dpac/consortium>). Funding for the DPAC has been provided by national institutions, in particular the institutions participating in the *Gaia* Multilateral Agreement. This research has made use of NASA's Astrophysics Data System Bibliographic Services.

## LIST OF AUTHOR ORCIDS

S. Döner <https://orcid.org/0000-0001-7922-8961>  
 S. Ak <https://orcid.org/0000-0002-0912-6019>  
 Ö. Önal Taş <https://orcid.org/0000-0003-0864-1921>  
 O. Plevne <https://orcid.org/0000-0002-0435-4493>

## REFERENCES

- Ahumada R., et al., 2020, *ApJS*, 249, 3  
 Ak S., Bilir S., Karaali S., Buser R., Cabrera-Lavers A., 2007a, *New Astronomy*, 12, 605  
 Ak S., Bilir S., Karaali S., Buser R., 2007b, *Astronomische Nachrichten*, 328, 169  
 Allende Prieto C., et al., 2008, *Astronomische Nachrichten*, 329, 1018  
 Allende Prieto C., Kawata D., Cropper M., 2016, *A&A*, 596, A98  
 Bailer-Jones C. A. L., 2015, *PASP*, 127, 994  
 Bailer-Jones C. A. L., Rybizki J., Foesneau M., Mantelet G., Andrae R., 2018, *AJ*, 156, 58  
 Bensby T., Feltzing S., Oey M. S., 2014, *A&A*, 562, A71  
 Bergemann M., et al., 2014, *A&A*, 565, A89  
 Bilir S., Karaali S., Ak S., Yaz E., Hamzaoğlu E., 2006, *New Astronomy*, 12, 234  
 Bilir S., Cabrera-Lavers A., Karaali S., Ak S., Yaz E., López-Corrodoira M., 2008, *Publ. Astron. Soc. Australia*, 25, 69  
 Bilir S., Karaali S., Ak S., Önal Ö., Dağtekin N. D., Yontan T., Gilmore G., Seabroke G. M., 2012, *MNRAS*, 421, 3362  
 Blanton M. R., et al., 2017, *AJ*, 154, 28  
 Boeche C., et al., 2013, *A&A*, 553, A19  
 Bowen I. S., Vaughan A. H. J., 1973, *Appl. Opt.*, 12, 1430  
 Boyer M. L., McDonald I., van Loon J. T., Woodward C. E., Gehrz R. D., Evans A., Dupree A. K., 2008, *AJ*, 135, 1395  
 Bressan A., Marigo P., Girardi L., Salasnich B., Dal Cero C., Rubele S., Nanni A., 2012, *MNRAS*, 427, 127  
 Cabrera-Lavers A., Bilir S., Ak S., Yaz E., López-Corrodoira M., 2007, *A&A*, 464, 565  
 Carraro G., Ng Y. K., Portinari L., 1998, *MNRAS*, 296, 1045  
 Casagrande L., Schönrich R., Asplund M., Cassisi S., Ramírez I., Meléndez J., Bensby T., Feltzing S., 2011, *A&A*, 530, A138  
 Casali G., et al., 2020, *A&A*, 639, A127  
 Chandrasekhar S., 1960, Principles of stellar dynamics  
 Chiappini C., Matteucci F., Gratton R., 1997, *ApJ*, 477, 765  
 Chiba M., Beers T. C., 2000, *AJ*, 119, 2843  
 Chiosi C., 1998, in Aparicio A., Herrero A., Sánchez F., eds, Stellar astrophysics for the local group: VIII Canary Islands Winter School of Astrophysics. p. 1  
 Coşkunoğlu B., et al., 2011, *MNRAS*, 412, 1237  
 Cox A. N., 2000, Allen's astrophysical quantities  
 De Silva G. M., et al., 2015, *MNRAS*, 449, 2604  
 Duran Ş., Ak S., Bilir S., Karaali S., Ak T., Bostancı Z. F., Coşkunoğlu B., 2013, *Publ. Astron. Soc. Australia*, 30, e043  
 Edvardsson B., Andersen J., Gustafsson B., Lambert D. L., Nissen P. E., Tomkin J., 1993, *A&A*, 275, 101  
 Eggen O. J., Lynden-Bell D., Sandage A. R., 1962, *ApJ*, 136, 748  
 Feltzing S., Holmberg J., Hurley J. R., 2001, *A&A*, 377, 911  
 Feuillet D. K., Frankel N., Lind K., Frinchaboy P. M., García-Hernández D. A., Lane R. R., Nitschelm C., Roman-Lopes A., 2019, *MNRAS*, 489, 1742  
 Freeman K., Bland-Hawthorn J., 2002, *ARA&A*, 40, 487  
 Fuhrmann K., 1998, *A&A*, 338, 161  
 Gaia Collaboration et al., 2018, *A&A*, 616, A1  
 García Pérez A. E., et al., 2016, *AJ*, 151, 144  
 Gilmore G., Wyse R. F. G., 1985, *AJ*, 90, 2015  
 Gilmore G., et al., 2012, *The Messenger*, 147, 25  
 Gratton R., Carretta E., Matteucci F., Sneden C., 1996, in Morrison H. L., Sarajedini A., eds, Astronomical Society of the Pacific Conference Series Vol. 92, Formation of the Galactic Halo...Inside and Out. p. 307  
 Haywood M., Di Matteo P., Lehnert M. D., Katz D., Gómez A., 2013, *A&A*, 560, A109  
 Holtzman J. A., et al., 2015, *AJ*, 150, 148  
 Holtzman J. A., et al., 2018, *AJ*, 156, 125  
 Iben Icko J., 1968, *ApJ*, 154, 581  
 Johnson D. R. H., Soderblom D. R., 1987, *AJ*, 93, 864  
 Jørgensen B. R., Lindegren L., 2005, *A&A*, 436, 127

- Karaali S., Bilir S., Gökçe E. Y., Plevne O., 2019, [Publ. Astron. Soc. Australia](#), 36, e040
- Lin J., Dotter A., Ting Y.-S., Asplund M., 2018, [MNRAS](#), 477, 2966
- Lutz T. E., Kelker D. H., 1973, [PASP](#), 85, 573
- Majewski S. R., et al., 2017, [AJ](#), 154, 94
- Miglio A., et al., 2017, [Astronomische Nachrichten](#), 338, 644
- Mihalas D., Binney J., 1981, Galactic astronomy. Structure and kinematics
- Minchev I., Chiappini C., Martig M., 2013, [A&A](#), 558, A9
- Minchev I., Chiappini C., Martig M., 2016, [Astronomische Nachrichten](#), 337, 944
- Navarro J. F., Abadi M. G., Venn K. A., Freeman K. C., Anguiano B., 2011, [MNRAS](#), 412, 1203
- Ng Y. K., Bertelli G., 1998, [A&A](#), 329, 943
- Nidever D. L., et al., 2015, [AJ](#), 150, 173
- Nissen P. E., Christensen-Dalsgaard J., Mosumgaard J. R., Silva Aguirre V., Spitoni E., Verma K., 2020, [A&A](#), 640, A81
- Nordström B., et al., 2004, [A&A](#), 418, 989
- Olsen E. H., 1983, [A&AS](#), 54, 55
- Olsen E. H., 1993, [A&AS](#), 102, 89
- Origlia L., Ferraro F. R., Fusi Pecci F., Rood R. T., 2002, [ApJ](#), 571, 458
- Pedregosa F., et al., 2011, [Journal of Machine Learning Research](#), 12, 2825
- Plevne O., Önal Taş Ö., Bilir S., Seabroke G. M., 2020, [ApJ](#), 893, 108
- Pont F., Eyer L., 2004, [MNRAS](#), 351, 487
- Recio-Blanco A., et al., 2022, [arXiv e-prints](#), p. arXiv:2206.05541
- Rich R. M., Reitzel D. B., Howard C. D., Zhao H., 2007, [ApJ](#), 658, L29
- Schwarzschild I. M., Selberg H., 1962, [ApJ](#), 136, 150
- Searle L., Zinn R., 1978, [ApJ](#), 225, 357
- Smith H. J., 1987, [A&A](#), 188, 233
- Soubiran C., Bienaymé O., Siebert A., 2003, [A&A](#), 398, 141
- Soubiran C., Bienaymé O., Mishenina T. V., Kovtyukh V. V., 2008, [A&A](#), 480, 91
- Spitzer Lyman J., Schwarzschild M., 1953, [ApJ](#), 118, 106
- Steinmetz M., et al., 2006, [AJ](#), 132, 1645
- Tunçel Güçtekin S., Bilir S., Karaali S., Plevne O., Ak S., 2019, [Advances in Space Research](#), 63, 1360
- Twarog B. A., 1980, [ApJ](#), 242, 242
- Wielen R., 1977, [A&A](#), 60, 263
- Wilson J. C., et al., 2019, [PASP](#), 131, 055001
- Wojno J., et al., 2018, [MNRAS](#), 477, 5612
- Wyse R. F. G., Gilmore G., 1988, [AJ](#), 95, 1404
- Yanny B., et al., 2009, [AJ](#), 137, 4377
- Yaz E., Karaali S., 2010, [New Astronomy](#), 15, 234
- Zhao G., Zhao Y.-H., Chu Y.-Q., Jing Y.-P., Deng L.-C., 2012, [Research in Astronomy and Astrophysics](#), 12, 723
- Çelebi M., Bilir S., Ak S., Ak T., Bostancı Z. F., Yontan T., 2019, [Ap&SS](#), 364, 172
- van Leeuwen F., 2007, [A&A](#), 474, 653

# Band Profile and Surface Acoustic Wave Attenuation Analysis of Polygonal Cavity-type Piezoelectric Phononic Crystals

F. Kuruoğlu<sup>1\*</sup>, N. S. Genç<sup>1</sup>, A. Erol<sup>1</sup>, and A. Çiçek<sup>2</sup>

<sup>1</sup>Istanbul University, Faculty of Science, Department of Physics, Vezneciler, 34134, Istanbul, Türkiye

<sup>2</sup>Burdur Mehmet Akif Ersoy University, Faculty of Arts and Science, Department of Nanoscience and Nanotechnology, 15030, Burdur, Türkiye

## ABSTRACT

In this study, we examined the dispersion profiles and surface acoustic wave attenuation properties of polygonal cavity-type phononic crystals in relation to changes in the number of vertices. Both band analysis and transmission spectrum calculations are performed using finite element method simulations. The findings indicate an increase in the number of vertices of phononic crystal results in an increase in local resonance bandgap frequencies and corresponding transmission peaks. Furthermore, the phononic crystal bandgap widens from 7.3 MHz to 11.1 MHz as the number of vertices increases from 3 to 14, as demonstrated by the obtained dispersion profiles. Comparable features are observed in the transmission spectra for alternating polygonal cavity-type phononic crystal periodic grooves. Additionally, the ability of the surface acoustic wave attenuation is affected by the phononic crystal shape, and the resonance frequency of the phononic crystals can be adjusted by changing the number of vertices.

**Keywords:** Surface acoustic wave – phononic crystal – metasurface – Finite element method – phononic bandgap

## 1. INTRODUCTION

The ability to manipulate biological or inorganic objects without physical contact has long been a desired goal. Electromagnetic and acoustic waves have emerged as the most effective means to achieve this aim (Collins et al. 2016). Surface acoustic waves (SAWs) have gained significant attention in various research and application areas, including delay lines (Topaltzikis et al. 2021), filters (Su et al. 2021b,a), microfluidics (Xie et al. 2020; Qian et al. 2020; Agostini et al. 2019), gas-detection (Kumar & Prajesh 2022; Hekiem et al. 2021), mass detection (Wang et al. 2019), and bio-detection (Zhang et al. 2015; Kidakova et al. 2020) applications. The widespread use of SAW devices arises from their versatility across different fields of research and application. Phononic crystals (PnCs) are structures that offer acoustic bandgaps based on the material's periodicity and geometry, similar to photonic crystal slabs (Kushwaha et al. 1994; Sigalas & Economou 1993; Mead 1996; Kushwaha et al. 1993; Guo et al. 2023; Li et al. 2020). Pillar arrays have emerged as the most prominent geometry for PnCs, with a broad range of application areas (Achaoui et al. 2011, 2013; Jin et al. 2021). Piezoelectric phononic crystals (PPnCs) have also gained attention due to their physical properties and applications in waveguiding (Oh et al. 2011; Vasseur et al. 2007; Zhang et al. 2020; Korozlu et al. 2022), bio and mass sensing (Gharibi et al.

2019; Gharibi & Mehaneq 2021; Schmidt et al. 2016), energy harvesting (Cao et al. 2019), and microfluidics (Bourquin et al. (2011)). The geometric parameters of PPnCs, such as locally resonance and/or Bragg bandgap, determine their performance and versatility.

Recent studies have shown that using cavity-shaped metamaterials as piezoelectric phononic crystals can lead to broader SAW bandgaps (Ash et al. 2017; Pouya & Nash 2021). The geometrical parameters, including cavity radius, pillar height, and groove depth, play a crucial role in determining the frequency range where the phononic crystal will be effective (Kuruoğlu 2022). Therefore, obtaining the proper geometrical parameters and understanding their effects on the acoustic bandgap is crucial for superior phononic device applications.

In this paper, we introduce the band profile and the SAW attenuation characteristics of the PPnCs, which have been modelled with the various number of vertices from  $n=3$  to  $n=14$ . A series of Finite Element Method (FEM) simulations were conducted to analyze and correlate the acoustic field behaviour based on the number of pillar vertices of the PPnCs by using the *COMSOL Multiphysics Software*.

**Corresponding Author:** F. Kuruoğlu E-mail: furkan.kuruoglu@istanbul.edu.tr

Submitted: 28.04.2023 • Revision Requested: 17.05.2023 • Last Revision Received: 19.05.2023 • Accepted: 22.05.2023 • Published Online: 25.05.2023



This article is licensed under a Creative Commons Attribution-NonCommercial 4.0 International License (CC BY-NC 4.0)

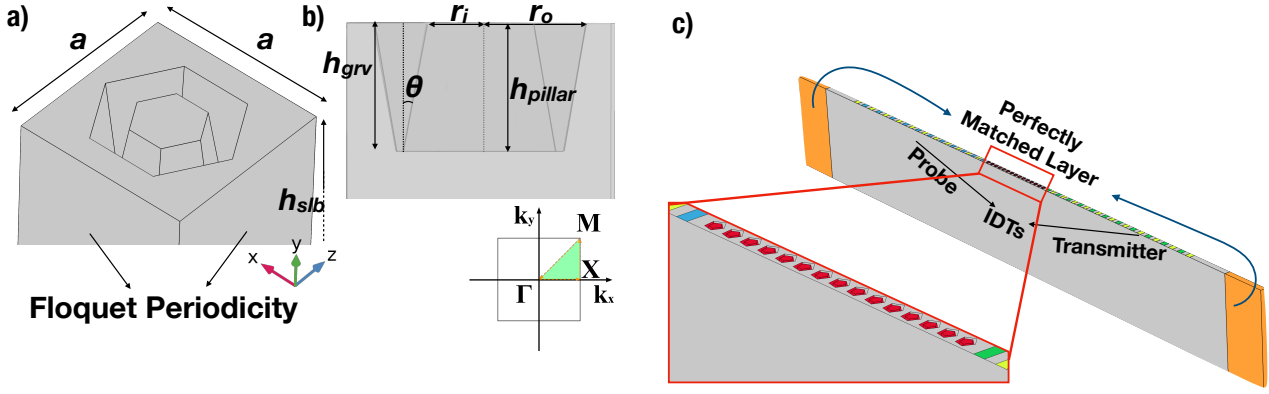


**Figure 1.** a) 3D unit cell used for the simulation of the band profile, b) Cross-sectional view of the unit cell and the wavevector path for the square arrayed PPnCs and c) the 3D FEM model that simulated the SAW attenuation characteristics of the PPnC array.

## 2. METHODS

To examine the band structures of polygonal cavity-type PPnCs and SAW transmission spectra with different numbers of PPnC vertices, FEM simulations were conducted. These simulations utilized *COMSOL Multiphysics* 6.1, which incorporates the piezoelectricity module to couple the elastic wave equation and Maxwell's related equation (Gauss' law). This allows the determination of stresses and electrical potential distributions over piezoelectric materials.

To facilitate a comparison with the research conducted by [Ash et al. \(2017\)](#), a two-dimensional (2D) PPnC in the form of a square lattice was utilized. As depicted in Figure 1a, the square arrayed PPnCs were modelled by fixing the groove depth ( $h_{grv}$ ) to  $6\mu\text{m}$ , groove top radius ( $r_o$ ) to  $5\mu\text{m}$ , pillar bottom radius ( $r_i$ ) to  $3\mu\text{m}$ , and lattice constant ( $a$ ) to  $12\mu\text{m}$ . The pillar height ( $h_{pillar}$ ) was defined as the same as the groove depth. The wall inclination angle ( $\theta$ ) was set to  $10^\circ.2$ , which has been experimentally reported for  $128^\circ$  Y-cut X-propagating (YX- $128^\circ$ ) lithium niobate ( $\text{LiNbO}_3$ ) ([Yavuzcetin et al. 2011](#)). This cut was defined in *COMSOL* using Euler angles  $(\alpha, \beta, \gamma) = (0, 38^\circ, 0)$ . The use of Euler angles is more convenient than the transformation of elasticity and coupling matrices of Z-cut  $\text{LiNbO}_3$ .

To determine the eigenfrequencies of the polygonal cavity-type PPnCs and their corresponding transmission spectra as a function of the number of vertices, FEM simulations were conducted on the irreducible Brillouin zone (BZ) in the first BZ, with the wavevector  $\mathbf{k}$  being swept along the  $\Gamma \rightarrow X \rightarrow M \rightarrow \Gamma$  path for the square array. A 3D schematic of the modelled PPnC unit cell is depicted in Figure 1b, where Bloch-Floquet periodic boundary condition (PBC) was defined for both opposing sides of the unit cell, and the bottom side of the unit cell was defined as a fixed constraint surface. The piezoelectric slab height was set to  $h_{slb} = 200\mu\text{m}$ , and the local resonance bandgap (LRBG) resulting from the resonance vibrations of the core column was found to be below the expected Bragg bandgap [19]. The

LRBG edge frequencies and width can be adjusted by varying the number of vertices of the PPnCs.

To obtain the transmission spectra for each number of vertices, frequency domain FEM simulations were conducted to generate Rayleigh-type SAWs using interdigitated transducers (IDTs) as the standard means of radio frequency (RF) SAW generation. The SAW transmission spectra were simulated for two facing identical IDTs and a PPnC array in between, as shown in Figure 1c. To work in a broad frequency range, chirped IDTs were modelled with a finger width range of  $7.5\mu\text{m}$  to  $12.5\mu\text{m}$ , with a step increase of  $\Delta\omega = 0.5\mu\text{m}$ , and the number of finger pairs in each IDT set to  $N_{IDT} = 11$ . The PPnC array consisted of 15 periodic units equally spaced from the IDT fingers, lying along the [10] direction. The IDT on the left was defined as the source to propagate SAW, while the right-side IDT was used to probe the transmitted signal through the floating potential ( $V_{probe}$ ). SAW transmittance ( $S_{21}$ ) was calculated using the  $S_{21} = 20 \times \log_{10}(V_{probe}/V_{applied})$  where  $V_{applied} = 50\text{ V}$  was the RF amplitude ([Ulug et al. 2022](#)). To minimize unwanted reflections, low-reflecting boundaries (LRB) were placed on the bottom side of the model, and perfectly matched layers (PML) were placed at the edges of the model in the direction of SAW propagation. Periodic boundary conditions (PBC) were used for the sides parallel to the SAW propagation direction, allowing only one row of the PPnC to be modelled while the rest were replicated infinitely through the PBC.

## 3. RESULTS

The band profiles of triangular ( $n=3$ ) and tetradeccagonal cavity-shaped PPnCs, which represent the two external investigated cases in the present work, were plotted as can be seen in Figure 2a and b, respectively. The red dashed lines represent the Rayleigh SAW modes of the bulk slab without perturbation, while the dispersion lines of other leaky SAW modes are omitted. The shaded regions in red and green indicate the excluded



ranges of these leaky modes. The two lowest bands are associated with the bending and expansion modes of the core pillar, and hence, they are flat as stated in Jin et al. (2021). In contrast, the third band consists of the anti-resonant modes of the outer grooves. So all these modes are labelled as A, B and C, respectively and the corresponding displacements were given as inset in Figure 2.

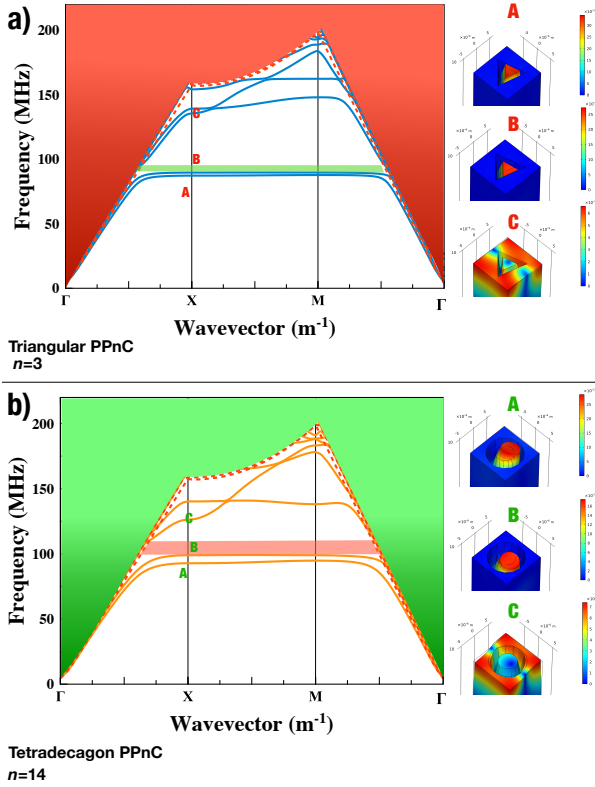


**Figure 2.** Band profile of a) triangular ( $n=3$ ) cavity type and b) tetradecagon ( $n=14$ ) type PPnC and corresponding displacements in the resonance frequencies.

The horizontal hatched highlighted stripes in Figure 2a and b represent the local resonance bandgap region of the PPnC unit cell. As the number of vertices increases, the LRBG broadens and its central frequency  $f_c$  is shifted to higher values.

In order to obtain an explicit knowledge of the effect of the number of vertices in the band profile, a series of band profiles were studied from  $n=3$  to  $n=14$  where the  $n$  is the number of vertices. In Figure 3, band behaviours in the BZ were plotted for each PPnC vertices type. The LRBG-related bands shift to the higher frequencies up to  $n=6$ , while no band profile change was observed afterward.

The BG characteristics as a function of the number of vertices were plotted as in Figure 4a to bring clarity to the geometry dependence of the polygonal cavity-type PPnCs. The corresponding frequencies to the BG edges shift to the higher-frequency regions with the increasing number of vertices and remain almost fixed for the greater edge number than  $n=6$ . This behaviour can be attributed to changes in the moment of inertia

( $\Delta I$ ) with respect to the polygonal cavity shape (Muhammad et al. 2021; Tateno et al. 2021; Guo & Zhang 2022). Figure 4b was plotted to emphasize the coherence of the frequency response and the moment of inertia of the polygonal cavity type PPnCs. The moment of inertia difference, which equals to the moment of inertia of the cavity, represents the same trend as the resonance frequencies. It is also stated from the 1st derivatives of the moment of inertia and mass of the cavity as can be seen in Figure 4c, the governing factor is the extracted mass for both moments of inertia and the resonance frequency.

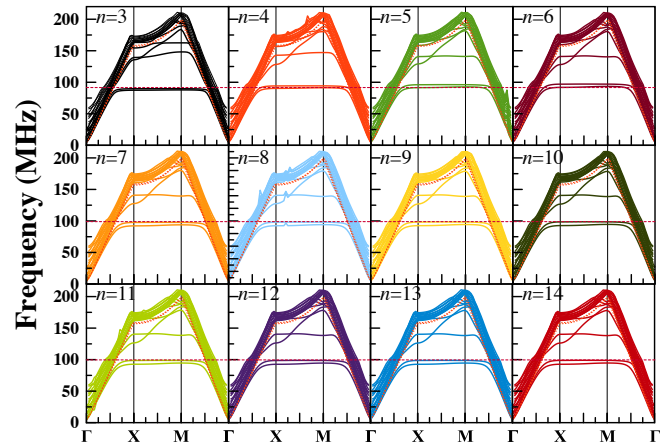


**Figure 3.** The band structures of the square array polygonal cavity-type PPnCs for the different number of vertices.

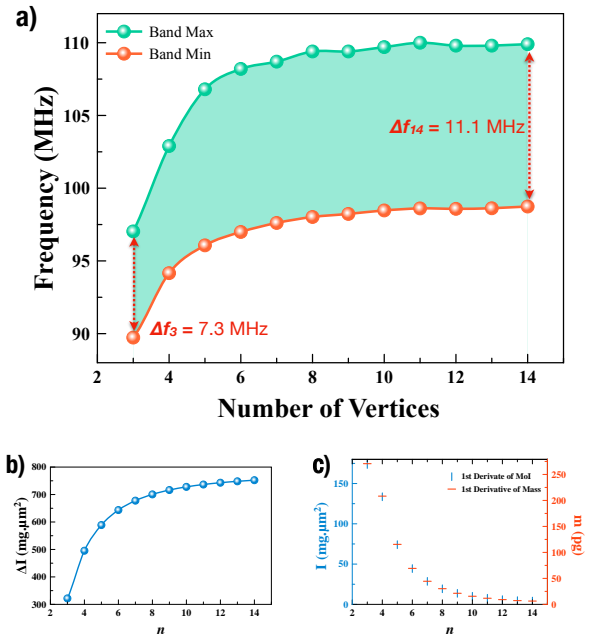


**Figure 4.** a) Changes in the frequencies at the edges of the LRBG with respect to the number of vertices of polygonal cavity-type PPnC, b) the moment of inertia difference ( $\Delta I$ ) of groove and pillar as a function of the number of vertices that equals to the extracted part to create the cavity and c) 1st derivatives of the moment of inertia and mass of the extracted part of the polygonal cavity-type PPnC.

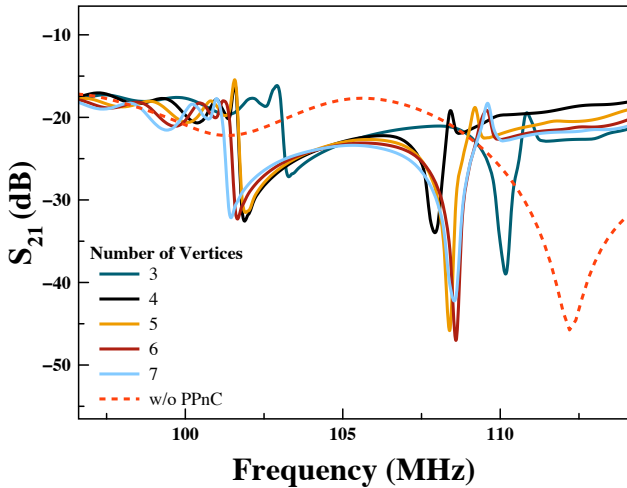


**Figure 5.** Transmission spectra of SAWs are presented for the polygonal cavity-type square PPnC array with varying numbers of vertices oriented along the [10] direction.

To gain a better understanding of the interaction between PPnC and SAW, transmission spectra ( $S_{21}$ ) were obtained. Figure 5 displays the SAW transmission spectra in the range of 95 MHz to 115 MHz for each number of vertices ranging from 3 to 7. The red dashed line in Figure 5 represents the  $S_{21}$  spectrum of the bare chirped IDT pairs without the PPnC between them. Each transmission spectrum shows two distinct peaks, with the major peak at approximately 107 MHz and the minor peak at around 102 MHz. In comparison to the dispersion profiles, both  $S_{21}$  peak intensities increase until the number of vertices is  $n=6$ . Once the number of vertices increases, the peak intensity around 107 MHz decreases, which results in a poorer SAW attenuation performance. Besides, the minor peak intensity remains almost constant for each PPnC geometry. Also, the major peak frequency shifts through the higher frequencies, as stated in the band profile characteristics.

#### 4. CONCLUSION

To summarize, the simulation results of band structures and SAW transmission spectra for polygonal cavity-type PPnCs are presented as a function of the number of vertices of the PPnC. The LRBG edge frequencies increase, and the width of LRBG increases as the number of vertices of PPnC increases. The attenuation profile tends to increase with the increasing number of vertices of PPnC, and also, the peak frequency shifts through to the higher frequencies up to  $n=6$ . All these characterised properties of the polygonal cavity-type PPnCs were reasoned by the changing extracted mass amount to create different polygonal-shaped cavities, and that makes the investigated PPnCs suitable for sensing applications through the mass loading effect while PPnCs exhibit overt characteristic responses to the sub-nano gram mass differences.

**Peer Review:** Externally peer-reviewed.

**Author Contribution:** Conception/Design of study - F.K.; Data Acquisition - F.K., N.S.G.; Data Analysis/Interpretation - F.K., N.S.G., A.E., A.Ç.; Drafting Manuscript - F.K., N.S.G., A.E., A.Ç.; Critical Revision of Manuscript - F.K., N.S.G., A.E., A.Ç.; Final Approval and Accountability - F.K., A.E., A.Ç.; Supervision - A.E., A.Ç.

**Conflict of Interest:** Authors declared no conflict of interest.

**Financial Disclosure:** Authors declared no financial support.

#### ACKNOWLEDGEMENTS

This work is funded by The Scientific and Technological Research Council of Turkey (TÜBİTAK) (Project No: 120F337).

#### LIST OF AUTHOR ORCIDS

F. Kuruoğlu <https://orcid.org/0000-0002-5314-4441>  
 N. S. Genç <https://orcid.org/0009-0001-5301-177X>  
 A. Erol <https://orcid.org/0000-0003-4196-1791>  
 A. Çiçek <https://orcid.org/0000-0002-7686-0045>

#### REFERENCES

- Achaoui Y., Khelif A., Benchabane S., Robert L., Laude V., 2011, *Physical Review B*, 83, 104201  
 Achaoui Y., Laude V., Benchabane S., Khelif A., 2013, *Journal of Applied Physics*, 114, 104503  
 Agostini M., Greco G., Cecchini M., 2019, *IEEE Access*, 7, 70901  
 Ash B. J., Worsfold S. R., Vukusic P., Nash G. R., 2017, *Nature Communications*, 8, 174  
 Bourquin Y., Wilson R., Zhang Y., Reboud J., Cooper J. M., 2011, *Advanced Materials*, 23, 1458  
 Cao D., Hu W., Gao Y., Guo X., 2019, *Smart Materials and Structures*, 28, 085014  
 Collins D. J., Devendran C., Ma Z., Ng J. W., Neild A., Ai Y., 2016, *Science Advances*, 2, e1600089  
 Gharibi H., Mehaney A., 2021, *Physica E: Low-dimensional Systems and Nanostructures*, 126, 114429  
 Gharibi H., Khaligh A., Bahrami A., Ghavifekr H. B., 2019, *Journal of Molecular Liquids*, 296, 111878  
 Guo J. C., Zhang Z., 2022, *Applied Physics A*, 128, 126  
 Guo L., Zhao S., Guo Y., Yang J., Kitipornchai S., 2023, *International Journal of Mechanical Sciences*, 240, 107956  
 Hekiem N. L. L., Ralib A. A. M., Hattar M. A. b. M., Ahmad F., Nordin A. N., Rahim R. A., Za'bah N. F., 2021, *Sensors and Actuators A: Physical*, 329, 112792  
 Jin Y., Pennec Y., Bonello B., Honarvar H., Dobrzynski L., Djafari-Rouhani B., Hussein M. I., 2021, *Reports on Progress in Physics*, 84, 086502  
 Kidakova A., Boroznjak R., Reut J., Öpik A., Saarma M., Syritski V., 2020, *Sensors and Actuators B: Chemical*, 308, 127708  
 Korozlu N., Biçer A., Sayarcan D., Kaya O. A., Cicek A., 2022, *Ultrasonics*, 124, 106777

- Kumar A., Prajesh R., 2022, *Sensors and Actuators A: Physical*, p. 113498
- Kuruoğlu F., 2022, *Cumhuriyet Science Journal*, 43, 346
- Kushwaha M. S., Halevi P., Dobrzynski L., Djafari-Rouhani B., 1993, *Physical Review Letters*, 71, 2022
- Kushwaha M. S., Halevi P., Martínez G., Dobrzynski L., Djafari-Rouhani B., 1994, *Physical Review B*, 49, 2313
- Li X., Ning S., Liu Z., Yan Z., Luo C., Zhuang Z., 2020, *Computer Methods in Applied Mechanics and Engineering*, 361, 112737
- Mead D., 1996, *Journal of Sound and Vibration*, 190, 495
- Muhammad Lim C., Leung A. Y. T., 2021, *Acoustics*, 3, 25
- Oh J. H., Lee I. K., Ma P. S., Kim Y. Y., 2011, *Applied Physics Letters*, 99, 083505
- Pouya C., Nash G. R., 2021, *Communications Materials*, 2, 55
- Qian J., Ren J., Liu Y., Lam R. H. W., Lee J. E.-Y., 2020, *Analyst*, 145, 7752
- Schmidt M.-P., Oseev A., Lucklum R., Zubtsov M., Hirsch S., 2016, *Microsystem Technologies*, 22, 1593
- Sigalas M., Economou E., 1993, *Solid State Communications*, 86, 141
- Su R., et al., 2021a, *IEEE Transactions on Device and Materials Reliability*, 21, 365
- Su R., et al., 2021b, *IEEE Electron Device Letters*, 42, 438
- Tateno S., Kurimune Y., Matsuo M., Yamanoi K., Nozaki Y., 2021, *Physical Review B*, 104, L020404
- Topaltzikis D., et al., 2021, *Applied Physics Letters*, 118, 133501
- Ulug B., Kuruoğlu F., Yalçın Y., Erol A., Sarcan F., Şahin A., Cicek A., 2022, *Journal of Physics D: Applied Physics*, 55, 225303
- Vasseur J. O., Hladky-Hennion A.-C., Djafari-Rouhani B., Duval F., Dubus B., Pennec Y., Deymier P. A., 2007, *Journal of Applied Physics*, 101, 114904
- Wang Y., Wang Y., Liu W., Chen D., Wu C., Xie J., 2019, *Sensors and Actuators A: Physical*, 288, 67
- Xie Y., Mao Z., Bachman H., Li P., Zhang P., Ren L., Wu M., Huang T. J., 2020, *Journal of biomechanical engineering*, 142
- Yavuzcetin O., Ozturk B., Xiao D., Sridhar S., 2011, *Optical Materials Express*, 1, 1262
- Zhang X.-F., Zhang Z.-W., He Y.-L., Liu Y.-X., Li S., Fang J.-Y., Zhang X.-A., Peng G., 2015, *Frontiers of Physics*, 11
- Zhang Z.-D., Liu F.-K., Yu S.-Y., Lu M.-H., Chen Y.-F., 2020, *Applied Physics Express*, 13, 044002

# Laser Spectroscopic Investigation of the Hyperfine Structure of Atomic Manganese in the Mid-infrared Wavelength Range

S. Kröger<sup>1\*</sup> , L. Windholz<sup>2</sup> , and Gö. Başar<sup>3</sup> 

<sup>1</sup>Hochschule für Technik und Wirtschaft Berlin, Fachbereich 1, Wilhelminenhofstr. 75A, D-12459 Berlin, Germany

<sup>2</sup>Institut für Experimentalphysik, Technische Universität Graz, Petersgasse 16, Graz A-8010, Austria

<sup>3</sup>Istanbul University, Faculty of Science, Department of Physics, TR-34134 Vezneciler, Istanbul, Turkiye

## ABSTRACT

The hyperfine structure of atomic manganese was studied with laser induced fluorescence spectroscopy and optogalvanic spectroscopy using a commercial hollow cathode discharge lamp and a fully automated single mode mid-infrared tunable laser diode system in the wavelength range from 1530 nm to 1610 nm. Five spectral lines has been analysed. Magnetic dipole hyperfine structure constants  $A$  for seven levels were determined by fitting the hyperfine structure using Voigt profile functions. For two levels, the  $A$  constants were determined experimentally for the first time. For the other levels, the previously published hyperfine structure constants  $A$  could be confirmed and the accuracy of the values could be improved. When comparing our two new experimental  $A$ -constants with calculated  $A$ -constants from the literature, which originate from a semi-empirical analysis of the odd parity levels in Mn, large deviations were found. Until now, experimental values were missing for a more precise calculation. Our new values offer the possibility for a future optimisation of the calculation.

**Keywords:** laser spectroscopy – hyperfine structure – manganese

## 1. INTRODUCTION

Lasers in the visible and near infrared spectral range up to 1000 nm have been used very successfully for many decades for the investigation of atomic hyperfine structure (hfs) and isotopic shifts. For some time now, suitable laser light sources have also been available in the infrared spectral range above 1000 nm, but so far they have not been used for such applications. Presented here for the first time is the use of a fully automated diode laser system in the mid-infrared to measure the hfs of atomic transitions of manganese. The device used offered a fast and straightforward possibility to study atomic spectra at high resolution without using additional devices for characterizing the laser radiation, such as a wavemeter or a reference marker Fabry-Perot-Interferometer (see Section 2).

Manganese (Mn) with the atomic number 25 is one of the 3d elements and belongs to the elements with only one stable isotope. This isotope, <sup>55</sup>Mn, has a nuclear spin of  $I = 5/2$  and a nuclear magnetic dipole moment of  $\mu = 3,468716(2) \mu_N$  (Lederer & Shirley 1978), leading to a broad hfs splitting in Mn spectra. This splitting is also clearly seen in Doppler broadened spectra. The electric quadrupole moment with  $Q = 0.33(1)$  barns (Lederer & Shirley 1978) causes only a small de-

viation of the magnetic dipole hfs, which is not well detectable at the resolution of our experiments.

In the last decades several investigations of the fine structure and hfs of atomic Mn have been conducted, see Lefèbvre et al. (2003); Başar et al. (2003); Blackwell-Whitehead et al. (2005); Acar et al. (2005); Kloze et al. (2013); Głowacki et al. (2020a,b); Elantkowska et al. (2022); Głowacki et al. (2022) and references therein. Although much research has been done, there are still many gaps in the hfs data for Mn I and reliable laboratory data are an important prerequisite for the study of astrophysical spectra, for example for the analysis of stellar abundances and for the determination of physical parameters in stellar atmospheres.

Three of the five infrared Mn lines presented here have already been studied by Meléndez (1999) who fitted the solar spectrum. The resolution in our spectra is significantly better than in the solar spectrum. Meléndez has explicitly pointed out in his paper that laboratory measurements are necessary to improve the accuracy of HFS splitting.

Corresponding Author: S. Kröger E-mail: sophie.kroeger@htw-berlin.de

Submitted: 30.04.2023 • Revision Requested: 15.05.2023 • Last Revision Received: 19.05.2023 • Accepted: 22.05.2023 • Published Online: 30.05.2023



This article is licensed under a Creative Commons Attribution-NonCommercial 4.0 International License (CC BY-NC 4.0)

## 2. EXPERIMENTAL

Laser induced fluorescence spectroscopy (LIF) and optical-galvanic spectroscopy (OGS) have been applied for the measurements of the hfs of Mn spectra. The experimental set up allowed to measure with both methods simultaneously.

The free Mn atoms were produced in a commercial hollow cathode lamp (Hamamatsu Photonics) with Ne as buffer gas. The discharge ran with a current of about 20 mA.

A single mode mid-infrared tunable laser diode system (DLC CTL 1550 from TOPTICA Photonics) with an optical power of about 40 mW in the wavelengths in the range from 1510 nm to 1630 nm was used to excite the Mn atoms. The laser was controlled fully automatically via the laser DLC controller. The wavelength could be mode-hop free tuned over the entire wavelength range. The scanning speed and step width could be adjusted. The laser controller has four integrated AD converters, two of which were used to measure for the LIF and OGS signals, respectively. Measurements are taken via the supplied DLC pro PC-GUI control software, which allows easy control of the laser and simultaneous measurement data acquisition.

The laser beam was amplitude-modulated by a mechanical chopper with a frequency of slightly below 3 kHz. The Lock-in technique was used to filter out the OGS and LIF signals from the corresponding signals. For OGS, the laser-induced change of the discharge voltage measured across a ballast resistor was sent to the lock-in amplifier. For LIF, the light from the plasma was coupled to a monochromator (McPherson with a grating with 1200 lines/mm) and detected with a photomultiplier (Hamamatsu R928). The signal from the photomultiplier was sent to a second lock-in amplifier in order to detect the change in intensity of the fluorescence caused by the laser light. The fluorescence light from the laser-induced transition was detected at a selected wavelength of the monochromator with a wavelength precision of 0.1 nm.

The laser diode system DLC CTL is able to scan the wavelength very quickly. Since the intensity of the investigated Mn lines was relatively weak compared to the neighboring noble gas (Ne) lines, a high time constant of 300 ms or 1 s had to be set at the lock-in in order to minimise noise and make the lines stand out clearly from the noise. The scanning speed had to be adapted to this time constant and therefore a slow scanning speed was chosen. Scan times of 0.02 nm per minute data and a step size of 0.0005 nm have been set on the laser controller.

The PC control software provides a cvs data file with the wavelength and the signal(s) of the AD converter(s). The OGS signal was always measured with the first AD converter. For three lines, the LIF signal was recorded additionally with the second AD converter. For two lines, no fluorescence line with a sufficiently strong LIF signal was available. These lines were only measured with OGS.

The absolute wavelengths given by the DLC CTL control are not calibrated. The investigated spectral lines could nev-

ertheless be clearly assigned. The position of the lines was determined relative to the neighboring noble gas lines and the wavelengths were additionally checked with an external wavemeter (HighFinesse WS7-60). Since the determination of the absolute wavelength is not the focus of interest in this present work, no further effort was made at this point. In the following, the wavelength calculated from the level energies using the Rydberg-Ritz combination principle is used to mark the lines.

The temporal linearity of the laser scan was checked and confirmed with the external HighFinesse wavemeter, which ran parallel to the measurement but was recorded separately.

Despite the linearity of the wavelength change, the data increments of the measurement data are not exactly uniform. For the subsequent evaluation of the experimental data (see Section 3), equidistant data on a frequency axis are required. Therefore, the data of the experimental wavelengths in the measured spectra were converted into frequencies. Subsequently, the spectra consisting of frequency and intensity data pairs were transferred by linear interpolation to equidistant interpolation points with a step size of 40 or 50 MHz using a Python script. Each line was measured and analysed at least five times.

## 3. HYPERFINE STRUCTURE ANALYSIS

In the wavelength range of the laser system (from 1510 nm to 1630 nm), five Mn lines could be unambiguously classified. The classification of the lines was done with program *Elements* (Windholz & Guthöhrlein 2003; Windholz 2016), which used a list of levels of atomic and singly ionic Mn from ? to search for transitions matching the wavelengths. Three of the lines are found in the literature and had already been classified by Meléndez (1999).

The lines are compiled in Table 1, sorted by lower level, and shown in Figures 1 and 2. The wavenumbers  $\sigma$  are the centre-of-gravity of the hfs calculated using the Rydberg-Ritz combination principle from the fine structure level energies. The wavelengths in air  $\lambda_{\text{air}}$  are calculated from the wavenumbers. The level energies values and  $J$  quantum numbers of the lower and the upper levels are given according to the database from Kurucz<sup>1</sup>. In the seventh column, the experimental method used is listed. In the final column, a comment concerning the hfs analysis is given.

For all lines, the lower level has even parity. Three and two lines, respectively, each have the same lower level. The three lines connected to the lower level  $39\,431.368\text{ cm}^{-1}$  (see Figure 1) were measured with OGS and LIF. For the LIF measurements in all three cases the same fluorescence line was used,  $\lambda_{\text{air, f}} = 482.35\text{ nm}$ , starting from the lower level of the laser transition. The signal-to-noise ratio was slightly better using LIF than OGS. The measurement results of both spectroscopy

<sup>1</sup> <http://kurucz.harvard.edu/atoms/>

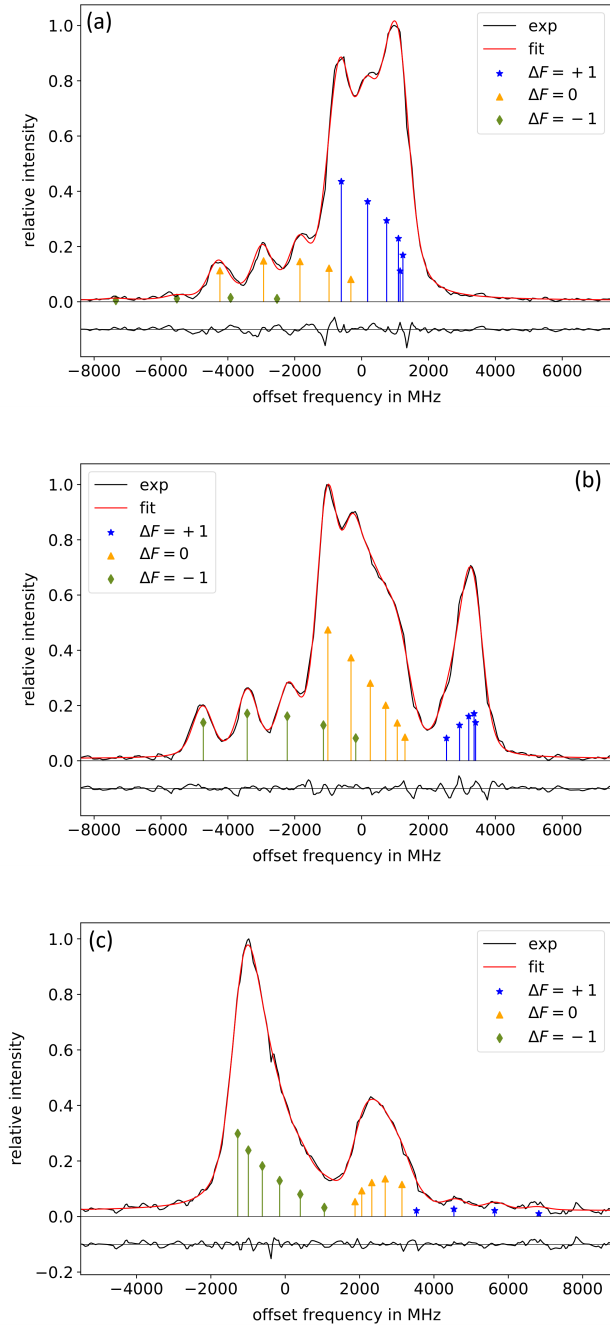


**Figure 1.** Hfs spectra of the three lines connected to the lower level  $39\,431.368\text{ cm}^{-1}$ ,  $J = 7/2$  recorded with LIF, together with the best fit curves. The hfs components are marked by the difference  $\Delta F$  of the total angular momenta of the upper and lower hfs levels. In the lower part of each figure, the difference between experimental and best-fit curves is given. a) transition to upper level  $46\,026.238\text{ cm}^{-1}$ ,  $J = 9/2$ , b) transition to upper level  $46\,000.874\text{ cm}^{-1}$ ,  $J = 7/2$ , c) transition to upper level  $45\,981.621\text{ cm}^{-1}$ ,  $J = 5/2$ .

methods were used for the hfs analysis. As mentioned above, for the two lines, connected to the lower level  $49\,415.397\text{ cm}^{-1}$  (see Figure 2), no fluorescence line was found and therefore only OGS measurements are available for the hfs analysis.

To analyse hfs, the linearised experimental spectra were fitted

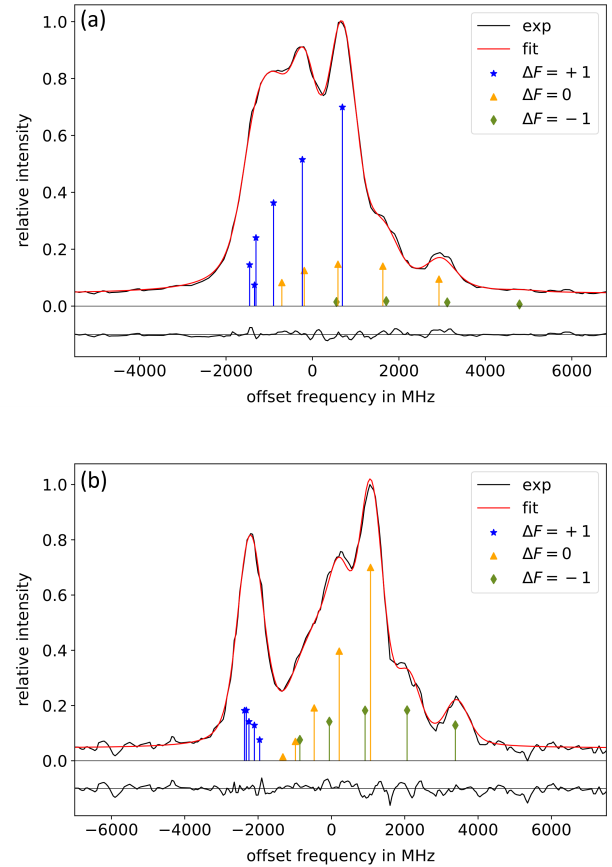


**Figure 2.** Hfs spectra of the two lines connected to the lower level  $49\,415.397\text{ cm}^{-1}$ ,  $J = 5/2$  recorded with OGS, together with the best fit curves. The hfs components are marked by the difference  $\Delta F$  of the total angular momenta of the upper and lower hfs levels. In the lower part of each figure, the difference (diff.) between experimental and best-fit curves is given. a) transition to upper level  $56\,012.635\text{ cm}^{-1}$ ,  $J = 7/2$ , b) transition to upper level  $56\,008.209\text{ cm}^{-1}$ ,  $J = 5/2$ .

with the computer program, FITTER (Zeiser et al. 2022). The fitting program uses a list of parameters, which can be set as free parameters, coupled with other parameters or can be set to a specific value if required. The list of parameters comprises the centre of gravity of the total hfs, the hfs constants  $A$  and  $B$  of the upper and the lower levels, two parameters to take into account the height and slope of the background, as well as the relative intensity and two profile parameters for each individual hfs component. We chose a Voigt profile as the line profile function, which requires two full widths at half maximum (FWHM) profile parameters per individual hfs component, each one to describe the Gaussian and the Lorentzian parts of the Voigt profile.

As can be seen in Figure 1 and 2, with the resolution achieved in our experiment all lines are partly unresolved. Therefore the number of free parameters in the fit had to be reduced considerably. For this purpose

- the electric quadrupole hfs constants  $B$  of both levels were set to be zero,
- for three lines the magnetic dipole hfs constants  $A$  of the lower level was fixed (see Table 1),
- the Gaussian part of the Voigt profile is set to be equal for all hfs components,
- the Lorentzian part of the Voigt profile is set to be equal for all strong hfs components with  $\Delta F = \Delta J$  and for all weak hfs components with  $\Delta F \neq \Delta J$ , and
- the intensities of the individual hfs components are coupled to each other.

The explanation for these steps is given in the following paragraphs.

The hfs constants  $B$  were set to zero because the influence of the electric quadrupole interaction is very small for Mn (as mentioned in the introduction) and it was not possible to determine reliable values for the  $B$  constants with our Doppler-limited spectra.

To determine the  $A$  value of the lower levels, in each set of lines connecting the same lower level the best resolved line was selected. This line was fitted with magnetic dipole hfs constants  $A$  of the lower level and the upper levels as freely floating parameters. The resulting  $A$  values were preset and fixed when fitting the hfs of the other lines. The corresponding information is given in the last column of Table 1.

All lines are influenced by saturation effects, leading to a reduction in intensity as well as a broadening of the strong hfs components. As a consequence, the intensity ratios of the individual hfs components do not agree with the theoretical intensity ratios for electrical dipole transitions and the Lorentzian part of the full width at half maximum (FWHM) differs for different hfs components. For unsaturated spectra, all hfs components could have been fitted with the same Voigt FWHM. For saturated spectra, the Gaussian parts of the Voigt profile remains only slightly affected by saturation, whereas the width of the Lorentzian contribution varies. To account the saturation broadening of the strong hfs components in our spectra, two parameters for the Lorentzian part were fitted as freely floating parameter, one for all strong hfs components with  $\Delta F = \Delta J$  and one for all weak hfs components with  $\Delta F \neq \Delta J$ .

To account for the saturation of the intensities of all hfs components, a single parameter was applied. Based on this parameter, theoretical values were calculated for the saturated intensities of the individual hfs components. These values were then used to couple to the intensity ratios during the fit. This method was presented in previous papers by one of the authors (LW) (Sobolewski 2019, 2020; Faisal 2020). The saturation parameter is not implemented in the fit program, therefore the parameter was changed step by step by hand until the optimal fit with minimised sum of squares of the residuals was found.

The saturation effects were much stronger for the lines connected to the lower level  $39\,431.368\text{ cm}^{-1}$  than for the lines

connected to the lower level  $49\,415.397\text{ cm}^{-1}$ . The saturation-induced intensity increase of the weak components relative to the strongest component was between 2.5 and 3.0 for the lines connected to the lower level  $39\,431.368\text{ cm}^{-1}$ , while it was only 1.4 for the other lines.

The FWHM of the Voigt profiles was for all lines in the order of magnitude of 700 to 800 MHz and the FWHM of the Gaussian parts in the order of magnitude of 530 MHz to 600 MHz. Depending on the different lines the FWHM of the Lorentzian parts varied between 200 MHz to 440 MHz.

The resulting magnetic dipole hfs constants  $A_{\text{exp}}$  are listed in Table 2 together with the values from the literature, if available. The term designation according to (Elantkowska et al. 2022; Głowacki et al. 2022) is given in the fourth column. The spectral lines used for the determination of the  $A$  constants are indicated in the fifth column.

The reported constants  $A_{\text{exp}}$  are the mean values of the fit results of all measurements of the respective line. The uncertainties, indicated within brackets, consider both the standard deviation associated with the mean value and the error bar of the fixed  $A$  value, assuming the  $A$  constant of the lower level had been fixed during the fit.

For five levels, our  $A$  constants are in good agreement with the values from the literature (Brodzinski et al. 1987; Blackwell-Whitehead et al. 2005). The accuracy of the  $A$  constants could be improved.

For comparison, in the last two columns from Table 2 calculated values for the  $A$  constants, resulting from semi-empirical analysis of the odd and even parity level system in Mn (Elantkowska et al. 2022; Głowacki et al. 2022) are given. The calculated values from the literature for the two even parity levels show a very good consistency with the experimental  $A$  constants, much better than for the odd parity levels. For the levels with odd parity, a deviation in the order of 60 to 100 MHz can be seen for the levels whose  $A$  constants were already known previously and were taken into account in the semi-empirical calculation. For the two levels with previously unknown  $A$  constants, the deviation of our experimental values  $A_{\text{exp}}$  from the predicted constants  $A_{\text{calc}}$  from the semi-empirical fit lies at 280 MHz and 380 MHz and is much larger. This emphasises the importance of our experimental results. The enlargement of the experimental database will lead to an improvement in the results of semi-empirical calculations if the new values will be taken into account.

#### 4. CONCLUSION AND OUTLOOK

For the first time, a laser system in the mid-infrared spectral range was used to investigate the hfs in atomic spectra. Due to the implementation of a fully automated controller, the measurements could be carried out quickly and easily. The hfs of five spectral lines of atomic Mn has been investigated. Magnetic dipole hfs constants  $A$  for seven levels were obtained, two

**Table 1.** Lines of atomic manganese measured with LIF or OGS.

Line		Even level		Odd level		Method	Comment
$\lambda_{\text{air}}$ (nm)	$\tilde{\nu}$ ( $\text{cm}^{-1}$ )	$E_e$ ( $\text{cm}^{-1}$ )	$J_e$	$E_o$ ( $\text{cm}^{-1}$ )	$J_o$		
1 515.916	6 594.870	39 431.368	7/2	46 026.238	9/2	LIF	$A_{\text{lower}}$ fixed during the fit
1 521.769	6 569.506	39 431.368	7/2	46 000.874	7/2	LIF	Both $A$ constants fitted independently
1 526.242	6 550.253	39 431.368	7/2	45 981.621	5/2	LIF	$A_{\text{lower}}$ fixed during the fit
1 515.372	6 597.238	49 415.397	5/2	56 012.635	7/2	OGS	$A_{\text{lower}}$ fixed during the fit
1 516.389	6 592.812	49 415.397	5/2	56 008.209	5/2	OGS	Both $A$ constants fitted independently

**Table 2.** Experimental magnetic dipole hyperfine structure constants  $A$  (in MHz) for levels of atomic manganese (sorted by parity  $p$ ).

$E$ ( $\text{cm}^{-1}$ )	$J$	$p$	Config., term [3,4]	$\lambda$ (nm)	$A_{\text{exp}}$	$A_{\text{ef}}$	Reference	$A_{\text{calc}}$	Reference
39 431.368	7/2	e	$3d^5(^6S)4s5s\ ^8S$	1521.769	736.2 (15)	737 (3)	[1]	738	[3]
49 415.397	5/2	e	$3d^5(^6S)4s5s\ ^6S$	1516.389	-632 (4)	-642 (9)	[1]	-682	[3]
45 981.621	5/2	o	$3d^5(^6S)4s5p\ ^8P$	1526.242*	826.3 (21)	824 (3)	[2]	719	[4]
46 000.874	7/2	o	$3d^5(^6S)4s5p\ ^8P$	1521.769	620.0 (11)	621 (3)	[2]	555	[4]
46 026.238	9/2	o	$3d^5(^6S)4s5p\ ^8P$	1515.916*	518.6 (19)	519 (3)	[2]	467	[4]
56 008.209	5/2	o	$3d^5(^6S)4s8p\ ^6P$	1516.389	-470 (6)			-82	[4]
56 012.635	7/2	o	$3d^5(^6S)4s5p\ ^6P$	1515.372*	-372 (7)			-92	[4]

(\*): hfs constants  $A$  of the lower level were fixed during the fit.

[1]: Brodzinski et al. (1987), [2]: Blackwell-Whitehead et al. (2005), [3]: Elantkowska et al. (2022), [4]: Głowacki et al. (2022)

**Note:** values from Brodzinski et al. (1987) and Blackwell-Whitehead et al. (2005) have been converted to MHz from  $\text{mK} = 10^{-3} \text{cm}^{-1}$ .

of these for the first time. Our newly obtained  $A$  constant values exhibit concurrence with the values characterized by previously established literature and are within the designated error limits, wherein our values have less errors. The two new  $A$  constants point out a large discrepancy between the experimental values and predicted literature values resulting from a semi-empirical analysis (Głowacki et al. 2022). We recommend that the calculation should be repeated with our new values.

In the Mn spectrum between 1510 nm to 1630 nm, there were a few more Mn lines that could not be classified. This means that at least one of the two levels involved must be unknown for each line. We will try to solve the problem of these unclassified lines as well. For this, however, further experiments must be carried out.

**Peer Review:** Externally peer-reviewed.

**Author Contribution:** Conception/Design of study - S.K., Gö. B.; Data Acquisition - S.K.; Data Analysis/Interpretation - L.W., Gö. B., S.K.; Drafting Manuscript - S.K.; Critical Revision of Manuscript - Gö.B., L.W.; Final Approval and Accountability - S.K., Gö.B.

**Conflict of Interest:** Authors declared no conflict of interest.

**Financial Disclosure:** Authors declared no financial support.

## ACKNOWLEDGEMENTS

Sophie Kröger acknowledges TOPTICA Photonics for loaning the laser system DLC CTL 1550 for the period of the measurements.

## LIST OF AUTHOR ORCIDS

S. Kröger <https://orcid.org/0000-0003-4991-9176>  
L. Windholz <https://orcid.org/0000-0001-6078-6154>  
Gö. Başar <https://orcid.org/0000-0002-2428-8163>









## REFERENCES

- Acar G., Başar Gü., Başar Gö., Öztürk I. K., Kröger S., 2005, *PhysS*, 71, 245  
Başar Gü., Başar Gö., Acar G., Öztürk I. K., Kröger S., 2003, *PhysS*, 67, 476  
Blackwell-Whitehead R., Pickering J., Pearse O., 2005, *ApJS*, 157, 402  
Brodzinski T., Kronfeldt H.D., Kropp J.R., Winkler R., 1987, *ZPhyD*, 7, 161  
Elantkowska M., Ruczkowski J., Głowacki P., Stefańska D., 2022, *JQSRT*, 292, 108347  
Faisal M., Windholz L., Kröger S., 2020, *JQSRT*, 245, 106873



- Głowacki P., Stefańska D., Ruczkowski J., Elantkowska M., 2020a, [JQSRT](#), 253, 107138
- Głowacki P., Stefańska D., Elantkowska M., Ruczkowski J., 2020b, [JQSRT](#), 249, 107013
- Głowacki P., Stefańska D., Ruczkowski J., Elantkowska M., Chomski M., Furmann B., 2022, [JQSRT](#), 287, 108245
- Klose A., Minamisono K., Mantica P.F., 2013, [PhRvA](#), 88, 042701
- Lederer C.M., Shirley V.S., 1978, [Tables of Isotopes](#), 7th ed.; Wiley: New York, US
- Lefèbvre P.-H., Garnir H.-P., Biémont E., 2003, [A&A](#), 404, 1153
- Meléndez J., 1999, [MNRAS](#), 307, 197
- Sobolewski Ł.M., Windholz L., Kwela J., Drozdowski R., 2019, [JQSRT](#), 237, 106639
- Sobolewski Ł.M., Windholz L., Kwela J., 2020, [JQSRT](#), 242, 106769
- Windholz, L., Guthöhrlein G.H., 2003, [PhST](#), 105, 55
- Windholz, L., 2016, [PhyS](#), 91, 114003
- Zeiser A., Kröger S., Pooyan-Weis L., Windholz L., Guthöhrlein G., 2022, [JQSRT](#), 290, 108294

# Selective Antimicrobial Properties of W-Ge Nanocomposite Thin Films

S. Atasoy<sup>1\*</sup> , Y. Kurul<sup>1</sup> , S. Aktas<sup>1</sup> , F. Sarcan<sup>2</sup> , M. S. Kurt<sup>3</sup> , A. Ayna<sup>4</sup> , E. Darendelioğlu<sup>4</sup> ,  
and A. Erol<sup>2</sup> 

<sup>1</sup>Giresun University, Faculty of Engineering, Department of Mechanical Engineering, 28200, Giresun, Türkiye

<sup>2</sup>Istanbul University, Faculty of Science, Department of Physics, Vezneciler, 34134, Istanbul, Türkiye

<sup>3</sup>Erzurum Technical University, Science Faculty, Department of Fundamental Science, 25050, Erzurum, Türkiye

<sup>4</sup>Bingöl University, Faculty of Science and Literature, Department of Chemistry, 12000, Bingöl, Türkiye

## ABSTRACT

The antimicrobial properties of W-Ge nanocomposite thin films as a function of Ge concentration were investigated within the scope of this study. The films were deposited on an AZ61Mg substrate using a magnetron sputter source with a co-deposition technique. Structural analyses showed that all coatings had a composite crystal structure. Additionally, the morphological investigation indicated that films had goosefoot-type structures at low Ge concentrations (5% and 10%), while Ge-rich films (40% and 60%) had cauliflower-type structures. The 20% Ge concentration coating had both structures. Regarding the surface morphology, the root mean square roughness of the surface reached its maximum value at a Ge concentration of 60% while the surface roughness and wettability of all the films showed an opposite trend. The antimicrobial activity of the W-Ge nanocomposite films against gram-negative (*Salmonella typhimurium* NRRLE 4413, *Escherichia coli* ATCC 25922) and gram-positive (*Staphylococcus aureus* 6538 P, *Bacillus subtilis* IM 622) bacteria was investigated via disc diffusion antibiotic sensitivity assay. Based on the antibacterial activity test, it was concluded that although all the films had antimicrobial efficiency against gram-negative and gram-positive bacteria, they were more effective against gram-positive bacteria. Moreover, with the increased surface roughness of the films, the number of grain boundaries, which cause an increase in the intensity of the oxide phases of the metals, increases, resulting in better antibacterial activity.

**Keywords:** nanocomposite thin film – tungsten – germanium – antibacterial efficiency – surface roughness

## 1. INTRODUCTION

Metallic composite thin films find extensive application across various fields such as environmental sensing, gas sensing, and water purification due to their enhanced performance, extended functionality as well as low cost, and given performance not attainable with bulk materials (Martin 2009; Zboun et al. 2020). Additionally, there are several studies focusing on the antimicrobial efficiency of metallic composite thin films. For instance, Menazea & Awwad (2020) reported on the antimicrobial efficiency of TiO<sub>2</sub> doped ZnO thin film, which was produced by pulsed laser ablation in liquid. Chuang et al. (2017) studied the effects of Ag<sub>2</sub>O on the antibacterial efficiency of ZnO/Ag<sub>2</sub>O composite thin film produced via magnetron sputtering method. Furthermore, Jena et al. (2020) presented a work that focused on the antibacterial properties of ternary composite coatings (graphene oxide - chitosan-silver) produced by the electrophoretic deposition technique. Arslan et al. (2022) reported on the antibacterial properties of Ge-DLC (diamond-like carbon) coatings produced by co-deposition technique via

magnetron sputtering method. As pointed out in various studies, the quality of the metallic composite materials, which depends on the growing method, has a significant effect on the sensing performance of the devices and/or functionalization of the material against bacteria. The most preferred thin film deposition techniques include physical and chemical vapour deposition, solution processes, and fusion processes (Voevodin et al. 1999; Somogyvári et al. 2012; Park et al. 2006; Helmersson et al. 2006; Roy et al. 2015; Sarcan 2020). Among these, the magnetron sputtering method allows the co-deposition of two metals by controlling the deposition rate under high-vacuum conditions, thereby avoiding any contamination.

The antimicrobial properties of Ge and its compounds were proved in a study on human pathogenic bacteria (Sellappa & Jeyaraman 2011). The studies on *Pseudomonas aeruginosa* planktonic and *Staphylococcus aureus* in suspension revealed that elemental Ge has antimicrobial activities (Kurt et al. 2021; Khalid et al. 2014). Ge naturally exists in very low concentrations in dairy foods. This metal, which is taken at a low amount

Corresponding Author: S. Atasoy E-mail: selcuk.atasoy@giresun.edu.tr

Submitted: 28.04.2023 • Revision Requested: 22.05.2023 • Last Revision Received: 29.05.2023 • Accepted: 05.06.2023 • Published Online: 12.06.2023



This article is licensed under a Creative Commons Attribution-NonCommercial 4.0 International License (CC BY-NC 4.0)

(0.4 - 3.4 mg) by the human body on a daily basis, contributes to controlling important biological functions such as maintaining sodium, potassium, glucose, and pH levels in balance, as well as lowering blood pressure (Okada et al. 1989; Nagata et al. 1985; Lück et al. 1999; Kaplan et al. 2004; Bian et al. 2017). A long period (18 months) of GeO<sub>2</sub> intake has been reported to result in acute renal failure in the human body due to the high dose intake (600 mg per day) (Nagata et al. 1985). Another study indicated that a patient who consumed 76 g of elemental Ge for 6 months developed renal failure (Lück et al. 1999). Bian et al. (2017) published a study on MgGe alloys, in which the potential cytotoxic effects of Ge on the human body were explored (Ge concentrations below 3wt percent). Their study demonstrated that MgGe alloys own excellent cytocompatibility, histocompatibility, good mechanical features, and corrosion resistance. The combination of such properties makes Ge metal and its alloys excellent potential candidates for implant materials. Moreover, the superior mechanical and physical qualities of W, such as its high melting point, wear resistance, and hardness, make it a desirable metal for use in a variety of applications.

In this study, we aim to obtain a composite of these two metals to enhance their superior properties against bacteria. For this purpose, W-Ge nanocomposite films as a function of Ge concentrations were deposited on AZ61Mg by magnetron sputtering approach to investigate their antibacterial efficiency in biological applications. Subsequently, the phase structure, surface morphology and wettability of the samples were examined. The antibacterial efficiency of W-Ge nanocomposite thin films as a function of Ge concentrations against gram-negative (*Salmonella typhimurium* NRRLE 4413, *Escherichia coli* ATCC 25922) and gram-positive (*Staphylococcus aureus* 6538 P., *Bacillus subtilis* IM 622) bacteria has been investigated.

## 2. EXPERIMENTAL DETAILS

### 2.1. Sample Preparation

Initially, AZ61 Mg substrates with dimensions of 10×20×2 mm were polished with 800–2000 mesh Silicon Carbide (SiC) abrasive papers, and 5 μm aluminium oxide (Al<sub>2</sub>O<sub>3</sub>) powder. Afterwards, then the surfaces of the Mg substrates were cleaned using an RCA type wet-cleaning procedure using acetone, methanol, and distilled water, respectively, in an ultrasonic cleaner for 3 minutes for each Mg substrate. The cleaning procedure was completed by blow-drying with nitrogen gas.

### 2.2. Thin Film Deposition

Tungsten (W) and Germanium (Ge) solid targets with a purity of 99.99% were used to coat Mg substrates. Plasma cleaning was applied to each target for 10 minutes prior to the coating process to remove contamination and achieve a more efficient

surface activity. All Mg substrates were coated using a Nanovak magnetron sputter system (Model: NVTS-400). The base pressure of the system was approximately  $4 \times 10^{-6}$  mTorr and the working pressure during the deposition process of all samples was approximately  $3 \times 10^{-3}$  mTorr. The co-deposition technique was used to deposit W-Ge nanocomposite coatings on the Mg substrates through the alteration of Ge concentration (5%, 10%, 20%, 40%, and 60%). A quartz thickness monitor was used to determine the deposition rates of the alloy samples. Ge concentrations of W-Ge nanocomposite coatings were controlled by adjusting the deposition rates of W and Ge based on the published work by Kurt et al. (2021). The distance between the substrate and the targets was approximately 15 cm, and the deposition was performed at room temperature. The thickness of the films was measured as  $1 \pm 0.9$  μm using an optical profilometer.

### 2.3. Sample Characterisation

The phase composition of the W-Ge nanocomposite coatings was analysed using the X-ray diffraction (XRD) technique with a Rigaku SmartLab diffractometer and a Cu Kα (1.5406 Å) radiation source. The morphology of the films at different Ge concentrations was evaluated using scanning electron microscopy (SEM) with an FEI Versa 3D Dual Beam. The surface roughness of the films was determined by atomic force microscopy (AFM – Park System XE-100E). The thickness of the films for each deposition condition was measured using a Bruker-Contour GT 3D Optical profilometer. The wettability and contact angle values of the coatings were analysed using the sessile drop technique with a contact angle goniometer (CAG) (Dataphysics OCA 15EC) at room temperature. The contact angle values were measured 60 seconds after pure water was dropped onto the surfaces.

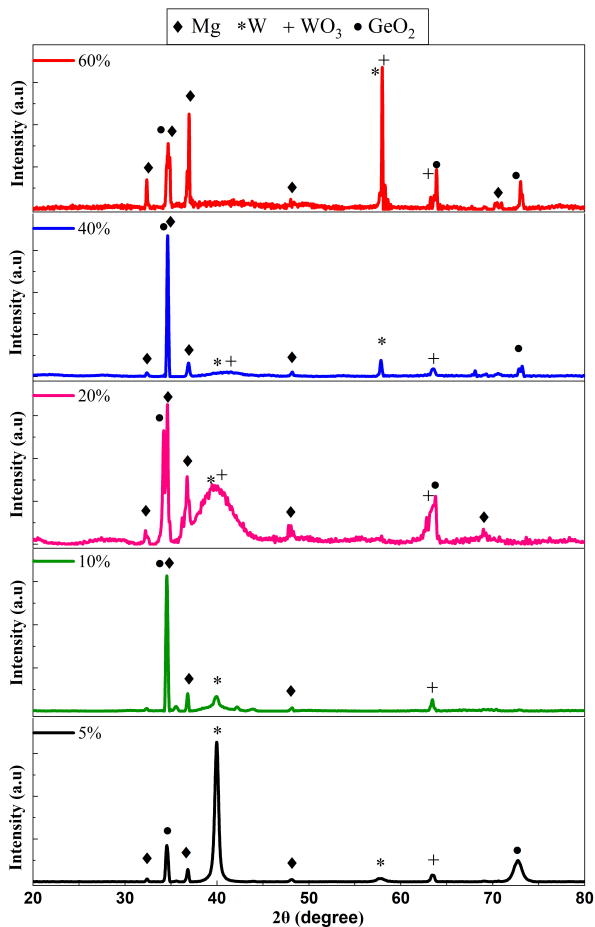
### 2.4. In-vitro Bacterial Test

The antimicrobial activity of W-Ge nanocomposite coatings against gram negative (*Salmonella typhimurium* NRRLE 4413, *Escherichia coli* ATCC 25922) and gram-positive bacteria (*Staphylococcus aureus* 6538 P., *Bacillus subtilis* IM 622) was investigated via disc diffusion antibiotic sensitivity assay in which 6 mm of diameters discs were placed on the plates. The antibiotic discs and the Mg substrates which were coated with approximately 1 μm of W-Ge nanocomposite films at different concentration of Ge (5-60%) were placed on Muller-Hinton agar (MHA) plates inoculated with 100 μl of  $1 \times 10^6$  bacterial suspensions. Plates were then incubated at 37 °C overnight, followed by measurement of the diameters of inhibition zones. During the tests, an antibiotic mixture (penicillin-streptomycin) was used as a positive control.

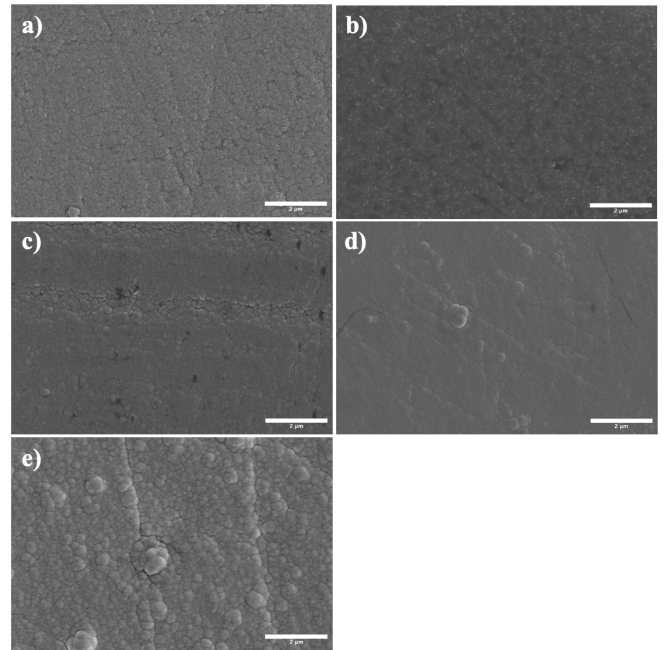
### 3. RESULT AND DISCUSSION

Figure 1 displays the crystallographic properties of W-Ge nanocomposite films deposited on AZ61Mg by magnetron sputtering.  $2\theta$  Mg peak values of  $32^\circ.33$ ,  $34^\circ.66$ ,  $36^\circ.82$ , and  $48^\circ.13$  matched with the entry number of 96-151-2519, are observed due to the Mg substrate for all Ge concentrations. Crystal structure of  $\text{GeO}_2$  are observed at  $34^\circ.22$  with (111) plane from all coatings and at  $62^\circ.63$  with (221) planes from 20% and 60% Ge concentration. Additional  $2\theta$   $\text{GeO}_2$  peak is detected at  $72^\circ.73$  with (112) orientation from 5%, 40% and 60% coatings (entry no: 96-152-5833).  $2\theta$  peak values  $39^\circ.90$ , and  $57^\circ.70$  indicate the metallic W with the (101), (200) planes, respectively (entry no: 96-151-2550). Besides,  $\text{WO}_3$  crystal structure is obtained from all coatings at  $63^\circ.44$ , indicating the (400) plane. Whilst,  $2\theta$   $\text{WO}_3$  peak value of  $40^\circ.38$  with (201) plane is observed for 20% and 40% Ge concentrations, this is obtained at  $57^\circ.98$  with (202) plane for 60% Ge concentration (entry no: 96-100-4057). It can be concluded that the film coatings were formed as a composite crystal structure.

Figure 2 displays the morphology of the W-Ge nanocomposite thin films as a function of Ge concentrations. SEM images reveal two types of morphology, including goosefoot-type and



**Figure 1.** XRD spectrum of W-Ge thin film deposited on AZ61 Mg.



**Figure 2.** SEM images of the W-Ge nanocomposites coatings for a) 5% b) 10% c) 20% d) 40% e) 60% Ge concentrations.

cauliflower-type, for low (5%, 10%, 20%) and high Ge (40% and 60%) concentrations, respectively. In light of these morphological differences in the SEM images, it can be considered that there are two types of mechanisms in film formation. The increase of the Ge concentration for low Ge films led to a reduction in the goosefoot structure as shown in Figure 2a-c, which result in a reduction in the number of grains. However, the film with a 20% Ge concentration has a combined morphological structure of a goosefoot and a cauliflower-type. Conversely, coatings with high concentrations of Ge exhibit a contrasting effect, resulting in a cauliflower-like surface morphology in Ge-rich films. Specifically, the coating with a Ge concentration of 60% demonstrates a notable abundance of grains, as displayed in Figure 2e. The surface roughness of W-Ge nanocomposite coatings was evaluated using by AFM as a function of Ge concentration. It is found that the roughness varies between 35 to 90 nm, as illustrated in Figure 3a.

The surface roughness of W-Ge nanocomposite films at low Ge concentrations (5%, 10% and 20%) increase as a function of Ge concentration. This result is in a good agreement with SEM analyses since the surface morphology of thin film is less smooth and has some pores at 20% Ge concentration. Besides, surface roughness of 40% Ge concentration of W-Ge nanocomposite film decreases the level of lowest Ge concentration. The SEM image of W-Ge nanocomposite films at 40% Ge concentration shows a smoother surface profile (Figure 2d). As expected from the SEM image given in Figure 2e, the 60% Ge concentration leads to the highest surface roughness due to high number of grains and pores.

The effect of the variation of Ge concentration on surface

wetting characteristic was determined by measuring contact angle values 60 s after dropping  $1\mu\text{l}$  distilled water on thin film surface and the results are illustrated in Figure 3b. The wetting property of a surface is defined as hydrophobic if the contact angle is greater than  $90^\circ$  and hydrophilic if it is less than  $90^\circ$  (Law 2014; Kuruoğlu 2022). The contact angle values of W-Ge nanocomposite coatings with 5%, 10%, 20%, 40% and 60% Ge concentration are  $68^\circ.6$ ,  $55^\circ.8$ ,  $27^\circ.4$ ,  $85^\circ.6$  and  $62^\circ.7$ , respectively. Hence, as shown in Figure 3b, the W-Ge nanocomposite coatings altered with Ge concentration have hydrophilic surfaces and the highest and the lowest contact angle values are obtained at 40% and 20% Ge concentrations, respectively. Additionally, the contact angle values of the remaining Ge concentrations are apparently similar. It is well known that surface chemistry and surface morphology determine the wetting characteristic of surface. The effect of surface morphology (smooth or rough surface) on the wettability of surface were modelled by Young (1805) and Cassie & Baxter (1944) or Wenzel (1936). According to the Wenzel model, an increase in roughness leads to a hydrophilic surface to be more hydrophilic, and a hydrophobic surface to be more hydrophobic. The results of surface roughness measurements and wettability tests of W-Ge nanocomposite films reveal that, in general, with the increase of surface roughness, the wettability of the surfaces decreases (see Figure 3a-b). It can be concluded that W-Ge nanocomposite films have hydrophilic surface properties and their hydrophilicity increases with increasing surface roughness, which obeying Wenzel model (Wenzel 1936). While, W-Ge nanocomposite films with 60% Ge concentration possess the highest rms surface roughness value of 93.3 nm, its contact angle ( $62^\circ.7$ ) is approximately the same values of W-Ge nanocomposite coatings with 5% Ge concentration. This behaviour can be explained with Cassie-Baxter model where droplet cannot penetrate the surface cavities, regardless to the nature of surface, owing to the air pockets under the droplet (Foadi et al. 2019b,a).

Gram-positive (*Staphylococcus aureus* 6538 P., *Bacillus subtilis* IM 622) and gram-negative (*Salmonella typhimurium* NR-RLE 4413, *Escherichia coli* ATCC 25922) were used as model bacteria to reveal antibacterial activities of the W-Ge based nanocomposite coatings as a function of Ge concentration. The formation of inhibition zones confirms the presence of antibacterial activity in all W-Ge nanocomposite coatings. The antibacterial effects of the coatings on gram-positive and gram-negative bacteria follow different patterns and it is observed that it is more effective against to gram-positive bacteria as presented in Figure 4a-b. These differences can be attributed to the differences in cell wall of bacteria. Gram-positive bacteria has a thick peptidoglycan layer and no outer lipid membrane whilst gram-negative bacteria has a thin peptidoglycan layer and has an outer lipid membrane. In fact, a gram-positive bacterium (i.e. *S. aureus*) is made up of an outer membraneless peptidoglycan layer with a thickness ranging from 20 to 80

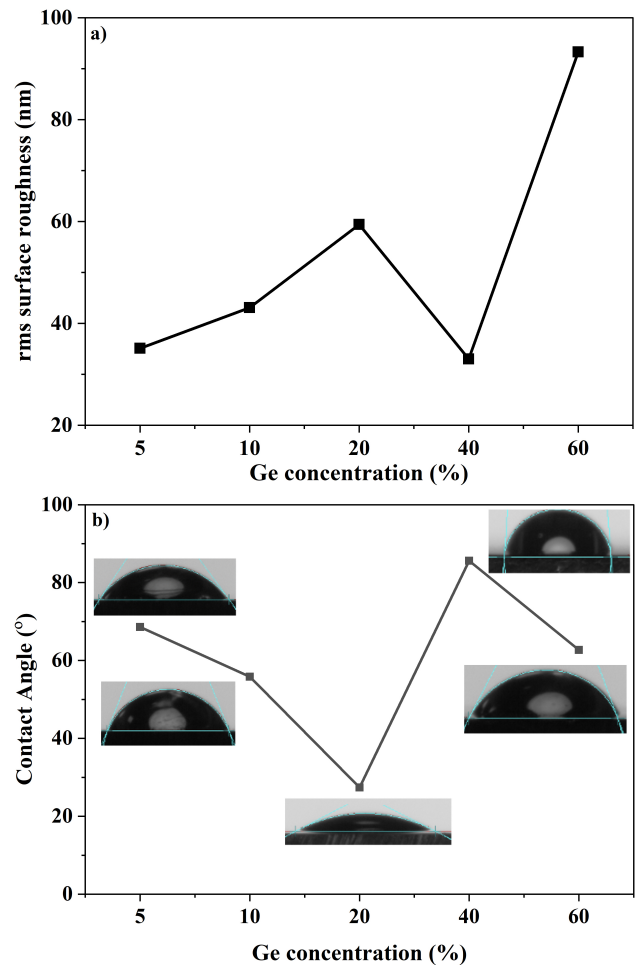


**Figure 3.** a) Surface roughness and b) contact angle values of W-Ge nanocomposite coatings thin film surfaces as a function of Ge concentration.

nm. The outer membrane is an extra layer that *E. coli* has, despite being a gram-negative bacteria with a considerably thinner layer of peptidoglycan (thickness of 78 nm). Additionally, it has been previously noted that the outer membrane of the gram-negative *E. coli* bacterium made *E. coli* more resistant to an AFM tip-induced direct contact interaction than *S. aureus* (Akhavan & Ghaderi 2010; Eaton et al. 2008). Antibacterial efficiencies of W-Ge nanocomposite coatings against to *E. coli* and *S. typhimurium* as a function of Ge concentration show similar behaviour with increasing up to 20% Ge concentration and small amount decrease at 40% Ge. The surface roughness of the coatings is found to play a critical role in their antibacterial efficacy against *S. typhimurium*, and increasing surface roughness led to oxidation of the coatings, resulting in more intense  $\text{GeO}_2$  and  $\text{WO}_3$  peaks rather than metallic W (as shown in Figure 1). These findings are supported by the literature that has revealed the influence of surface roughness and  $\text{WO}_3$  of antibacterial efficiency of the coatings (Wu et al. 2018b,a; Tan et al. 2021). Additionally, while W-Ge nanocomposite coating with 60% Ge concentration exhibits the highest antibacterial effects against *S. typhimurium*, with a high number of grains

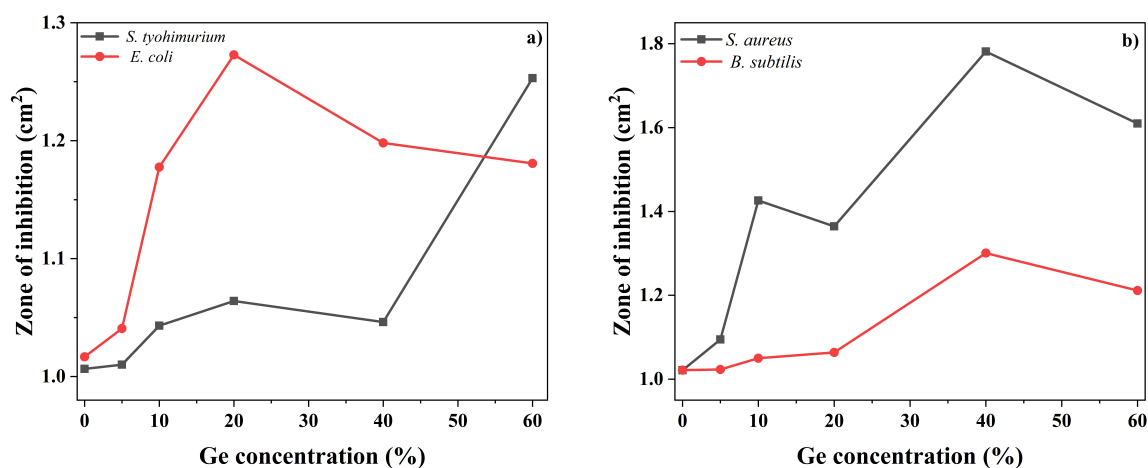


**Figure 4.** Antibacterial activity of W-Ge nanocomposite coatings as function of Ge concentration on a) gram-negative bacteria and b) gram-positive bacteria.

and the most intense WO<sub>3</sub> peaks, a similar effect is observed at 20% Ge concentration against *E. coli* (as shown in Figure 4a). As demonstrated in Figure 4b, the antibacterial efficiency of W-Ge nanocomposite coatings against *S. aureus* and *B. subtilis* is reasonably higher than against the gram-negative bacteria and exhibits the same tendency as a function of Ge concentration, with maximum efficiency being reached at 40% Ge concentration against *S. aureus*.

#### 4. CONCLUSION

In this study, findings on the selective antibacterial properties of W-Ge nanocomposite films based on varying Ge concentrations were presented. With increasing Ge concentration, two types of surface mechanisms (goosefoot and cauliflower-type) were observed, resulting to changes in surface roughness. The study also found that increased surface roughness led to higher oxidation of the coatings due to a higher number of grains. The coatings were found to have hydrophilic surfaces with an opposite trend with surface roughness. Results from antimicrobial activity measurements showed that the coatings had antibacterial activity against both gram-negative and gram-positive bacteria, with higher efficacy against gram-positive bacteria. It could be concluded that increased surface roughness led to higher numbers of grain boundaries, intensifying the metals' oxide phases and improving their antibacterial activity.

**Peer Review:** Externally peer-reviewed.

**Author Contribution:** Conception / Design of study - S.Atasoy, S.Aktas; Data Acquisition - S.Atasoy, Y.K., S.Aktas, F.S., M.S.K., A.A., E.D.; Data Analysis / Interpretation - S.Atasoy, S.Aktas, F.S., A.A.; Drafting Manuscript - S.Atasoy, S.Aktas, F.S., A.A., M.S.K.; Critical Revision of Manuscript - S.Atasoy, S.Aktas, F.S., A.A., A.E.; Final Approval and Accountability - S.Atasoy, S.Aktas, F.S.; Technical or Material Support - F.S., M.S.K.; Supervision - A.E.

**Conflict of Interest:** Authors declared no conflict of interest.

**Financial Disclosure:** Authors declared no financial support.

#### LIST OF AUTHOR ORCIDS

S. Atasoy	<a href="https://orcid.org/0000-0003-0712-7904">https://orcid.org/0000-0003-0712-7904</a>
Y. Kurul	<a href="https://orcid.org/0000-0002-8708-6753">https://orcid.org/0000-0002-8708-6753</a>
S. Aktas	<a href="https://orcid.org/0000-0002-9143-6752">https://orcid.org/0000-0002-9143-6752</a>
F. Sarcan	<a href="https://orcid.org/0000-0002-8860-4321">https://orcid.org/0000-0002-8860-4321</a>
M. S. Kurt	<a href="https://orcid.org/0000-0002-2639-1850">https://orcid.org/0000-0002-2639-1850</a>
A. Ayna	<a href="https://orcid.org/0000-0001-6801-6242">https://orcid.org/0000-0001-6801-6242</a>
E. Darendelioğlu	<a href="https://orcid.org/0000-0002-0630-4086">https://orcid.org/0000-0002-0630-4086</a>
A. Erol	<a href="https://orcid.org/0000-0003-4196-1791">https://orcid.org/0000-0003-4196-1791</a>

#### REFERENCES

- Akhavan O., Ghaderi E., 2010, *ACS Nano*, 4, 5731
- Arslan M. E., Kurt M. Ş., Aslan N., Kadi A., Öner S., Çobanoğlu Ş., Yazici A., 2022, *Journal of Biomedical Materials Research Part B: Applied Biomaterials*, 110, 1667
- Bian D., et al., 2017, *Acta Biomaterialia*, 64, 421
- Cassie A. B. D., Baxter S., 1944, *Trans. Faraday Soc.*, 40, 546
- Chuang K.-T., Abdullah H., Leu S.-J., Cheng K.-B., Kuo D.-H., Chen H.-C., Chien J.-H., Hu W.-T., 2017, *Journal of Photochemistry and Photobiology A: Chemistry*, 337, 151
- Eaton P., Fernandes J. C., Pereira E., Pintado M. E., Xavier Malcata F., 2008, *Ultramicroscopy*, 108, 1128
- Foadi F., Vaez Allaei S. M., Palasantzas G., Mohammadzadeh M. R., 2019a, *Phys. Rev. E*, 100, 022804
- Foadi F., ten Brink G. H., Mohammadzadeh M. R., Palasantzas G., 2019b, *Journal of Applied Physics*, 125
- Helmerson U., Lattemann M., Bohlmark J., Ehiasarian A. P., Gudmundsson J. T., 2006, *Thin Solid Films*, 513, 1
- Jena G., Anandkumar B., Vanithakumari S., George R., Philip J., Amarendra G., 2020, *Progress in Organic Coatings*, 139, 105444

- Kaplan B. J., Parish W. W., Andrus G. M., Simpson J. S. A., Field C. J., 2004, *The Journal of Alternative and Complementary Medicine*, 10, 337
- Khalid A. Q., AlJohny B. O., Wainwright M., 2014, *African Journal of Microbiology Research*, 8, 1080
- Kurt M. Ş., Arslan M. E., Yazici A., Mudu İ., Arslan E., 2021, *Journal of Materials Science: Materials in Medicine*, 32, 6
- Kuruoğlu F., 2022, *Microfluidics and Nanofluidics*, 26, 72
- Law K.-Y., 2014, *The Journal of Physical Chemistry Letters*, 5, 686
- Lück B. E., Mann H., Melzer H., Dunemann L., Begerow J., 1999, *Nephrology Dialysis Transplantation*, 14, 2464
- Martin P. M., 2009, *Handbook of Deposition Technologies for Films and Coatings: Science, Applications and Technology*. William Andrew
- Menazea A., Awwad N. S., 2020, *Journal of Materials Research and Technology*, 9, 9434
- Nagata N., Yoneyama T., Yanagida K., Ushio K., Yanagihara S., Matsubara O., Eishi Y., 1985, *The Journal of Toxicological Sciences*, 10, 333
- Okada K., Okagawa K., Kawakami K., et al. 1989, *Clinical Nephrology*, 31, 219
- Park S.-M., Ikegami T., Ebihara K., Shin P.-K., 2006, *Applied Surface Science*, 253, 1522
- Roy D., Halder N., Chowdhury T., Chattaraj A., Roy P., 2015, *IOSR J VLSI Signal Process*, 5, 69
- Sarcan F., 2020, *Nanotechnology*, 31, 435502
- Sellappa S., Jeyaraman V., 2011, *International Journal of Pharma and Bio Sciences*, 2, 854
- Somogyvári Z., Langer G., Erdélyi G., Balázs L., 2012, *Vacuum*, 86, 1979
- Tan G.-L., Tang D., Dastan D., Jafari A., Shi Z., Chu Q.-Q., Silva J. P., Yin X.-T., 2021, *Ceramics International*, 47, 17153
- Voevodin A. A., O'Neill J. P., Prasad S. V., Zabinski J. S., 1999, *Journal of Vacuum Science & Technology A*, 17, 986
- Wenzel R. N., 1936, *Industrial & Engineering Chemistry*, 28, 988
- Wu S., Altenried S., Zogg A., Zuber F., Maniura-Weber K., Ren Q., 2018a, *ACS Omega*, 3, 6456
- Wu S., Zuber F., Maniura-Weber K., Brugger J., Ren Q., 2018b, *Journal of Nanobiotechnology*, 16, 20
- Young T., 1805, *Philosophical Transactions of the Royal Society of London*, 95, 65
- Zboun M., Arisan V., Topcuoglu N., Kuruoglu F., Sener L. T., Sarcan F., 2020, *Surfaces and Interfaces*, 21, 100703

### AIMS AND SCOPE

Physics and Astronomy Reports aims to contribute to the scientific knowledge in all areas of physics and astronomy. It is an open-access, peer-reviewed and international journal published semiannually in June and December.

The journal is devoted to publish original research and review articles written in English. Original and high quality research articles, review articles (by invitation only), and high-quality conference proceedings (in special issues by the approval of the editorial board) are welcome. The journal targets international and national communities.

Processing and publication are free of charge with the journal. There is no article processing charges or submission fees for any submitted or accepted articles.

### POLICIES

#### Publication Policy

The journal is committed to upholding the highest standards of publication ethics and pays regard to Principles of Transparency and Best Practice in Scholarly Publishing published by the [Committee on Publication Ethics \(COPE\)](#), the [Directory of Open Access Journals \(DOAJ\)](#), the [Open Access Scholarly Publishers Association \(OASPA\)](#), and the [World Association of Medical Editors \(WAME\)](#) on <https://publicationethics.org/resources/guidelines-new/principles-transparency-and-best-practice-scholarly-publishing>

The subjects covered in the manuscripts submitted to the journal for publication must be in accordance with the aim and scope of the journal. Only those manuscripts approved by every individual author and that were not published before or sent to another journal, are accepted for evaluation.

Changing the name of an author (omission, addition or order) in papers submitted to the Journal requires written permission from all the declared authors.

Plagiarism, duplication, fraudulent authorship/denied authorship, research/data fabrication, salami slicing/salami publication, breaching copyrights, and prevailing conflicts of interest are unethical behaviors. All manuscripts that are not in accordance with accepted ethical standards will be removed from publication. This also includes any possible malpractice discovered after publication.

#### Plagiarism:

Submitted manuscripts that pass the preliminary control are scanned for plagiarism using iThenticate software. If plagiarism/self-plagiarism is found, the authors will be

informed of it. Editors may resubmit the manuscript for a similarity check at any peer-review or production stage if required. High similarity scores may lead to rejection of the manuscript before and even after acceptance. Depending on the type of article and the percentage of the similarity score taken from each article, the overall similarity score is generally expected to be less than 15 or 20%.

#### Double Blind Peer-Review:

After the plagiarism check, the eligible ones are evaluated by the editors-in-chief for their originality, methodology, importance of the subject covered and compliance with the journal scope. The editor provides a fair double-blind peer review of the submitted articles and hands over the papers matching the formal rules to at least two national/international referees for evaluation and gives green light for publication upon modification by the authors in accordance with the referees' claims.

#### Open Access Statement

The journal is open access and all content is freely available without charge to the user or his/her institution. Except for commercial purposes, users are allowed to read, download, copy, print, search, or link to the full text of the articles in this journal without asking prior permission from the publisher or author. This is in accordance with the [BOAI](#) definition of open access.

The open access articles in the journal are licensed under the terms of the Creative Commons Attribution-NonCommercial 4.0 International ([CC BY-NC 4.0](#)) license.

#### Article Processing Charge

All expenses of the journal are covered by Istanbul University. The processing and publication are free of charge. There are no article processing charges or submission fees for any submitted or accepted articles.

#### Copyright Notice

Authors publishing with the journal retain the copyright to their work licensed under the Creative Commons Attribution-NonCommercial 4.0 International license (<https://creativecommons.org/licenses/by-nc/4.0/>) and grant the Publisher non-exclusive commercial right to publish the work. CC BY-NC 4.0 license permits unrestricted, non-commercial use, distribution, and reproduction in any medium, provided the original work is properly cited.



### Correction, Retraction, Expression of Concern

The editor should consider publishing corrections if minor errors that do not affect the results, interpretations and conclusions of the published paper are detected. The editor should consider retraction if major errors and/or misconduct invalidate results and conclusions are detected.

The editors should consider issuing an expression of concern if there is evidence of research or publication misconduct by the authors; there is evidence that the findings are not reliable and institutions of the authors do not investigate the case or the possible investigation seems to be unfair or nonconclusive.

The [COPE](#) and [ICJME](#) guidelines are considered for correction, retractions or expression of concern.

### Archiving Policy

To guarantee that all papers published in the journal are maintained and permanently accessible, articles are stored in Dergipark, which serves as a national archival website and simultaneously permits LOCKSS to collect, preserve, and serve content.

Additionally, the authors are encouraged to self-archive the final PDF version of their articles in open electronic archives, which conform to the standards of the Open Archives Initiative ([https:// www.openarchives.org/](https://www.openarchives.org/) ). Authors should provide a link from the deposited version to the URL of IUPress journal website.

## ETHICS

### PUBLICATION ETHICS AND PUBLICATION MALPRACTICE STATEMENT

Physics and Astronomy Reports is committed to upholding the highest standards of publication ethics and pays regard to Principles of Transparency and Best Practice in Scholarly Publishing published by the [Committee on Publication Ethics \(COPE\)](#), the [Directory of Open Access Journals \(DOAJ\)](#), the [Open Access Scholarly Publishers Association \(OASPA\)](#), and the [World Association of Medical Editors \(WAME\)](#) on <https://publicationethics.org/resources/guidelines-new/principles-transparency-and-best-practice-scholarly-publishing>

All submissions must be original, unpublished (including full text in conference proceedings), and not under the review of any other publication. The authors must ensure that the submitted work is original in nature. They must certify that the manuscript has not already been published or submitted elsewhere, in any language. Applicable copy-

right laws and conventions must be followed. Copyright materials (e.g., tables, figures or extensive quotations) must be reproduced only with appropriate permission and acknowledgement. Any work or words by other authors, contributors, or sources must be appropriately credited and referenced.

Each manuscript is reviewed by at least two referees using a double-blind peer review process. Plagiarism, duplication, fraudulent authorship/ denied authorship, research/data fabrication, salami slicing/salami publication, breaching of copyrights, and prevailing conflicts of interest are unethical behaviors. All manuscripts that are not in accordance with accepted ethical standards will be removed from publication. This also includes any possible malpractice discovered after publication.

### Research Ethics

Physics and Astronomy Reports adheres to the highest standards in research ethics and follows the principles of international research ethics as defined below. The authors are responsible for the compliance of the manuscripts with ethical rules.

- Principles of integrity, quality and transparency should be sustained in designing the research, reviewing the design and conducting the research.
- The research team and participants should be fully informed about the aims, methods, possible uses, requirements of the research, and risks of participation in research.
- The confidentiality of the information provided by the research participants and the confidentiality of the respondents should be ensured. The research should be designed to protect the autonomy and dignity of the participants.
- Research participants should voluntarily participate in the research, not under any coercion.
- Any possible harm to the participants must be avoided. Research should be planned in such a way that the participants are not at risk.
- The independence of research must be clear, and any conflicts of interest must be disclosed.
- In experimental studies with human subjects, written informed consent from the participants who decided to participate in the research must be obtained. In the case of children and those under wardship or with confirmed insanity, legal custodian assent must be obtained.

- If the study is to be carried out in any institution or organization, approval must be obtained from that institution or organization.
- In studies with human subjects, it must be noted in the method section of the manuscript that the informed consent of the participants and ethics committee approval from the institution where the study was conducted have been obtained.

### Author's Responsibilities

The authors are responsible for ensuring that the article is in accordance with scientific and ethical standards and rules. The authors must ensure that the submitted work is original in nature. They must certify that the manuscript has not already been published or submitted elsewhere, in any language. Applicable copyright laws and conventions must be followed. Copyright materials (e.g., tables, figures or extensive quotations) must be reproduced only with appropriate permission and acknowledgement. Any work or words by other authors, contributors, or sources must be appropriately credited and referenced.

All the authors of the submitted manuscript must have direct scientific and academic contributions to the manuscript. The author(s) of the original research articles is defined as a person who is significantly involved in “conceptualization and design of the study”, “collecting the data”, “analyzing the data”, “writing the manuscript”, “reviewing the manuscript with a critical perspective” and “planning/conducting the study of the manuscript and/or revising it”. Fund raising, data collection and supervision of the research group are not sufficient roles to be accepted as authors. The author(s) must meet all these criteria described above. The order of names in the author list of an article must be a co-decision and must be indicated in the [Copyright Agreement Form](#).

Individuals who do not meet the authorship criteria but have contributed to the study must take place in the acknowledgement section. Individuals providing technical support, general support, material, financial support and assisting in writing are examples to be indicated in the acknowledgement section.

All authors must disclose any issues concerning financial relationships, conflicts of interest, and competing interests that may potentially influence the results of the research or scientific judgment. When an author discovers a significant error or inaccuracy in his/her own published paper, it is the author's obligation to promptly cooperate with the editor-in-chief to provide retractions or corrections of mistakes.

### Responsibility for the Editor and Reviewers

The editor-in-chief evaluates manuscripts for their scientific content without regard to ethnic origin, gender, sexual orientation, citizenship, religious beliefs or the authors' political philosophy. He/She provides a fair double-blind peer review of the submitted articles for publication and ensures that all the information related to submitted manuscripts is kept as confidential before publishing.

The editor-in-chief is responsible for the content and overall quality of publications. He/She must publish errata pages or make corrections when needed.

The editor-in-chief does not allow any conflicts of interest between the authors, editors and reviewers. Only he has the full authority to assign a reviewer and is responsible for the final decision to publish the manuscripts in the journal.

The reviewers must have no conflict of interest with respect to the research, authors and/or research funders. Their judgment must be objective.

Reviewers must ensure that all information related to submitted manuscripts is kept confidential and must report to the editor if they are aware of copyright infringement and plagiarism on the author's side.

A reviewer who feels unqualified to review the topic of a manuscript or knows that its prompt review will be impossible should notify the editor and excuse him/herself from the review process.

The editor informs the reviewers that the manuscripts are confidential information and that this is a privileged interaction. The reviewers and editorial board cannot discuss the manuscripts with other people. The anonymity of referees must be ensured. In particular situations, the editor may share a review by one reviewer with other reviewers to clarify a particular point.

### PEER REVIEW

#### Peer Review Policies

Only those manuscripts approved by every individual author and that were not published before or submitted to another journal, are accepted for evaluation.

Submitted manuscripts that pass the preliminary control are scanned for plagiarism using iThenticate software. After the plagiarism check, the eligible ones are evaluated by the editor-in-chief for their originality, methodology, importance of the subject covered, and compliance with the journal scope.

The editor hands over the papers matching the formal rules to at least two national/international referees

for double-blind peer review evaluation and gives green light for publication upon modification by the authors in accordance with the referees' claims.

### Responsibility for the Editor and Reviewers

The editor-in-chief evaluates manuscripts for their scientific content without regard to ethnic origin, gender, sexual orientation, citizenship, religious beliefs or the authors' political philosophy. He/She provides a fair double-blind peer review of the submitted articles for publication and ensures that all the information related to submitted manuscripts is kept as confidential before publishing.

The editor-in-chief is responsible for the content and overall quality of publications. He/She must publish errata pages or make corrections when needed. The editor-in-chief does not allow any conflicts of interest between the authors, editors and reviewers. Only he has the full authority to assign a reviewer and is responsible for the final decision to publish the manuscripts in the journal.

The reviewers must have no conflict of interest with respect to the research, authors and/or research funders. Their judgment must be objective.

Reviewers must ensure that all information related to submitted manuscripts is kept confidential and must report to the editor if they are aware of copyright infringement and plagiarism on the author's side.

A reviewer who feels unqualified to review the topic of a manuscript or knows that its prompt review will be impossible should notify the editor and excuse him/herself from the review process.

The editor informs the reviewers that the manuscripts are confidential information and that this is a privileged interaction. The reviewers and editorial board cannot discuss the manuscripts with other people. The anonymity of referees must be ensured. In particular situations, the editor may share a review by one reviewer with other reviewers to clarify a particular point.

### Peer Review Process

Only those manuscripts approved by every individual author and that were not published before or submitted to another journal, are accepted for evaluation.

Submitted manuscripts that pass the preliminary control are scanned for plagiarism using iThenticate software. After the plagiarism check, the eligible ones are evaluated by the editor-in-chief for their originality, methodology, importance of the subject covered and compliance with the journal scope. Editor-in-chief evaluates manuscripts for their scientific content without regard to ethnic origin,

gender, sexual orientation, citizenship, religious belief or political philosophy of the authors and ensures a fair double-blind peer review of the selected manuscripts.

The selected manuscripts are sent to at least two national/international referees for evaluation, and publication decision is made by the editor-in-chief upon modification by the authors in accordance with the referees' claims.

Editor-in-chief does not allow any conflicts of interest between the authors, editors, and reviewers and is responsible for the final decision for publication of the manuscript in the journal.

The reviewers' judgments must be objective. Reviewers' comments on the following aspects are expected during the review.

- Does the manuscript contain new and significant information?
- Does the abstract clearly and accurately describe the content of the manuscript?
- Is this problem significant and concisely stated?
- Are the methods comprehensively described?
- Are the interpretations and conclusions justified by the results?
- Is adequate reference made to other works in the field?
- Is the language acceptable?

Reviewers must ensure that all information related to submitted manuscripts is kept confidential and must report to the editor if they are aware of copyright infringement and plagiarism on the author's side.

A reviewer who feels unqualified to review the topic of a manuscript or knows that its prompt review will be impossible should notify the editor and excuse him/herself from the review process.

The editor informs the reviewers that the manuscripts are confidential information, and that this is a privileged interaction. The reviewers and editorial board cannot discuss the manuscripts with other people. The anonymity of the referees is important.

## AUTHOR GUIDELINES

### Manuscript Organization and Submission

1. The publication language of the journal is English
2. Authors are required to submit Copyright Agreement Form, Author Form and Title Page together with the main manuscript document

3. Manuscripts should be prepared using the article template in Latex format
4. Due to double-blind peer review, the main manuscript document must not include any author information.
5. Title page should be submitted together with the main manuscript document and should include the information below:
  - Category of the manuscript
  - The title of the manuscript.
  - All authors' names and affiliations (institution, faculty/department, city, country), e-mail addresses, and ORCIDs.
  - Information of the corresponding author (in addition to the author's information e-mail address, open correspondence address, and mobile phone number).
  - Financial support
  - Conflict of interest.
  - Acknowledgment.
6. Submitted manuscripts should have an abstract of 150-250 words before the introduction, summarizing the scope, the purpose, the results of the study, and the methodology used. Under the abstract, a minimum of 3 and a maximum of 6 keywords that inform the reader about the content of the study should be specified.
7. The manuscripts should contain mainly these components: title, abstract and keywords; sections, references, tables and figures. The main text of research articles should include introduction, methods, results, discussion, conclusion and references subheadings.
8. Tables and figures should be given with a number and a caption. Every Figure or Table should be referred within the text of the article in numerical order with no abbreviations (ie: Table 1, Figure 1)
9. References should be prepared in line with Harvard reference system. For information: <https://www.easybib.com/guides/citation-guides/harvard-referencing/>
10. Authors are responsible for all statements made in their work submitted to the journal for publication.

### References

Physics and Astronomy Reports complies with Harvard system for referencing and in-text citations. For information: <https://www.easybib.com/guides/citation-guides/harvard-referencing/>. Accuracy of citations is the author's responsibility. All references should be cited in the text.

It is strongly recommended that authors use Reference Management Software such as Zotero, Mendeley, etc.

### Submission Checklist

Please ensure the following:

- The title page was prepared according to the journal rules.
- This manuscript has not been submitted to any other journal.
- The manuscript has been checked for English language.
- The manuscript was written in accordance with the full-text writing rules determined by the journal.
- The manuscript has an abstract of 150-250 words and the number of keywords should be 3-6.
- The references are in line with the Harvard reference system.
- The Copyright Agreement Form has been filled in and is ready for submission together with the manuscript.
- The Author Contribution Form has been filled in and is ready for submission together with the manuscript.
- Permission for previously published copyrighted material (text,figure,table) has been obtained if used in the present manuscript.
- The Ethics Committee Report (if necessary) has been obtained and ready for submission together with the manuscript, and the ethics committee report date and number have been given in the manuscript text.
- Review of the journal policies.
- All authors have read and approved the final version of the manuscript.

EK 2-B

 Istanbul University  
 İstanbul Üniversitesi

**Journal name: Physics and Astronomy Reports**  
 Dergi Adı: Physics and Astronomy Reports

**Copyright Agreement Form**  
 Telif Hakkı Anlaşması Formu

<b>Responsible/Corresponding Author</b> <i>Sorumlu Yazar</i>				
<b>Title of Manuscript</b> <i>Makalenin Başlığı</i>				
<b>Acceptance Date</b> <i>Kabul Tarihi</i>				
<b>List of Authors</b> <i>Yazarların Listesi</i>				
<i>Sıra No</i>	<i>Name - Surname Adı-Soyadı</i>	<i>E-mail E-Posta</i>	<i>Signature İmza</i>	<i>Date Tarih</i>
1				
2				
3				
4				
5				

<b>Manuscript Type (Research Article, Review, etc.)</b> <i>Makalenin türü (Araştırma makalesi, Derleme, v.b.)</i>				
<b>Responsible/Corresponding Author:</b> <i>Sorumlu Yazar:</i>				
<b>University/company/institution</b>	<i>Çalıştığı kurum</i>			
<b>Address</b>	<i>Posta adresi</i>			
<b>E-mail</b>	<i>E-posta</i>			
<b>Phone; mobile phone</b>	<i>Telefon no; GSM no</i>			

**The author(s) agrees that:**

The manuscript submitted is his/her/their own original work, and has not been plagiarized from any prior work, all authors participated in the work in a substantive way, and are prepared to take public responsibility for the work, all authors have seen and approved the manuscript as submitted, the manuscript has not been published and is not being submitted or considered for publication elsewhere, the text, illustrations, and any other materials included in the manuscript do not infringe upon any existing copyright or other rights of anyone. İSTANBUL UNIVERSITY will publish the content under Creative Commons Attribution-NonCommercial 4.0 International (CC BY-NC 4.0) license that gives permission to copy and redistribute the material in any medium or format other than commercial purposes as well as remix, transform and build upon the material by providing appropriate credit to the original work. The Contributor(s) or, if applicable the Contributor's Employer, retain(s) all proprietary rights in addition to copyright, patent rights. I/We indemnify İSTANBUL UNIVERSITY and the Editors of the Journals, and hold them harmless from any loss, expense or damage occasioned by a claim or suit by a third party for copyright infringement, or any suit arising out of any breach of the foregoing warranties as a result of publication of my/our article. I/We also warrant that the article contains no libelous or unlawful statements, and does not contain material or instructions that might cause harm or injury. This Copyright Agreement Form must be signed/ratified by all authors. Separate copies of the form (completed in full) may be submitted by authors located at different institutions; however, all signatures must be original and authenticated.

**Yazar(lar) aşağıdaki hususları kabul eder:**

Sunulan makalenin yazar(lar)ın orijinal çalışması olduğunu ve intihal yapmadıklarını, Tüm yazarların bu çalışmaya aslı olarak katılmış olduklarını ve bu çalışma için her türlü sorumluluğu aldıklarını, Tüm yazarların sunulan makalenin son halini gördüklerini ve onayladıklarını, Makalenin başka bir yerde basılmadığını veya basılmak için sunulmadığını, Makalede bulunan metnin, şekillerin ve dokümanların diğer şahıslara ait olan Telif Haklarını ihlal etmediğini kabul ve taahhüt ederler. İSTANBUL ÜNİVERSİTESİ'nin bu fikri eseri, Creative Commons Atıf-GayriTicari 4.0 Uluslararası (CC BY-NC 4.0) lisansı ile yayınlamasına izin verirler. Creative Commons Atıf-GayriTicari 4.0 Uluslararası (CC BY-NC 4.0) lisansı, eserin ticari kullanım dışında her boyut ve formatta paylaşılmasına, kopyalanmasına, çoğaltılmasına ve orijinal esere uygun şekilde atıfta bulunmak kaydıyla yeniden düzenleme, dönüştürme ve eserin üzerine inşa etme dâhil adapte edilmesine izin verir. Yazar(lar)ın veya varsa yazar(lar)ın işverenin telif dâhil patent hakları, fikri mülkiyet hakları saklıdır. Ben/Biz, telif hakkı ihlali nedeniyle üçüncü şahıslarca vuku bulacak hak talebi veya açılacak davalarda İSTANBUL ÜNİVERSİTESİ ve Dergi Editörlerinin hiçbir sorumluluğunun olmadığını, tüm sorumluluğun yazarlara ait olduğunu taahhüt ederim/ederiz. Ayrıca Ben/Biz makalede hiçbir suç unsuru veya kanuna aykırı ifade bulunmadığını, araştırma yapılırken kanuna aykırı herhangi bir malzeme ve yöntem kullanılmadığını taahhüt ederim/ederiz. Bu Telif Hakkı Anlaşması Formu tüm yazarlar tarafından imzalanmalıdır/onaylanmalıdır. Form farklı kurumlarda bulunan yazarlar tarafından ayrı kopyalar halinde doldurularak sunulabilir. Ancak, tüm imzaların orijinal veya kanıtlanabilir şekilde onaylı olması gerekir.

<b>Responsible/Corresponding Author;</b> <i>Sorumlu Yazar;</i>	<b>Signature / İmza</b>	<b>Date / Tarih</b>
		...../...../.....